

ABSTRACT

XU, CHAO. Ultrafast Optical Characterization of Surfaces and Interfaces. (Under the direction of Dr. Kenan Gundogdu).

In my thesis work, I studied a variety of materials using noninvasive optical techniques. These materials are: 1) metallic zirconium (Zr), which is used as nuclear fuel cladding material; 2) bismuth selenide (Bi_2Se_3), a low band gap semiconductor and a layered material that is commonly used in thermoelectric applications and recently shown to exhibit exotic topological insulator behavior; 3) atomically thin transition metal dichalcogenides (TMDCs), which are recently discovered two dimensional semiconductors. The common property of all these systems is that the most important physics or chemistry is taking place at the surface or interface of the material with other materials. For instance, on Zr, naturally, the oxidation forms an interface between Zr and ZrO_2 layers. Under extreme conditions such as experienced in nuclear reactor environment, this formation later on evolves into cracks that leads to failures in a reactor. In Bi_2Se_3 , the topologically important state is at the surface where the bulk terminates and forms a 2D topologically protected electronic state. In TMDC, the whole material itself is a surface and interfacial interactions with the substrate becomes very important to characterize for completely understanding the material properties. Therefore I have developed optical techniques that are specifically sensitive to characterize the variety of physics on surface or interface without using electrical contacts.

First, second harmonic generation (SHG) anisotropy using ultrafast laser, has been applied on studying the bonding between Zr and its oxide film on the top. It was found that the amorphous strain has a big impact on the bonding between Zr and its oxide. With the aid

of ultra-high vacuum (UHV) technique and Auger electron spectroscopy (AES), the oxidation of fresh Zr has been studied. A two-stage process of oxidation on Zr, with the first stage of oxygen adsorption and the second stage of further oxidation slowed down by the already formed oxide, was revealed.

Second, I will show the near surface electric field on Bi_2Se_3 , one promising topological insulator (TI), can be monitored by electric field induced second harmonic (EFISH) generation using ultrafast laser. With controlled doping level and external environment, it was found that three different physical and chemical processes (near surface charge transfer, chemical adsorption and chemical reaction) take place on Bi_2Se_3 in ambient air.

Third, exciton dynamics has been monitored using self-developed transient reflection spectroscopic microscopy (TRSM) on substrate-supported and suspended MoS_2 and WS_2 monolayers, which are in the category of transition metal dichalcogenide (TMDC) materials. It was found that substrate will assist in the non-radiative exciton recombination. On different substrates, exciton dynamics remains the same while the doping level on monolayer from the charge transfer into substrate plays an important role on photo-luminescence. Moreover, exciton-exciton annihilation (EEA) rate can be extracted from the exciton dynamics and it can be mitigated by the presence of substrate.

All my works suggest the significance of ultrafast optical techniques as useful tools on the characterization of surfaces and interfaces, which could give guidance on material optimization and novel device fabrication.

© Copyright 2015 by Chao Xu

All Rights Reserved

Ultrafast Optical Characterization of Surfaces and Interfaces

by
Chao Xu

A dissertation submitted to the Graduate Faculty of
North Carolina State University
in partial fulfillment of the
requirements for the degree of
Doctor of Philosophy

Physics

Raleigh, North Carolina
2015

APPROVED BY:

Kenan Gundogdu
Committee Chair

Daniel Dougherty

David Aspnes

Ki Wook Kim

DEDICATION

To my wife, Wei Liu, for her companion and support all through my PhD study.

To my parents, Hairong Xu and Xingming Sheng, for their support.

BIOGRAPHY

The author, Chao Xu, was born in a small village (Longxi) in China. He had a wonderful childhood with his parents and grandparents' selfless love. He went to a small town (Tianning) for primary school and started to raise his interest in science. After finished his primary school, his parents made a big decision and sent him to a primate junior high school in a small city (Jiashan) to get better education. With his effort, he got enrolled in the best senior high school in the same city. He made a lot of lifetime friends there and his interest in science became mature then. He was admitted into Physics Department in University of Science and Technology of China in a big city (Hefei), majoying in Optics/Physics.

After his graduation in 2010, he came to North Carolina State University pursuing the PhD degree in Physics. Starting from 2011, inspired by the enthusiastic professor, Dr. Kenan Gundogdu, he took the role of research assistant in Gundogdu's group and focused on material characterization using optical methods. At the meantime, in 2014, he got married to Wei Liu, who got her Master degree in Statistics in The Ohio State University in the same year.

Little by little, Chao, traveled across the earth, and got the highest academic degree. Every step, was marked by his family, his advisors, his friends' support and his own effort.

ACKNOWLEDGMENTS

Many people made this thesis possible.

First, I would like to thank my advisor, Dr. Kenan Gundogdu, for his support and guidance in my graduate research. He was the one who made complex physics intuitive. He was the one who worked with me on experiments in the laboratory even through midnight some days. He was the one who made my life in the research group filled with fun. The research experience in Dr. Gundogdu's group will be forever in my memory.

Also, I would like to thank my distinguished committee members, Dr. Daniel Dougherty, Dr. David Aspnes, Dr. Ki Wook Kim, for their guidance and review of this work.

I would like to express my gratitude to my former and current colleagues, Dr. Bilal Gokce, Dr. Cong Mai, Dr. Bhoj Gautum, Andrew Barrette, Robert Younts, Samanvitha Sridhar, Yiling Yu, Yifei Yu, Dr. Somsubhra Maity. It's my pleasure to work with them, and they played an important role in my research.

Special thanks to my friends, Daniel Weston II, Luyang Zhao, Kai Shen, Shupeng Niu, Lin Ning, Cheng Cheng. They made my life more fun.

Finally, I would extend my gratitude to those who helped me but not listed here.

Without those people above, this thesis work can never be possible.

TABLE OF CONTENTS

LIST OF TABLES	ix
LIST OF FIGURES	x
LIST OF ABBREVIATIONS	xviii
Chapter 1 Introduction.....	1
1.1 Background.....	1
1.2 Zirconium (Zr).....	3
1.3 Topological Insulator (TI).....	5
1.4 Transition Metal Dichalcogenide (TMDC) Monolayers.....	9
1.5 Outline.....	13
Chapter 2 Theory of Nonlinear Optics.....	14
2.1 Second Harmonic Generation (SHG).....	14
2.1.1 Brief history of SHG.....	14
2.1.2 SHG on interface.....	15
2.1.3 Microscopic bond model – Anisotropic Bond Model (ABM).....	15
2.1.4 Macroscopic phenomenological model (MPM).....	19
2.1.5 Electric Field Induced Second Harmonic (EFISH) Generation.....	20
2.2 Time Resolved Spectroscopy.....	20
2.2.1 Brief history of Pump-Probe experiment.....	20

2.2.2 Ultrafast Transient Absorption/Reflection (TA/TR) Spectroscopy.....	22
Chapter 3 Experimental Results	25
3.1 Zr.....	25
3.1.1 Overview.....	25
3.1.2 Experimental Methods.....	25
3.1.2.1 In ambient air.....	25
3.1.2.2 In UHV chamber.....	29
3.1.3 Experimental Results	32
3.1.3.1 SHG anisotropy from the interface of Zr/ZrO ₂	32
3.1.3.2 Time dependent AES and SHG results during the oxidation of fresh Zr.....	37
3.1.4 Conclusions.....	46
3.2 Bi ₂ Se ₃	47
3.2.1 Overview.....	47
3.2.2 Experimental Methods.....	48
3.2.3 Ambient Air Cleave.....	49
3.2.4 Cleaves in Controlled Gas Environments.....	53
3.2.5 Discussion.....	56
3.2.5.1 Regime I: Intrinsic charge redistribution.....	57
3.2.5.2 Regime II: Adsorbate Modifications of Electrostatic Fields	59

3.2.5.3 Regime III: Chemical Modification of the Surface	60
3.2.6 Conclusions.....	61
3.3 MoS ₂ and WS ₂ Monolayers.....	62
3.3.1 Overview.....	62
3.3.2 Experimental Methods.....	63
3.3.3 Exciton dynamics on MoS ₂ and WS ₂ monolayers.....	68
3.3.3.1 Suspended versus substrate-supported monolayers.....	68
3.3.3.2 Different substrate-supported monolayers.....	77
3.3.3.3 Exciton-exciton annihilation (EEA) on MoS ₂ and WS ₂ monolayers	80
3.3.4 Conclusions.....	87
Chapter 4 Summary and Future works	88
4.1 Summary.....	88
4.2 Future works	89
4.2.1 Zr.....	89
4.2.2 Bi ₂ Se ₃	89
4.2.3 TMDC monolayers	90
REFERENCES	91
APPENDICES	101
Appendix A Specifications of Laser System	102
Appendix B Focused Laser Beam Size.....	104

Appendix C	Pump Fluence Conversion.....	108
Appendix D	Matlab Code for Anisotropic Bond Model.....	109

LIST OF TABLES

Table 3-1 Fitting parameters for the measured dynamic results on as-grown MoS ₂ and WS ₂ monolayers.	75
Table 3-2 Fitting parameters for the measured dynamics results on different substrate supported MoS ₂ monolayers.	77
Table 3-3 Exciton peak versus Trion peak ratios in PL spectra and DFT simulated substrate-induced dopings.	80
Table 3-4 EEA rates on suspended and substrate-supported MoS ₂ and WS ₂ monolayers.	86

LIST OF FIGURES

Figure 1-1 A lump of graphite, a graphene transistor and a tape dispenser. Donated to the Nobel Museum in Stockholm by Andre Geim and Konstantin Novoselov in 2010.....	2
Figure 1-2 Nuclear fuel cladded by Zr alloys.	3
Figure 1-3 One analogy of topological surface states between trivial TI and nontrivial TI.	5
Figure 1-4 (a) Structure of crystalline Bi_2Se_3 . (b) The electronic structure of Bi_2Se_3 as measured by ARPES, showing the signatures of the exotic metallic surface states in TI. ^{12,13,20} (c) Brillouin zone for Bi_2Se_3 with space group $R3m$. ¹⁹	7
Figure 1-5 (A) Different carrier type regions. (B) Evolution of Fermi level by photon-assisted surface doping by oxygen.	8
Figure 1-6 (a) Representative optical image of mono- and few-layer MoS_2 crystals on a silicon substrate with etched holes of 1.0 and 1.5 μm in diameter. (b) PL image of the same samples. The PL QY is much enhanced for suspended regions of the monolayer samples, and the emission from the few-layer sample is too weak to be seen in this image. ⁴²	10
Figure 1-7 Lattice structure of MoS_2 in both the in- and out-of-plane directions and simplified band structure of bulk MoS_2 . A and B are the direct gap transitions at K valley, $E_{g'}$ is the indirect gap near Γ valley and E_g is the direct gap at H valley. ⁴²	11
Figure 1-8 Spin degeneracy at the valence-band edges is lifted by the spin-orbit interactions, and K and K' valleys show time reversal symmetry. ⁴⁵	12
Figure 2-1 Dr. Theodore Maiman with the first working Ruby laser. (Photographed by HRL Laboratories, LLC)	14

Figure 2-2 Demonstration of the anisotropic bond model (ABM). 16

Figure 2-3 (a) Energy level scheme of SHG process. (b) Potential diagram of a bounded electron..... 17

Figure 2-4 The Horse in Motion, photographed with an array of 12 cameras in a line by Eadweard Muybridge..... 21

Figure 2-5 Diagram of pump-probe experiment. 22

Figure 3-1 Picture of Zr (0001)..... 26

Figure 3-2 Diagram of SHG setup. 28

Figure 3-3 (a) Residual Gas Analysis inside UHV chamber. (b) Zr(0001) under sputtering. . 29

Figure 3-4 AES before (black) and after (red) sputtering. 31

Figure 3-5 Picture of SHG experiment combined with UHV chamber: the arrowed lines indicate the path of 800 nm laser into the UHV chamber..... 32

Figure 3-6 Oxygen atoms are in octahedral sites in alternative layers on the interface of Zr/ZrO₂..... 33

Figure 3-7 ABM simulation of SHG from a perfect interface between Zr and its oxide film. 34

Figure 3-8 SHG anisotropy of as-received Zr (0001) single crystal..... 34

Figure 3-9 SHG anisotropy on as grown Ti. (a) P-P (black) and P-S (red) geometries. (b) S-S (black) and S-P (red) geometries. 35

Figure 3-10 SHG anisotropy after chemical etching..... 36

Figure 3-11 SHG anisotropy after fine polishing. (a) P-P geometry. (b) S-S geometry..... 36

Figure 3-12 AES upon oxidation of fresh Zr in ambient environment of UHV. 38

Figure 3-13 Change of Zr and O peaks in AES upon exposure of fresh Zr in ambient environment of UHV. 38

Figure 3-14 Diagram of Zr oxide on the surface of Zr 39

Figure 3-15 Change of ZrO₂ thickness along with the exposure in Langmuir (black dots). The fitting (red curve) using a single exponential function $y = A_0 + A_1 * e^{-x/\tau}$ gives $A_0 = 1.78 \pm 0.03$ nm, $A_1 = -1.81 \pm 0.03$ nm and $\tau = 10.8 \pm 0.5$ L..... 41

Figure 3-16 Change of SHG from Zr surface along with the exposure in Langmuir (black) with the fitting (red curve). The fitting (red curve) using a two exponential function $y = A_0 + A_1 * e^{-x/\tau_1} + A_2 * e^{-x/\tau_2}$ gives $A_0 = 1.079 \pm 0.004$, $A_1 = 22.88 \pm 0.08$, $\tau_1 = 0.360 \pm 0.002$ L, $A_2 = 4.21 \pm 0.05$ and $\tau_2 = 2.52 \pm 0.03$ L (adjusted $R^2 = 0.99773$). 42

Figure 3-17 Change of SHG from Zr surface along with the exposure in Langmuir (black) with the fitting (red curve). The fitting (red curve) using Equation 3-12 gives $I_0 = 25.73$, $R = 0.20$, $\tau_1 = 0.57$, $A_2 = 3.42$, $\tau_2 = 2.93$ (adjust $R^2 = 0.99847$)..... 45

Figure 3-18 Change of ZrO₂ thickness (black squares) and SHG (blue squares) along with the exposure in Langmuir (x-axis in log scale)..... 46

Figure 3-19 Normalized SHG Anisotropy from the Bi₂Se₃ (111) surface as a function of azimuthal angle ϕ . Measurements taken (a) 5 min and (b) 5 day after cleavage in ambient air. <1> P_{in}-P_{out}, <2> P_{in}-S_{out}, <3> S_{in}-P_{out}, <4> S_{in}-S_{out} indicate different incident and outgoing photon geometries..... 49

Figure 3-20 Time dependent SHG anisotropy after cleavage in ambient air for P_{in}-P_{out} geometry. 50

Figure 3-21 Evolution of SHG signal at high symmetric angles for different photon geometries. 51

Figure 3-22 Time dependent SHG at 0 ° and 60 ° for different Bi₂Se₃ samples. (a) Bi:Se = 0.62 (~6×10¹⁸ cm⁻³); (b) Bi:Se = 0.54 (~5×10¹⁷ cm⁻³) after cleavage in ambient air in P_{in}-P_{out} photon geometries. 52

Figure 3-23 Time dependent SHG intensity with Bi₂Se₃ (Bi:Se = 0.62) cleaved in N₂ and kept for 25.23 h before exposure to ambient air at the time indicated by the dashed line. 54

Figure 3-24 Time dependent SHG intensity with Bi₂Se₃ (Bi:Se = 0.62) cleaved in zero-air and kept for 25.38 h before exposure to ambient air at the time indicated by the dashed line. 55

Figure 3-25 Schematic depiction of the different regimes of time evolution of the surface electric field considered in the discussion section. The top and bottom panels are schematics of the crucial physical processes in each regime and the time evolution of SHG intensity, respectively. Regime I involves gradual band bending due to redistribution of Se vacancy donors and their associated conduction band electrons. Region II shows surface adsorption of ambient gases where the arrow indicates arrival of a molecule (H₂O here, can also be N₂ or O₂) to the surface from the gas phase. Region III depicts more extensive surface oxidation where a clear chemical bond is drawn between O atoms and the surface. 56

Figure 3-26 Diagram of Transient Reflection Spectroscopic Microscopy (TRSM). 66

Figure 3-27 Dramatically improved PL efficiency of suspended monolayer MoS₂ and WS₂. (a) Optical image of a typical suspended monolayer. Inset: optical image of as-grown monolayers with a scale bar of 10 μm. (b) PL mapping of a typical suspended monolayer. The colorbar of PL intensity is in log scale. (c) PL spectra of as-grown monolayer MoS₂, suspended monolayer MoS₂, and the monolayer MoS₂ transferred onto SiO₂/Si substrates. The spectra of the as-grown monolayer and the monolayer MoS₂ transferred onto SiO₂/Si

substrates are multiplied by 50 for visual convenience. (d) PL spectra of as grown monolayer WS₂, suspended monolayer WS₂, and the monolayer WS₂ transferred onto SiO₂/Si substrates. The spectra of the as-grown monolayer and the transferred monolayer on SiO₂/Si substrates are multiplied by 25 and 50, respectively, for visual convenience. 70

Figure 3-28 Exciton dynamics of suspended and supported monolayers. The normalized DR of the probe pulse from (a) suspended and as-grown MoS₂ monolayers and (b) suspended and as-grown WS₂ monolayers as a function of the probe delay. The insets are magnified versions for the measured results around the zero-ps decay. Both experimental (dotted lined) and fitted (solid lines) results are plotted..... 72

Figure 3-29 Dependence of transient reflection $\Delta R/R$ of suspended monolayers on pump fluence. (a) For suspended MoS₂ monolayer and (b) For suspended WS₂ monolayer. The $\Delta R/R$ at the peak is linearly dependent on the pump fluence, and this indicates no substantial heating effect with the applied pump fluence. 73

Figure 3-30 Dependence of transient reflection $\Delta R/R$ of as-grown monolayers (sapphire substrates) on pumping fluence. (a) For MoS₂ monolayer and (b) For WS₂ monolayer. The $\Delta R/R$ at the peak is linearly dependent on the pump fluence, and this indicates no substantial heating effect with the applied pump fluence. 74

Figure 3-31 Independence of the transient reflection $\Delta R/R$ on pumping fluence and temperature. Normalized differential reflection $\Delta R/R$ of (a) as-grown monolayer MoS₂ and (b) as-grown monolayer WS₂ on sapphire substrates as a function of pumping fluence. Normalized differential reflection $\Delta R/R$ of (c) as-grown monolayer MoS₂ and (d) as-grown monolayer WS₂ on sapphire substrates as a function of temperatures, 75K, 150K, 220K, and 295K. The result indicates negligible dependence of the differential

reflection on the pumping fluence and temperature, suggesting the dominance of defect-assisted recombination as reported previously. 76

Figure 3-32 Comparable exciton dynamics in the supported monolayer MoS₂ on typical substrates. Normalized transient reflection $\Delta R/R$ shows similar decay trends for all the supported monolayers. 77

Figure 3-33 Substrate-dependent PL efficiency of supported monolayers. (a) PL spectra of monolayers MoS₂ on typical substrates. (b) Raman spectra of monolayers MoS₂ on different substrates. The two dashed lines indicate the E¹_{2g} and A_{1g} peaks of the as-grown monolayer. (c) Calculated charge transfer between monolayer MoS₂ and mica substrate, which shows plane-averaged differential charge density $\Delta\rho$ (red line) and amount of transferred charge ΔQ (blue line) as a function of the distance in the vertical direction. Also shown is a sideview of the structure used in the calculation (right)..... 79

Figure 3-34 Dependence of the exciton dynamics on pumping fluence for suspended MoS₂ monolayers. (a) Normalized differential reflection of suspended MoS₂ as a function of the time delay and with different pumping fluences, 1.5 $\mu\text{J}/\text{cm}^2$ (red), 2.5 $\mu\text{J}/\text{cm}^2$ (black), and 5.0 $\mu\text{J}/\text{cm}^2$ (blue). Inset: the results for the early stage of the decay. (b) The result of $(\Delta R/R)_0/(\Delta R/R)_t - 1$ derived from the data in (a) as a function of the delay time. The result for the pumping fluence of 5.0 $\mu\text{J}/\text{cm}^2$ is not shown for the visual convenience. (c) Fitting for the measured differential reflection of suspended MoS₂ with different pumping fluences, The fitted results are plotted in dashed lines and the experimental results are dots, 1.5 $\mu\text{J}/\text{cm}^2$ (red), 2.5 $\mu\text{J}/\text{cm}^2$ (black), and 5.0 $\mu\text{J}/\text{cm}^2$ (blue). 82

Figure 3-35 Dependence of the exciton dynamics on pumping fluence for suspended WS₂ monolayers. (a) Normalized differential reflection of suspended WS₂ as a function of the

time delay and with different pumping fluences, $1.5 \mu\text{J}/\text{cm}^2$ (red), $2.5 \mu\text{J}/\text{cm}^2$ (blue), and $5.0 \mu\text{J}/\text{cm}^2$ (black). Inset: the results for the early stage of the decay. (b) The result of $(\Delta R/R)_0/(\Delta R/R)_t - 1$ derived from the data in (a) as a function of the delay time. The dashed line serves to illustrate the slope of the result. (c) Fitting for the measured differential reflection of suspended WS_2 with different pumping fluences, The fitted results are plotted in dashed lines and the experimental results are dots, $1.5 \mu\text{J}/\text{cm}^2$ (red), $2.5 \mu\text{J}/\text{cm}^2$ (blue), and $5.0 \mu\text{J}/\text{cm}^2$ (black)..... 83

Figure 3-36 Dependence of the exciton dynamics on pumping fluence for as-grown MoS_2 monolayers. (a) Normalized differential reflection of as-grown MoS_2 as a function of the time delay and with different pumping fluences, $25 \mu\text{J}/\text{cm}^2$ (red), $50 \mu\text{J}/\text{cm}^2$ (black), and $100 \mu\text{J}/\text{cm}^2$ (blue). Inset: the results for the early stage of the decay. (b) The result of $(\Delta R/R)_0/(\Delta R/R)_t - 1$ derived from the data in (a) as a function of the delay time. The result for the pumping fluence of $100 \mu\text{J}/\text{cm}^2$ is not shown for the visual convenience. (c) The non-normalized differential reflection of as-grown MoS_2 at pumping fluence $25 \mu\text{J}/\text{cm}^2$ (red), $50 \mu\text{J}/\text{cm}^2$ (black), and $100 \mu\text{J}/\text{cm}^2$ (blue). 84

Figure 3-37 Dependence of the exciton dynamics on pumping fluence for as-grown WS_2 monolayers. (a) Normalized differential reflection of suspended WS_2 as a function of the time delay and with different pumping fluences, $10 \mu\text{J}/\text{cm}^2$ (red), $25 \mu\text{J}/\text{cm}^2$ (black), and $50 \mu\text{J}/\text{cm}^2$ (blue). Inset: the results for the early stage of the decay. (b) The result of $(\Delta R/R)_0/(\Delta R/R)_t - 1$ derived from the data in (a) as a function of the delay time. The result for the pumping fluence of $50 \mu\text{J}/\text{cm}^2$ is not shown for the visual convenience. (c) Fitting for the measured differential reflection of as grown WS_2 with different pumping fluences,

The fitted results are plotted in dashed lines and the experimental results are dots, 10 $\mu\text{J}/\text{cm}^2$ (red), 25 $\mu\text{J}/\text{cm}^2$ (black), and 50 $\mu\text{J}/\text{cm}^2$ (blue). 85

Fig. A-1 Diagram of the laser system. 103

Fig. A-2 Cross correlation of pump and probe pulses. 103

Fig. B-1 Knife edge measurement (black dots) of the focused beam using a 50X long working distance objective. The fitting (blue curve) using Eq. B-10 gives $p_1 = 5.67 \mu\text{W}$, $p_2 = -0.45 \mu\text{m}$ and $p_3 = 1.41 \mu\text{m}$ 107

LIST OF ABBREVIATIONS

2D	2 Dimensional
ARPES	Angle Resolved Photo-Electron Spectroscopy
ABM	Anisotropic Bond Model
AFM	Atomic Force Microscopy
AES	Auger Electron Spectroscopy
DA	Differential Absorption
DFT	Density Functional Theory
DR	Differential Reflection
EEA	Exciton-Exciton Annihilation
EFISH	Electric Field Induced Second Harmonic
GSB	Ground State Bleaching
HCP	Hexagonal Close-Packed
LASRE	Light Amplification by Stimulated Emission of Radiation
MPM	Macroscopic Phenomenological Model
PMT	Photo Multiplier Tube
PIA	Photo-Induced Absorption
PS	Polystyrene
QY	Quantum Yield
R6G	Rhodamine-6g
SHG	Second Harmonic Generation
SE	Stimulated Emission
SFCC	Surface Face-Centered Cubic
TEM	Transmission Electron Microscopy
TRSM	Transient Reflection Spectroscopic Microscopy
TI	Topological Insulator
TSS	Topological Surface States
TA	Transient Absorption

TR	Transient Reflection
TMDC	Transition Metal Dichalcogenide
TEM	Transmission Electron Microscopy
UHP	Ultra-High Purity
UHV	Ultra-High Vacuum
XPS	X-ray Photoelectron Spectroscopy
Zr	Zirconium

Chapter 1 Introduction

1.1 Background

As most of the physical and chemical processes take place on surfaces and interfaces, there are urgent demands for understanding these processes. For example, the thin oxide film on Si plays a crucial role on its performance in devices, and the most commonly used method to characterize the dielectric properties of thin films is ellipsometry. However, ellipsometry has limited sensitivity to the interface underlying its oxide film. For this purpose, the nonlinear optical tool, SHG and its related methodology have been exploited to investigate the buried interface on Si.¹⁻⁵

As comes to the material platform, devices based on traditional bulk semiconductors (such as Si and GeAs), have several blooming decades since their birth. Nevertheless, as they are getting compacter, the necklace seems to be touched because of their limit in density, considering the thermal conduction and device-to-device interference. Hence, people are pursuing more efficient materials to satisfy the unmet needs beyond the scope of traditional semiconductors.

The finding of graphene opened a new decade for 2D-materials. Figure 1-1 shows a transistor made using exfoliated graphene from a lump of graphite. The unprecedented physical properties on atomically scaled graphene triggered a realm of rediscovering existing materials, in their 2D-state. Such novel 2D-materials have superior physical properties and compactness that cannot be matched by traditional materials.



Figure 1-1 A lump of graphite, a graphene transistor and a tape dispenser. Donated to the Nobel Museum in Stockholm by Andre Geim and Konstantin Novoselov in 2010.

As these 2D-materials have dimensions in the atomic scale, the characterizations seem to be challenging. Traditional methods are not applicable on these materials because of their small scale and fragility. Therefore, more new methods need to be developed to characterize these new 2D-materials.

Driven by those challenges in surface and interface characterization, during my PhD study, I exploited nonlinear optical methods to investigate three categories of materials, Zr, TI (Bi_2Se_3), and TMDC (MoS_2 and WS_2) monolayers.

First, I started with employing SHG to study the bonding on the interface between Zr and its protective oxide film. Moreover, I investigated the initial oxidation of fresh Zr in UHV with SHG after the successful removal of the oxide film. Second, by controlling the

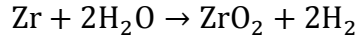
gaseous environment, I used SHG to investigate the near surface physical and chemical processes on Bi_2Se_3 . Lastly, to understand the exciton dynamics on MoS_2 and WS_2 monolayers, I developed Transient Reflection Spectroscopic Microscopy (TRSM), which yields real time imaging on these monolayers in micrometer scale.

1.2 Zirconium (Zr)



Figure 1-2 Nuclear fuel cladded by Zr alloys.

Zr has a unique combination of properties such as strong mechanical resistance and low neutron-capture cross-section. Thus Zr alloys are chosen as the cladding material (Figure 1-2) in commercial nuclear fission reactors. Zr is highly reactive to oxygen and water, while the native dense oxide film around Zr plays a crucial role in its corrosion resistance as a barrier. However, under high temperatures, the phase change (from cubic to tetragonal to monoclinic) of ZrO_2 can introduce large stresses that are responsible for the crack formation on the oxide cladding⁶. Under high temperatures, severe cracking will lead to the rapid formation of hydrogen and accelerated degradation of the fuel cladding:



Equation 1-1

The accident in Fukushima Nuclear Power Plant on Mar 11, 2011 occurred due to the interruption of cooling by the earthquake and tsunami disaster, leading to the accumulation of hydrogen through the reaction in Equation 1-1, which was responsible for the explosion inside the reactor. To better optimize and stabilize the property of Zr and its protective oxide film, many experimental and theoretical tools have been applied to learn the oxidation of Zr in clarifying the detailed processes. Spectral ellipsometry and X-ray photoelectron spectroscopy (XPS) experiments have been conducted to investigate the dependence of oxide growth kinetics for different crystallographic orientations on temperature and on oxygen partial pressure^{7,8}. A detailed study⁹ shows that there are two stages during the oxidation of Zr: while in the first and fast stage, a Zr suboxide interlayer is formed containing three suboxide components (Zr^{+1} , Zr^{+2} and Zr^{+3}); and a stoichiometric ZrO_2 overlayer grows in a second, slow stage. These suboxides stay in the interface with the stoichiometric ZrO_2 on top. Auger electron spectroscopy (AES) and followed theory¹⁰ have proved that these suboxides give further opportunities for oxidation. As a result, stress builds up on the interface resulting in cracking in the oxide film as transmission electron microscopy (TEM) observed¹¹. The inner interface plays an important role in protecting the structure of Zr or Zr alloys. Raman scattering study¹² suggests that the inner oxide composes of mostly tetragonal crystallites and while the external layer is monoclinic. A debates exists here because tetragonal form of ZrO_2 is not stable below 1400 K. One potential explanation is that tetragonal structure is only stable in the form of small crystallites (<30 nm) and the surface energy may change the

thermodynamic energy. Another significant factor is the compressive strain built up during the growth, which could change the thermodynamic stability as well, since it exists along the plane of interface, and is free in the normal direction.

1.3 Topological Insulator (TI)

In recent years it has been discovered that a very useful method of categorizing insulating solids is by topological invariants of their bulk band structure.¹³⁻¹⁵ These invariants are reflected in unique electronic surface states that are "protected" by symmetry and that are of interest for spintronic¹⁶ and quantum computing¹⁷ applications. Solids with strong spin-orbit coupling often have nontrivial topological invariants that require the existence of unique topological surface states (TSS's).¹⁸⁻²⁰ As the analogy²¹ in Figure 1-3, surface states acts as the bridge of nontrivial and trivial TIs due to the abrupt change in topology.

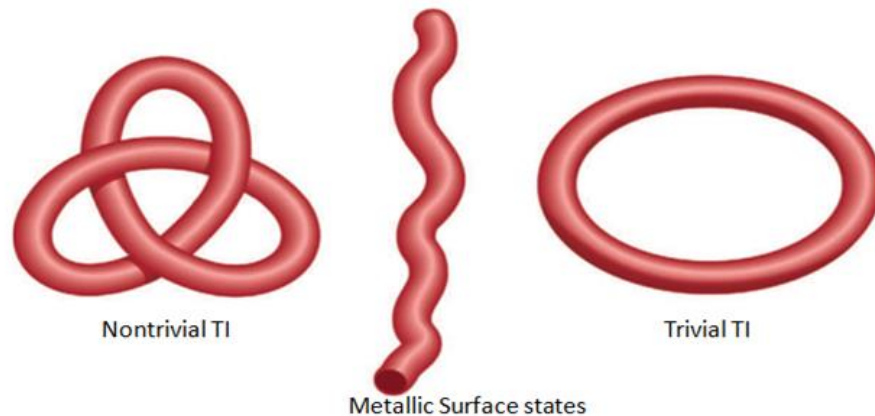


Figure 1-3 One analogy of topological surface states between trivial TI and nontrivial TI.

These TSS's have special properties such as linear dispersion²² and spin²³ and orbital angular momentum²⁴ "textures" correlated with crystal momentum. Furthermore, due to

their origination from bulk invariants, they are insensitive to non-magnetic surface perturbations²⁵ and thus robust enough to be of potential value in applications. The most valuable experimental probe of these states has been angle resolved photoelectron spectroscopy (ARPES) due to its extraordinary surface sensitivity and ability to produce direct band structure maps.²⁶ Recent ARPES measurements confirmed existence of TSS for several TI crystals. Among those, Bi_2Se_3 is a TI that has one single Dirac cone and a relative large bulk band gap ~ 300 meV.^{21-23, 27, 28} Bulk Bi_2Se_3 has layered structure, with every five atomic layers consisting one quintuple layer as indicated in Figure 1-4(a). Within the quintuple layer, the bondings are covalent; between quintuple layers, they are connected through van der Waals interaction. With mechanical exfoliation, Bi_2Se_3 can be easily cleaved between quintuple layers. Figure 1-4(b) and (c) illustrate the band structure of Bi_2Se_3 and its Brillouin zone.

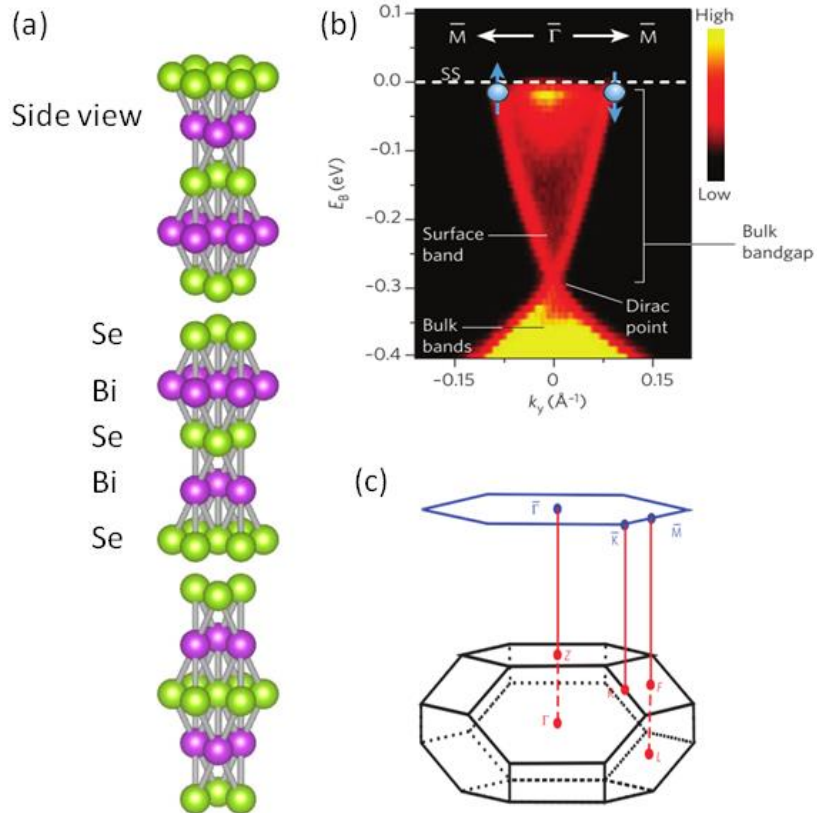


Figure 1-4 (a) Structure of crystalline Bi_2Se_3 . (b) The electronic structure of Bi_2Se_3 as measured by ARPES, showing the signatures of the exotic metallic surface states in TI.^{21, 22, 29} (c) Brillouin zone for Bi_2Se_3 with space group $R\bar{3}m$.²⁸

By contrast, less experimental progress has been made in directly observing the electrical transport properties of charge carriers in TSS's because of simultaneous contributions from bulk and surface carrier transport due to heavy-doping from Se vacancies.^{30, 31} In addition, ARPES measurements have shown that downward band bending near the surface creates an inversion layer that supports topologically trivial 2D electron gas states.³² Only a few experiments on very thin, exfoliated samples that have surfaces modified by strong acceptor layers have shown evidence for ambipolar transport in the Dirac-like surface state band on Bi_2Se_3 .³³ Intentional bulk doping of Bi_2Se_3 (e.g., with Ca ³¹ or As ^{34, 35}) has also been used to compensate heavy n-doping due to Se vacancies that are prevalent after crystal growth. This has the goal of moving the Fermi

level into the bulk band gap to enhance the sensitivity of electrical transport measurements of the TSS.³¹

In addition to intrinsic doping effects, the near surface electric fields in Bi_2Se_3 are also influenced by adsorbed molecules from the environment. This inspires one way to access the electrical carrier transport on Dirac-like surface band by tuning Fermi level towards the Dirac point inside the band gap through surface molecule adsorption. As one example in Figure 1-5, the Fermi level is tunable via surface oxygen doping³⁶. However, the general reactivity of the Bi_2Se_3 surface to ambient gases is a complex topic. Though correlations between Fermi level shifts and residual gas exposure have been made,³⁷ the Bi_2Se_3 surface is remarkably inert to oxidation by individual adsorbed gases.³⁸⁻⁴⁰ Significant oxidation occurs only in the presence of both water and oxygen⁴⁰ such as found in ambient conditions.⁴¹

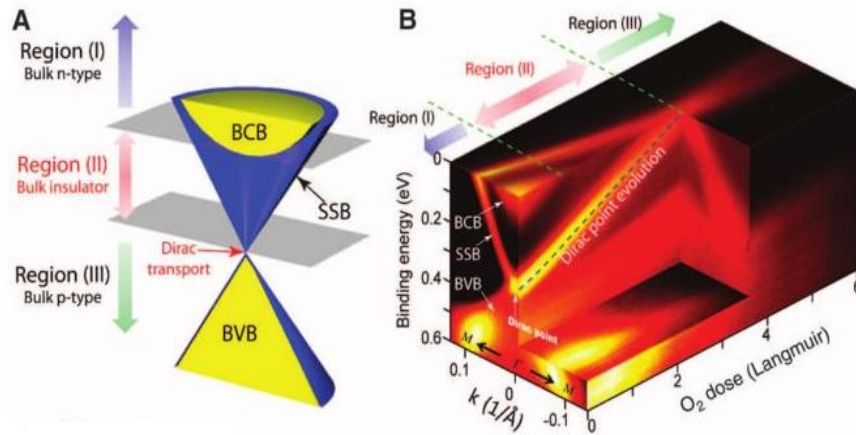


Figure 1-5 (A) Different carrier type regions. (B) Evolution of Fermi level by photon-assisted surface doping by oxygen.

In order to understand the complex interplay of electric fields, dopant distribution, and surface adsorbate effects near TI surfaces the technique of SHG is a valuable tool.⁴²⁻

⁴⁴ Pioneering work using SHG on Bi₂Se₃ by Hsieh et al. has shown significant charge transfer process over time near the solid surface (~10 nm) after a mechanical cleave in ambient air.³⁴ SHG is a surface-sensitive probe of this material that is particularly valuable for investigating near-surface electric fields due to band bending that breaks bulk inversion symmetry and allows SHG. To this end, this so-called electric field induced second harmonic (EFISH) generation has been used extensively to study electric fields at semiconductor surfaces.^{44, 45}

In the case of Bi₂Se₃, it was found that near surface charge transfer arises from downward band bending^{34, 35} similar to that observed in ARPES⁴⁶⁻⁴⁸ and can saturate in less than 100 min in ambient air. Moreover, cleaving samples in an O₂ environment dramatically changes the qualitative character of the time dependence due to the acceptor character of O₂ adsorbates.^{34, 35} This has led to the conclusion that EFISH in Bi₂Se₃ acts as a sensitive probe of the near surface electric field that complements other experimental techniques.

1.4 Transition Metal Dichalcogenide (TMDC) Monolayers

The ultra-high carrier mobility in excess of $2 \times 10^5 \text{ cm}^2/(\text{V}\cdot\text{s})$ ⁴⁹ on graphene implied possible applications on novel devices. However, the current frame of switching device fabrication found its limitations on utilizing graphene due to its absence of band gap on the Dirac point^{50, 51}. While some scientists are looking for means to open the gap by introducing small perturbations on graphene⁵²⁻⁵⁵, other scientists now turned their wheels towards other 2D-materials. The transition of indirect band gap to direct band gap in the visible wavelength region on MoS₂ with decreasing thickness, and the improved

photoluminescence (PL) quantum yield (QY) by more than 10^4 declared a new era of 2D materials for optical and electrical devices⁵⁶.

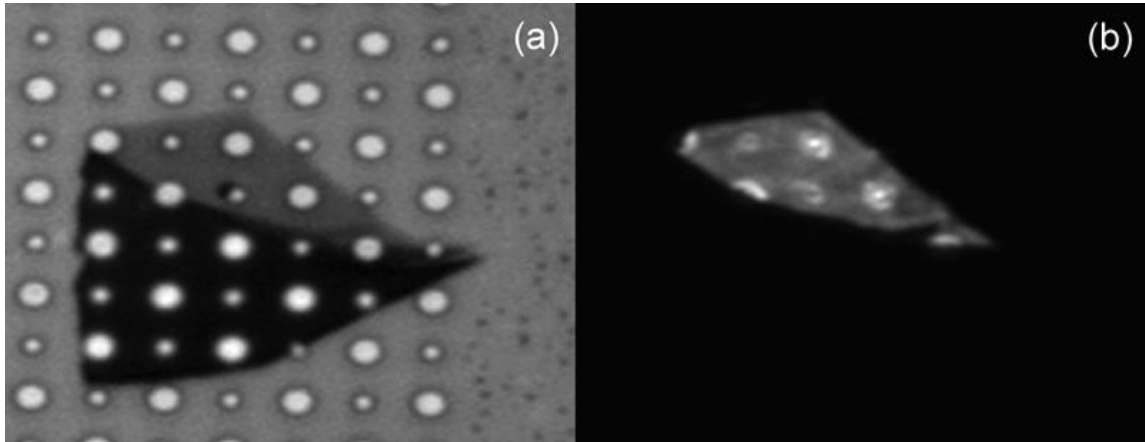


Figure 1-6 (a) Representative optical image of mono- and few-layer MoS₂ crystals on a silicon substrate with etched holes of 1.0 and 1.5 μm in diameter. (b) PL image of the same samples. The PL QY is much enhanced for suspended regions of the monolayer samples, and the emission from the few-layer sample is too weak to be seen in this image.⁵⁶

As shown in Figure 1-6, the PL is much enhanced on the MoS₂ monolayer in the PL image. The mystery implies in the upward energy shift (E'_g in Figure 1-7) by more than 0.6 eV from bulk to monolayer, shifting into direct gap at K valley.

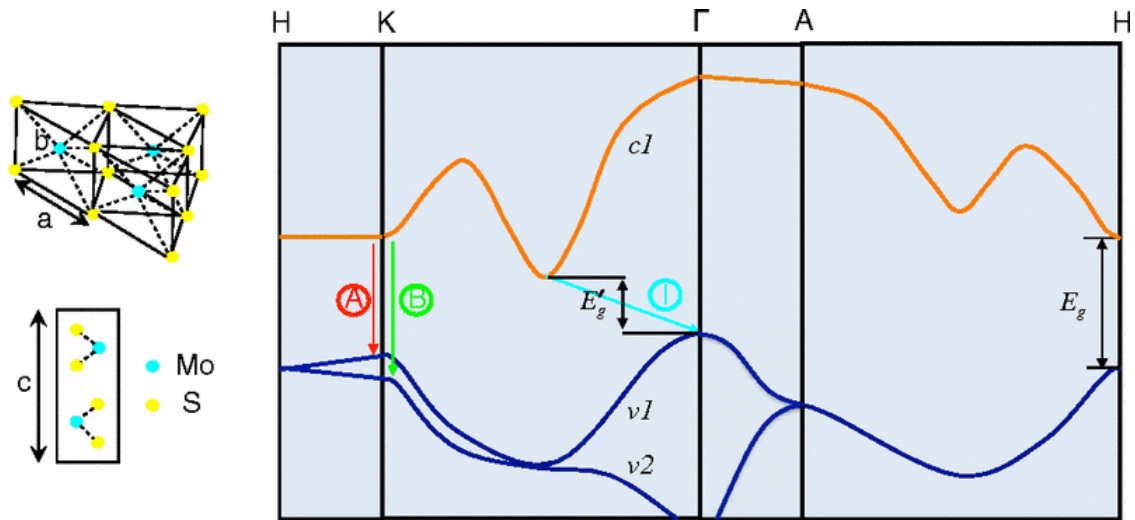


Figure 1-7 Lattice structure of MoS₂ in both the in- and out-of-plane directions and simplified band structure of bulk MoS₂. A and B are the direct gap transitions at K valley, E_g^{Γ} is the indirect gap near Γ valley and E_g^h is the direct gap at H valley.⁵⁶

What's more, the strong spin-orbit coupling from inversion symmetry break induces the spin splitting at K valley and K' valleys (Figure 1-8) with relatively high energy (148 meV⁵⁷) in valence band maximum. Valley polarization has been found on MoS₂ monolayer by selective optical pumping^{58, 59}. Ultrafast transient absorption⁶⁰ or reflection⁶¹ confirmed that hole valley relaxation will last about several picoseconds, implying potential applications in valley spintronics devices.

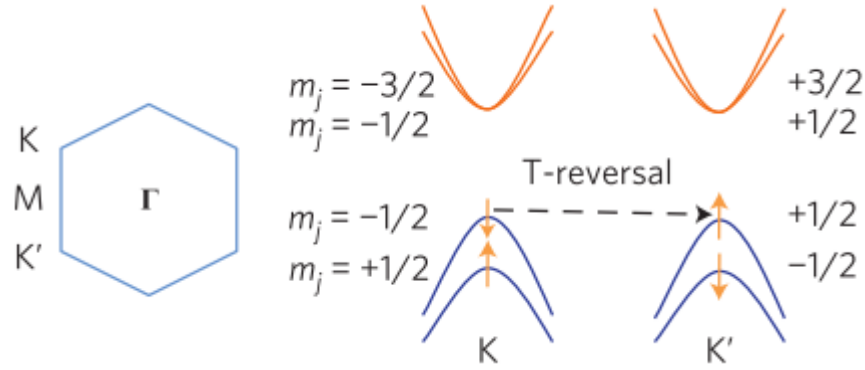


Figure 1-8 Spin degeneracy at the valence-band edges is lifted by the spin-orbit interactions, and K and K' valleys show time reversal symmetry.⁵⁹

The generalization can also be extended into other TMDC materials, such as MoSe₂⁶², WS₂⁶³ and WSe₂⁶², which were found to have similar properties as MoS₂.

With their pristine properties, TMDC materials present an atomic scale semiconductor platform that promises for scaling of semiconductor devices to truly atomic level.^{64-70,71} For the same reason, the atomically thin 2D TMDC materials makes the device development very challenging. Both the stability of 2D TMDC materials and the impact of external environment are important before further device development. In particular, the functionalities of 2D TMDC devices are strongly susceptible to the influence of substrates.⁷²⁻⁷⁵ As substrates are often required to support and house 2D TMDC devices, it is necessary to thoroughly understand the effects of substrates on them. Progress has been achieved in understanding the substrate effect^{74, 76-79}. For instance, substrates have been reported to affect luminescence of TMDC monolayers by introducing strain or doping.^{77, 80-83}

By contrast, less experimental progress has been made on directly observing the photoexcited exciton relaxations on different substrates⁸⁴. Transient absorption/reflection (TA/TR) have been demonstrated as a useful tool in characterizing the exciton formation

and relaxation⁸⁵⁻⁹¹ on TMDC monolayers. By selecting the pump and probe energies, different physical processes could be characterized.

In order to understand the detailed exciton recombination processes on different substrates, TA/TR would be a useful tool. A recent work by Wang⁸⁴ resolved the slightly differences in exciton dynamics between supported and suspended MoS₂ mono- and few-layers. However, the substrate conditions were not well controlled, such as the chemical properties, which will have a significant impact on the doping level of MoS₂ monolayer. And also the size of the suspended area was as small as $\sim 1 \mu\text{m}$, similar to or smaller than the size of laser beam, thus the contribution from the edge or the supported region cannot be dismissed. A comprehensive study is still necessary to clarify the effects of substrates using ultrafast TA/TR spectroscopy.

1.5 Outline

This thesis is organized as follows:

In Chapter 2, fundamental theories about nonlinear optics are introduced, including SHG and TA/TR.

In Chapter 3, my experimental results are presented and discussed on the three categories of materials.

In Chapter 4, there are a summary of all my works and my proposal on future works.

Chapter 2 Theory of Nonlinear Optics

2.1 Second Harmonic Generation (SHG)

2.1.1 Brief history of SHG

With the invention of the first laser by Theodore Maiman⁹² (Figure 2-1), one of its important applications on the light-matter interactions is SHG, which was observed first by Peter Franken and his coworkers in the Randall Laboratory at the University of Michigan⁹³. The formulation of SHG was initially elucidated by N. Bloembergen and P. S. Pershan at Harvard in 1962⁴². With the aid of well-developed ultrafast lasers, non-destructive SHG probing is possible on novel materials.



Figure 2-1 Dr. Theodore Maiman with the first working Ruby laser. (Photographed by HRL Laboratories, LLC)

2.1.2 SHG on interface

Due to the inversion symmetry of most crystals and poly-crystals, SHG in the bulk can be suppressed ($\chi_2 = \mathbf{0}$ in the bulk), thus SHG can only be contributed from the surface or interface where the inversion symmetry is broken. This makes SHG extremely sensitive to the surface or interface. SHG has been proven to be an important tool in studying surface or interface on traditional semi-conductors (Si⁹⁴) and novel 2D semi-conductors (MoS₂⁹⁵⁻⁹⁷ and WS₂⁹⁸).

2.1.3 Microscopic bond model – Anisotropic Bond Model (ABM)

An instructive model of SHG is the anisotropic bond model (ABM)⁹⁹. The calculation of SHG can be separated into 3 steps (demonstrated in Figure 2-2):

1. Solve the force equation of the charge for each bond.
2. Calculate the far field radiation from the motion of the charge for each bond.
3. Combine the radiation from each bond together coherently.

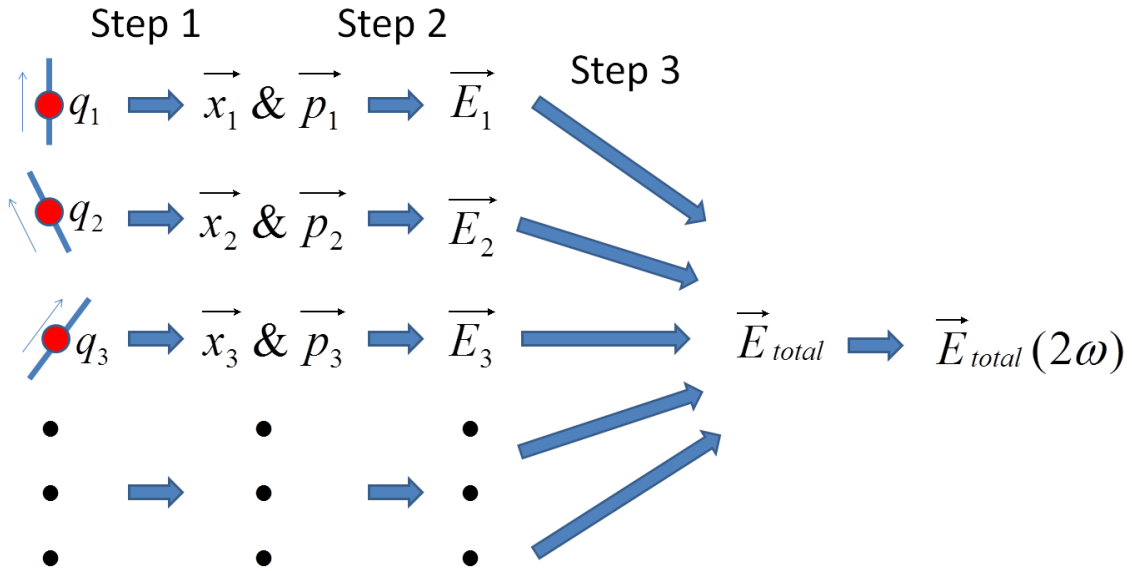


Figure 2-2 Demonstration of the anisotropic bond model (ABM).

A diagram of SHG is shown in Figure 2-3 (a). Figure 2-3 (b) is the potential diagram of a bounded electron. When the electron motion is small, as shown in Figure 2-3 (b), the potential of the electron can be approximated by the parabolic curve:

$$V(x) = \frac{1}{2} * \kappa_1 * (x - x_0)^2$$

Equation 2-1

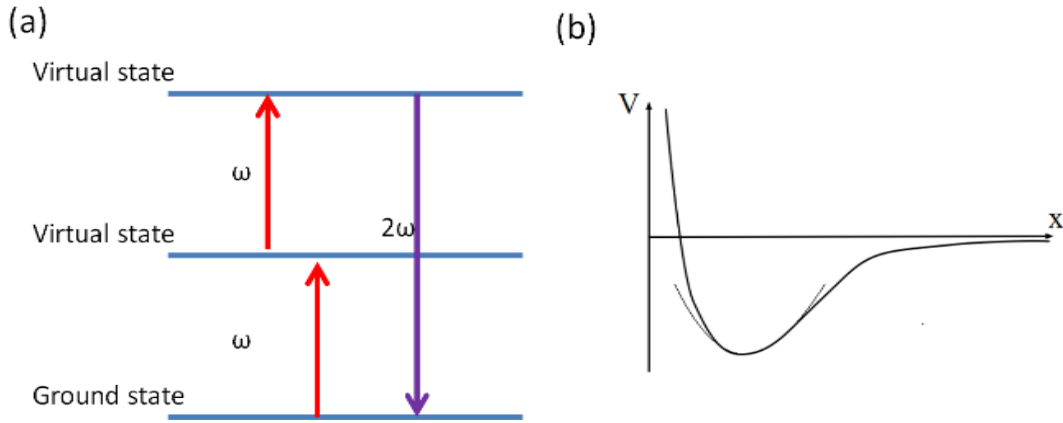


Figure 2-3 (a) Energy level scheme of SHG process. (b) Potential diagram of a bounded electron.

κ_1 is the harmonic spring constant, x is the position of the electron, and x_0 is its equilibrium position. The electron-light interaction problem can be solved easily as a harmonic oscillation problem. When the electron-light interaction is greater, to yield better approximation, a second term must be introduced to approximate the true potential¹⁰⁰:

$$V(x) = \frac{1}{2} * \kappa_1 * (x - x_0)^2 + \frac{1}{3} * \kappa_2 * (x - x_0)^3$$

Equation 2-2

κ_2 is the anharmonic spring constant. After including the charge q_j , the friction (with coefficient - b) and the applied electric field ($\vec{E}e^{-i\omega t}$), with the simple 1D force model, the force on the electron along the bonding direction \hat{b} will be⁹⁹:

$$F = q_j \vec{E} \cdot \hat{b} e^{-i\omega t} - \kappa_1 * (x - x_0) - \kappa_2 * (x - x_0)^2 - b \frac{dx}{dt} = m \frac{d^2 x}{dt^2}$$

Equation 2-3

Solve Equation 2-3 and we can get:

$$\mathbf{x} = \mathbf{x}_0 + \Delta x_1 e^{-i\omega t} + \Delta x_2 e^{-2i\omega t}$$

Equation 2-4

The linear term $\mathbf{p}_{1j} = \mathbf{q}_j \Delta x_1$ and the first order nonlinear term $\mathbf{p}_{2j} = \mathbf{q}_j \Delta x_2$ of the induced dipole $\vec{\mathbf{p}}_j = \mathbf{q}_j \Delta \vec{\mathbf{x}}_j$ are given:

$$\mathbf{p}_{1j} = \mathbf{q}_j \Delta x_1 = \frac{q_j^2 \vec{\mathbf{E}} \cdot \hat{\mathbf{b}}_j}{\kappa_1 - m\omega^2 - ib\omega} = \alpha_{1j} (\hat{\mathbf{b}}_j \cdot \vec{\mathbf{E}})$$

$$\mathbf{p}_{2j} = \mathbf{q}_j \Delta x_2 = \frac{q_j \kappa_2 \Delta x_1^2}{\kappa_1 - 4m\omega^2 - 2ib\omega} = \alpha_{2j} (\hat{\mathbf{b}}_j \cdot \vec{\mathbf{E}})^2$$

Equation 2-5

By combining different bondings together, the associated polarization per unit volume can be written as:

$$\vec{\mathbf{P}} = \chi_1 \cdot \vec{\mathbf{E}} + \chi_2 \cdot \vec{\mathbf{E}} \vec{\mathbf{E}}$$

Equation 2-6

The far-field radiation intensity can be expressed as:

$$\vec{\mathbf{E}}_{ff} = \frac{e^{ikr}}{r} [I - \hat{\mathbf{k}} \cdot \hat{\mathbf{k}}] \sum_j \vec{\mathbf{p}}_j$$

Equation 2-7

I is the unit tensor and $\hat{\mathbf{k}}$ is the unit vector in the direction of the observer. The far-field SHG is from the first order dipole component only:

$$\vec{\mathbf{E}}_{ff}(2\omega) = \frac{e^{ikr}}{r} [I - \hat{\mathbf{k}} \cdot \hat{\mathbf{k}}] \sum_j \vec{\mathbf{p}}_{2j}$$

Equation 2-8

A self-developed Matlab code for ABM is shown in Appendix D.

2.1.4 Macroscopic phenomenological model (MPM)

Besides ABM, the other well accepted model is the tensor based phenomenological model developed by Sipe et al.^{101, 102}, as mentioned above in Equation 2-6. The nonlinear electric field can be calculated once the nonlinear susceptibilities (the elements in χ_2) are known. The polarization can be expressed as:

$$\begin{pmatrix} P_x^{(2)} \\ P_y^{(2)} \\ P_z^{(2)} \end{pmatrix} = \begin{pmatrix} \chi_{xxx}^{(2)} & \chi_{xyy}^{(2)} & \chi_{xzz}^{(2)} & \chi_{xxy}^{(2)} & \chi_{xxz}^{(2)} & \chi_{xyz}^{(2)} \\ \chi_{yxx}^{(2)} & \chi_{yyy}^{(2)} & \chi_{yzz}^{(2)} & \chi_{yyx}^{(2)} & \chi_{yyz}^{(2)} & \chi_{yyz}^{(2)} \\ \chi_{zxx}^{(2)} & \chi_{zyy}^{(2)} & \chi_{zzz}^{(2)} & \chi_{zxy}^{(2)} & \chi_{zxz}^{(2)} & \chi_{zyz}^{(2)} \end{pmatrix} \begin{pmatrix} E_x E_x \\ E_y E_y \\ E_z E_z \\ 2E_x E_y \\ 2E_x E_z \\ 2E_y E_z \end{pmatrix}$$

Equation 2-9

Considering the macroscopic crystal symmetry of the medium, not all elements in the tensor χ_2 are independent. For instance, for the (111) surface of crystals with C_{3v} symmetry, such as Bi₂Se₃, when the y axis perpendicular to the plane of symmetry:

$$\begin{pmatrix} P_x^{(2)} \\ P_y^{(2)} \\ P_z^{(2)} \end{pmatrix} = \begin{pmatrix} \chi_{xxx}^{(2)} & -\chi_{xxx}^{(2)} & 0 & 0 & \chi_{xxz}^{(2)} & 0 \\ 0 & 0 & 0 & \chi_{xxz}^{(2)} & 0 & -\chi_{xxx}^{(2)} \\ \chi_{zxx}^{(2)} & \chi_{zxx}^{(2)} & \chi_{zzz}^{(2)} & 0 & 0 & 0 \end{pmatrix} \begin{pmatrix} E_x E_x \\ E_y E_y \\ E_z E_z \\ 2E_x E_y \\ 2E_x E_z \\ 2E_y E_z \end{pmatrix}$$

Equation 2-10

Now there are only four independent tensor elements: $\chi_{xxx}^{(2)}$, $\chi_{xxz}^{(2)}$, $\chi_{zxx}^{(2)}$ and $\chi_{zzz}^{(2)}$.

These elements can be determined by rotationally anisotropic SHG¹⁰³.

2.1.5 Electric Field Induced Second Harmonic (EFISH) Generation

SHG as described above neglects the effect of a DC electric field applied on the bulk, which may build up when there are charge traps on the surface or interface. With the DC electric field, the bulk inversion symmetry might be broken within its range, the new polarization from Equation 2-6 will be:

$$\vec{P}(2\omega) = \chi_2 \cdot \vec{E}\vec{E} + \chi_3 \cdots \vec{E}\vec{E}\vec{E}_{DC}$$

Equation 2-11

Usually, the SHG contribution from the second term in Equation 2-11 is small. However, when \vec{E}_{DC} is large enough, especially when there is an intrinsic DC electric field building up due to band bending in semi-conductors, EFISH will contribute significantly into the whole SHG. As a matter of fact, band bending can be monitored through EFISH¹⁰⁴ in this way.

2.2 Time Resolved Spectroscopy

2.2.1 Brief history of Pump-Probe experiment

As a famous prototype of high-speed photography, The Horse in Motion shows images of the horse with all feet off the ground. In Figure 2-4, Muybridge placed 12 cameras in a line along the edge of the track and the shutter of each was triggered by a thread as the horse passed. The motion of the horse was frozen while it passed through the camera, as the freezing time was limited by the shutter opening time in the order of milliseconds.

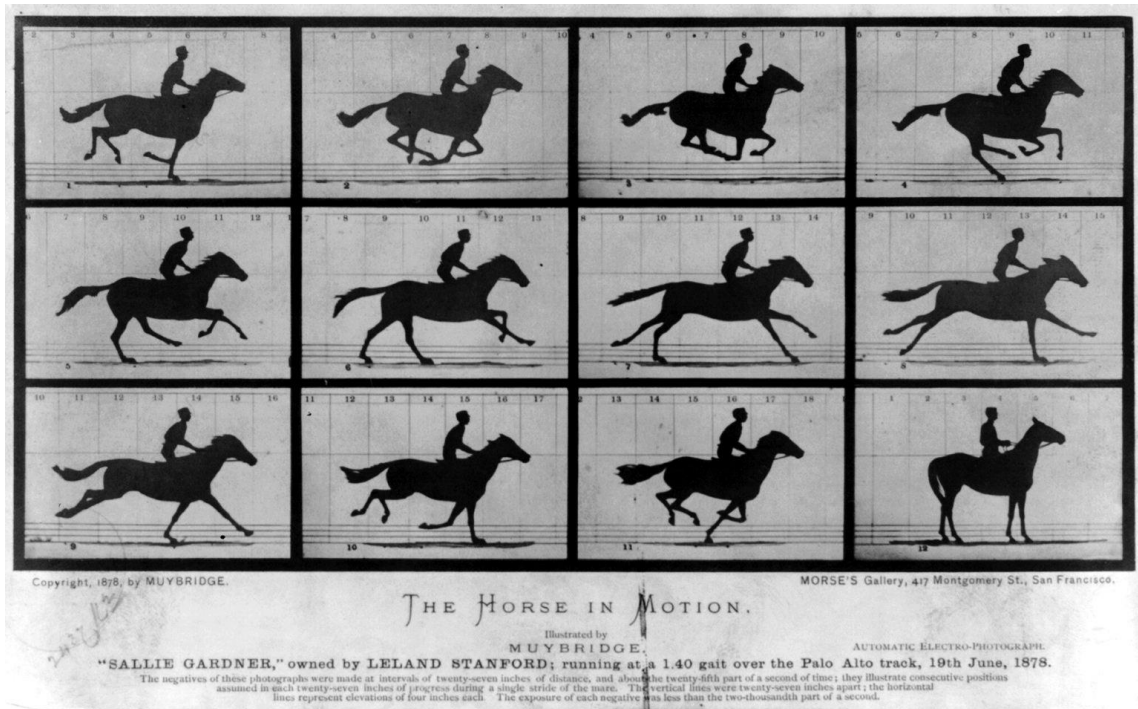


Figure 2-4 The Horse in Motion, photographed with an array of 12 cameras in a line by Eadweard Muybridge.

Similar ideas could be applied to optical pump-probe experiment (Figure 2-5), the process of a substance is clocked when it absorbs radiation from the pump pulse, which defines the zero time, as the horse passes the first camera. The passage of the second pulse—the probe pulse, through the substance at some later time point provides a snapshot of the status of the system at that time, as the horse passes through the following cameras. Thus the information of the substance after the pump excitation can be recorded with probe at different time delays controlled by the time spacing (t) between them, which is usually controlled by the spatial distance (d) between them ($t=d/c$, c is the speed of light), instead. Here, the resolution of pump-probe experiment is determined by the duration of the pulses, usually in the order of femtoseconds as most commercial ultrafast pulsed lasers can provide.

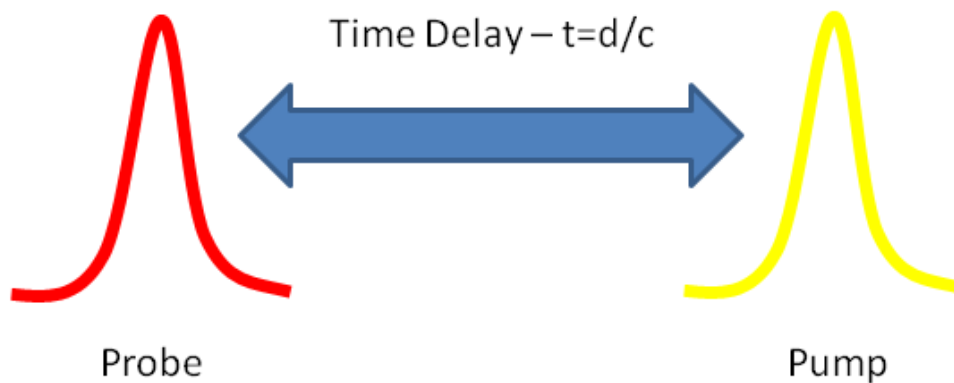


Figure 2-5 Diagram of pump-probe experiment.

2.2.2 Ultrafast Transient Absorption/Reflection (TA/TR) Spectroscopy

TA/TR measures the change in absorption/reflection of probe pulse due to the pump pulse. Since their similarity in nature, let's demonstrate TA first.

The change in absorption of the probe due to the pump is defined as:

$$\begin{aligned}
 & \textit{Absorbance}(\textit{of probe with pump})(A_{\textit{pump}}) \\
 & \quad - \textit{Absorbance}(\textit{of probe without pump})(A) \\
 & \quad = \Delta\textit{Absorbance}(\Delta A)
 \end{aligned}$$

Equation 2-12

ΔA records any change in the absorption spectrum as a function of time and wavelength. Thus, it reflects Ground State Bleaching (GSB, $\Delta A < 0$), Photo-Induced Absorption (PIA, $\Delta A > 0$), Stimulated Emission (SE, $\Delta A < 0$). GSB reflects the depletion of the ground state carriers to excited states. PIA refers to further excitation of excited carriers to higher energy levels. SE is the process that the incoming of a photon interacts

with an excited carrier and causes it to drop to a lower energy level by releasing another photon.

Conventionally, ΔA is scaled by the absorption of probe without pump, which is called differential absorption (DA):

$$DA = \frac{\Delta A}{A} = \frac{A_{pump} - A}{A}$$

Equation 2-13

The same definition can be generalized to ΔR and DR as well:

$$\begin{aligned} & \text{Reflection}(of\ probe\ with\ pump)(R_{pump}) \\ & - \text{Reflection}(of\ probe\ without\ pump)(R) \\ & = \Delta \text{Reflection}(\Delta R) \end{aligned}$$

Equation 2-14

$$DR = \frac{\Delta R}{R} = \frac{R_{pump} - R}{R}$$

Equation 2-15

When TA/TR are measured as a function of wavelength and time, it is called time resolved TA/TR spectroscopy (TRTRS). The TA/TR curve along wavelength provides information of different signatures (GSB, PIA, SE and so on) about the substance. Like finger printing, it gives the spectrum with signatures depending on materials. Different processes can also be extracted from the TA/TR curve along time, which can reveal the lifetimes of true physical processes upon the pump excitation. As a matter of fact, with selected pump and probe energies, it can give insights on different processes, such as hot carrier cooling, nonradiative exciton recombination, radiative recombination and so on. Usually, TRTRS is combined with other optical techniques like time resolved

photoluminescence, time resolved THz spectroscopy to distinguish different signatures or processes.

Chapter 3 Experimental Results

3.1 Zr

3.1.1 Overview

Fresh Zr is highly reactive and it will be immediately oxidized when exposed to ambient air. To access the bonding information on the interface between Zr and its oxide film, SHG anisotropy has been applied. It was found that strain introduced in the polishing process (if not well-controlled) could have an important effect on biasing SHG anisotropy, indicating a rough interface. Thus, a new sample preparing recipe was developed to achieve a smoother interface. ABM has been utilized for modeling the SHG anisotropy.

Besides the well-formed interface, to study the oxidation of Zr, SHG and AES have been used. With SHG, it was found that the initial oxidation of Zr obeys Langmuir kinetics with a time constant of 0.57 Langmuir. Moreover, the phase change of ZrO_2/Zr interface has a time constant of 2.93 Langmuir. With AES, the subsequent oxidation following an exponential decay with a time constant of 10.8 Langmuir was revealed. The combination of SHG and AES successfully shows the two-stage oxidation process on Zr surface which gives insights into the detailed oxidation process of Zr.

3.1.2 Experimental Methods

3.1.2.1 In ambient air

The sample (Figure 3-1) in the investigation was a one-side polished plate (surface roughness $<0.03 \mu\text{m}$) of polycrystalline Zr (~ 2 cm in diameter, ~ 1 mm in thickness) with

several crystalline grains in an orientation (0001) of accuracy $<1^\circ$. The sample was first cut into small pieces along grain boundaries. These small pieces have cross-sectional areas approximating 0.25 cm^2 in roughly shaped triangles or squares. One thing that needs to be paid attention is that even if the surface is very smooth, it does not indicate a well-structured interface. Since Zr is highly reactive to oxidizers in ambient air, the sample is naturally covered by a layer of hard, transparent Zr oxide¹⁰⁵. Consequentially, a fine polish on the surface, which is mostly the last step of a complete mechanical polishing process, may not be able to access the interface, rendering a smooth oxide surface instead of a smooth interface between oxide film and Zr.

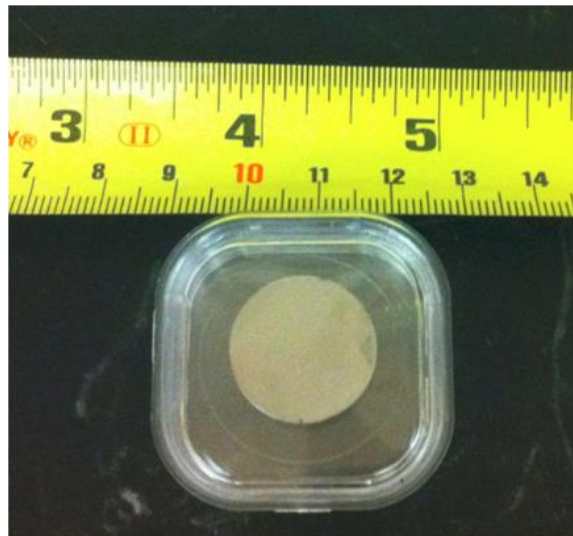


Figure 3-1 Picture of Zr (0001).

To eliminate possible confusion, the surface of Zr here is defined as the surface of fresh Zr when there is no oxide film, or the interface between Zr and its oxide film when oxide film presents.

Interface roughness and/or unknown strain are adverse effects while applying reflective optical methods. Thus, preparation of an atomically clean surface is crucial.

The goal of sample preparation is to achieve an optically smooth and a clean surface of single-crystal Zr. In ambient air, a clean surface here indicates that the surface of Zr maintains macroscopic crystalline structure even it's oxidized, i.e. oxidization changes only its microscopic structure, and its macroscopic symmetry won't be destroyed by other factors like polishing.

Accordingly, post processing in ambient air was applied. First, rough polish with 320, 400 and 600 grit SiC polishing wheels, step by step. Any finer sand paper than the aforementioned proved to be ineffective due to the hardness of the oxide layer on the surface. Second, fine polish 4 hours on a vibratory polisher using a 0.05 colloidal silica solution. A heavy weight was placed upon the polishing fixture to avoid leaving a residual film on the surface of sample. Third, acid etch by dipping into 37% nitric acid and 1.5% HF diluted with nanopure water. To etch the sample slowly and evenly, the etching solution with beaker was placed in a mixture of ice and water and the sample was sonicated in the etching solution for approximately 10 seconds. After acid etching, it was clear that the oxide had been removed in the acid solution because the new Zr surface became rougher and the new oxide surface appeared thinner observed by eye, and also revealed by SHG anisotropy. It is worth to mention that a diluter solution cannot penetrate into the relatively stable oxide film. To reduce the roughness on Zr surface, fine polishing again on a vibratory polisher was conducted. As a result, one relatively smooth interface with slight strain can be achieved, verified by SHG anisotropy below.

SHG anisotropy experiments were performed in reflection geometry using ultra-short laser pulses tuned at 800 nm with a repetition rate of 76 MHz (refer to Appendix A for detailed specifications of laser) and incident on the sample at 45 degrees (Figure 3-2).

Without otherwise stated, all the experimental conditions were in ambient air. The SHG anisotropy at 400 nm was collected as the sample was rotated along its azimuthal axis in ambient air. The beam was focused to a $\sim 40 \mu\text{m}$ spot on the sample with a power density less than 8 kW/cm^2 or a laser fluence less than $100 \mu\text{J/cm}^2$, which is below the damage threshold. Excitation and detection paths utilized wave-plates, polarizers and analyzers to measure the resulting SHG for $P_{\text{in}}/P_{\text{out}}$, $P_{\text{in}}/S_{\text{out}}$, $S_{\text{in}}/P_{\text{out}}$, and $S_{\text{in}}/S_{\text{out}}$ excitation and radiation polarization configuration as needed, where P means light polarization in the plane of incidence and S means polarization perpendicular to the plane of incidence. The PMT (P30CWAD5A, Electron Tubes Limited) was operating in photon-counting mode, having a uniform sensitive surface to make sure that SHG anisotropy was not biased by slightly change in the direction of SHG upon the rotation of the sample.

Reflective SHG set-up

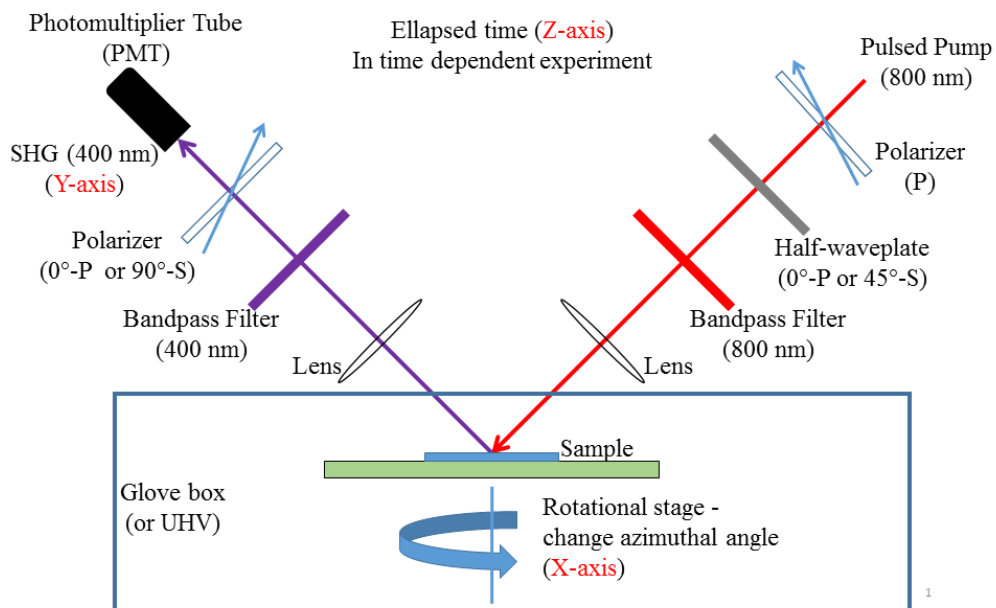


Figure 3-2 Diagram of SHG setup.

3.1.2.2 In UHV chamber

In UHV, a clean surface is classically defined to be an annealed surface at ambient temperature with a total surface contamination of less than a few percent of a monolayer.

Because Zr is highly interactive to gaseous molecules, further processing, was conducted in UHV to access the fresh Zr and to delay its oxidation process. Cleaning procedure specifically for Zr (0001) in the UHV involves heating to a high temperature requiring pressures ideally near 1×10^{-11} Torr at room temperature, argon ion sputtering, annealing, and in-situ element-specific analysis of the surface.

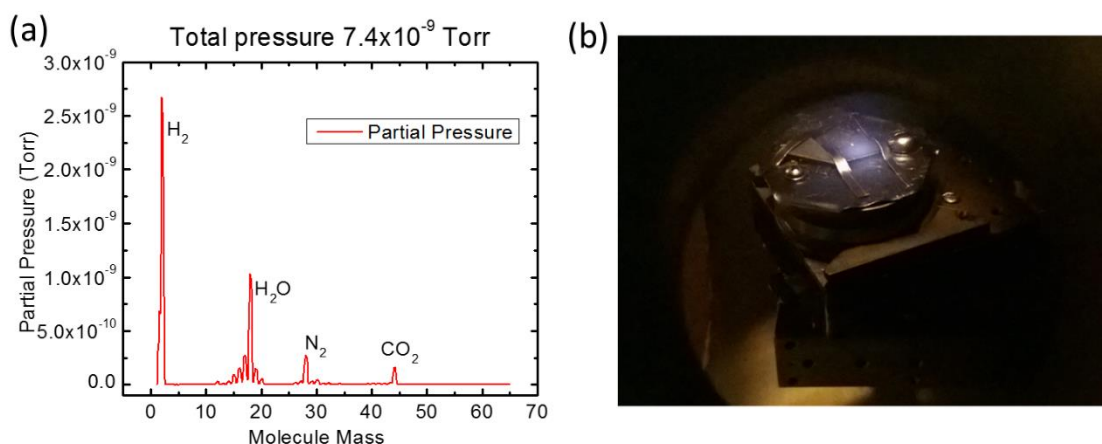


Figure 3-3 (a) Residual Gas Analysis inside UHV chamber. (b) Zr(0001) under sputtering.

The UHV chamber was step-pumped (Rough, Turbo, Ion, TSP pump, plus baking) to a base pressure about 1×10^{-9} Torr, which took about 5 days. Once the pressure of near 1×10^{-9} Torr was reached, it became difficult to detect leaks and contamination in the chamber. Figure 3-3 (a) shows a typical residual gas analysis of the ambient environment inside UHV chamber before baking at 7.4×10^{-9} Torr. We researched exhaustively to find an ideal “baking” recipe to achieve the lowest pressure possible for our UHV chamber.

However, there is a very small room for error when trying to reach the pressures ideally needed for a clean Zr surface (i.e. 1×10^{-11} Torr), but we were still able to achieve a clean surface for a small period of time (as indicated later). Then the chamber was back-filled with ultra-high purity Argon (purity > 99.999%) to 5×10^{-5} Torr. The emission current was set to 25 mA and the beam voltage was at 3 kV during the period of sputtering for about 4 hours (Figure 3-3 b), followed by annealing. Annealing insures the reproducibility of a nearly defect-free crystallinity surface. Sputtering and annealing were repeated several (4-7) times to ensure complete oxide removal.

AES is the surface characterization method we utilized since this method has detection limits of about one percent of a monolayer for individual elemental contamination of the surface. The quality of our oxide removal is shown by AES spectrum peaks representing relative ratios of Zr to amounts of carbon and oxygen contaminations on the surface. Peak to peak magnitude of an AES peak in a differentiated spectrum is directly related to the surface concentration of the element which produces Auger electrons. Figure 3-4 shows a typical AES results before and after 140 min sputtering. It is clear that the contaminants containing C atoms can be removed by Ar^+ sputtering and Zr atoms show up as accessing to fresh Zr. As a side note, the arise of the O atom peak is due to the insufficient sputtering time (140 min) here, in which stage, most of the contaminants are removed or “cleaned” by Ar ions. Actually, after several rounds of sputtering (~4 hours), O atom peak will almost disappear on AES.

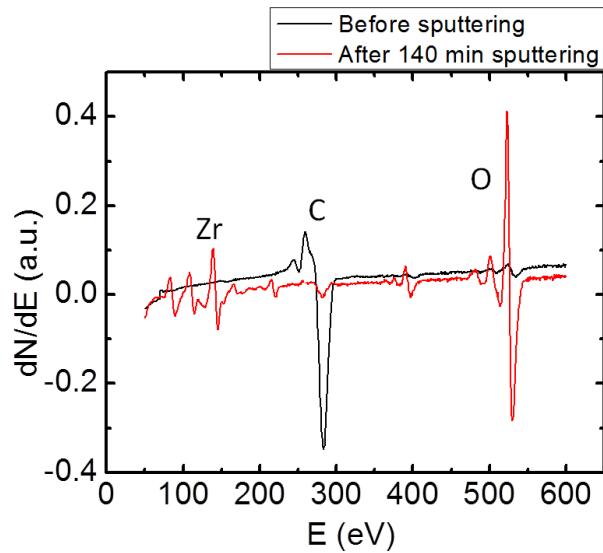


Figure 3-4 AES before (black) and after (red) sputtering.

The SHG experiment was conducted by passing the 800 nm light through the window on the UHV chamber onto the sample, with the reflected SHG collected through another window by the PMT (Figure 3-5). The set-up is very similar to the diagram in Figure 3-2, however, due to the different experimental conditions (limit in geometry, noise level), there are mainly two differences. First, the sample was sitting in the center of the UHV chamber, which was at least 20 cm from the nearest accessible window, thus a 30 cm focus lens was used, so the beam size on the sample would be $\sim 150 \mu\text{m}$ in diameter (see Eq. B-5 in Appendix B); the incidence angle was also changed to 60° limited also by the geometry. Second, because of the increased noise, the PMT (H10721, HAMAMATSU) operating in current mode was used with lock-in amplifier (SR810, Stanford Research Systems) in a chopping frequency of 400 Hz to eliminate the background noise. The azimuthal angle of the sample can be rotated in a range of $\sim 180^\circ$, where the maximum SHG was found at a certain angle θ_0 before the processing in UHV. The azimuthal angle θ_0 was fixed without otherwise stated. Excitation and detection paths

utilized wave-plates, polarizers and analyzers to measure the resulting SHG for P_{in}/P_{out} excitation and radiation polarization, where P means light polarization in the plane of incidence.

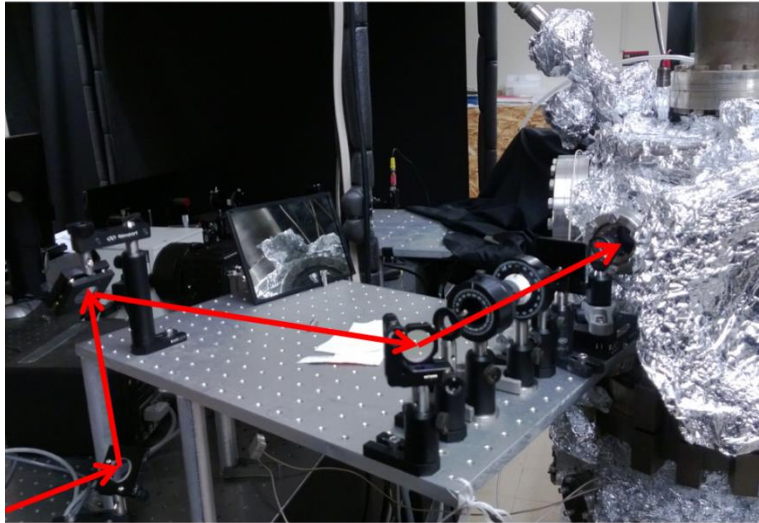


Figure 3-5 Picture of SHG experiment combined with UHV chamber: the arrowed lines indicate the path of 800 nm laser into the UHV chamber.

3.1.3 Experimental Results

3.1.3.1 SHG anisotropy from the interface of Zr/ZrO_2

Zr has hexagonal close-packed (HCP) structure, and the surface of (0001) has a 3-fold structure. It^{106, 107} was suggested theoretically that the initial adsorption of oxygen atoms will favor the surface face-centered cubic (SFCC) sites; as the adsorption of oxygen increases, oxygen atoms will start to occupy octahedral sites in the alternative layers such as Octa (2,3), Octa (4,5) and Octa (6,7). We can reasonably extend it to the

interface of well-formed Zr-ZrO₂ interface that oxygen atoms occupy the octahedral sites on the interface.

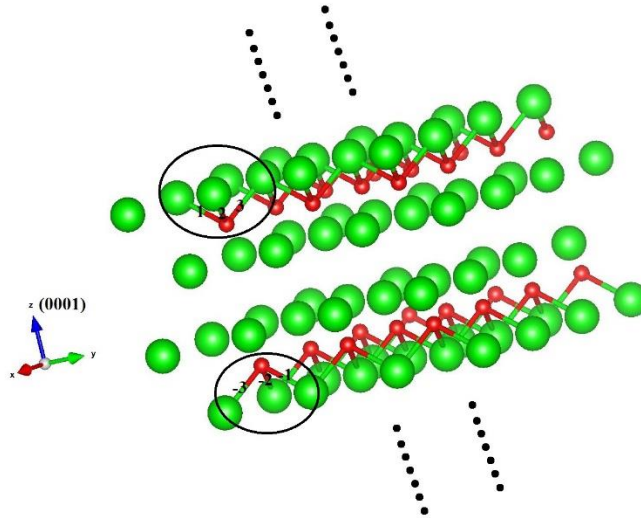


Figure 3-6 Oxygen atoms are in octahedral sites in alternative layers on the interface of Zr/ZrO₂.

As shown in Figure 3-6, due to the symmetry, there are only 6 independent bonds (numbered 1, 2, 3, and -1, -2, -3). Figure 3-7 shows the SHG anisotropies in P_{in} - P_{out} and P_{in} - S_{out} geometries simulated with ABM. The SHG anisotropy shows a 3-fold symmetry and a 6-fold symmetry, for P_{in} - P_{out} and P_{in} - S_{out} geometries, respectively. MPM will give the similar pattern based on the symmetry of the interface. For simplicity, here we excluded other effects, such as the EFISH. In real experimental measurements, the interface conditions could be much more complicated by the emergence of other factors, like surface roughness, strains, locally trapped charges and so on.

SHG anisotropy from a perfect interface

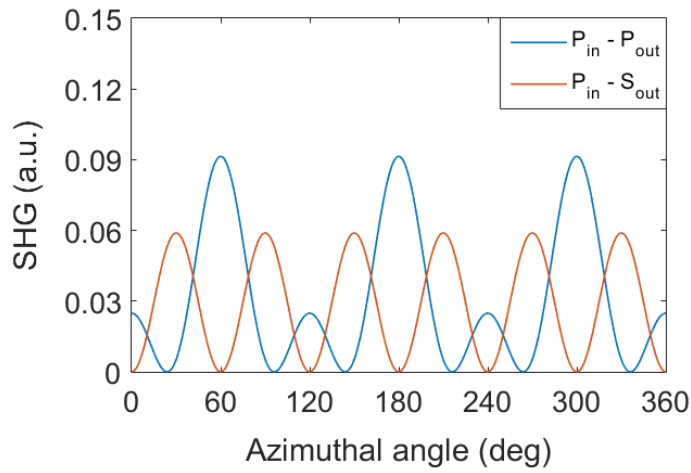


Figure 3-7 ABM simulation of SHG from a perfect interface between Zr and its oxide film.

To confirm the quality of the interface, SHG anisotropy (Figure 3-8) was measured in $P_{in} - P_{out}$ geometry without any further processing on the as-received Zr (0001). There was no 3-fold pattern as predicted in Figure 3-7. To confirm our assumption that there is no SHG from the interface of oxide and air, we did SHG anisotropy on ZrO_2 single crystal and there was no SHG signal at all. Thus we can safely attribute SHG signal from the interface between Zr and its oxide.

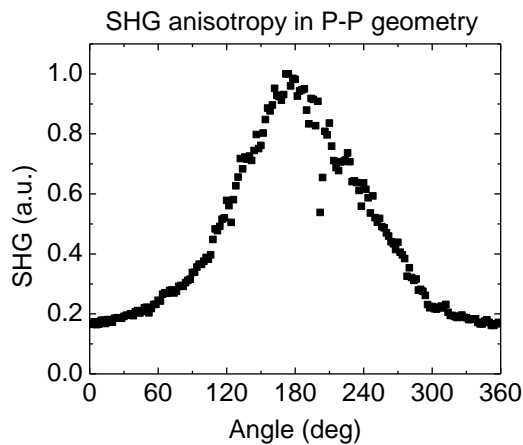


Figure 3-8 SHG anisotropy of as-received Zr (0001) single crystal.

While it's well studied that strain could have a significant impact on the SHG anisotropy¹⁰⁸, we suspected that the interface experienced strong strain effect. To confirm our suspect, we did SHG anisotropy on the as-grown Ti film, which has a (0001) direction as well. Ti also has a thin film of native oxide, and has very similar structure and properties as Zr. Generally, in Figure 3-9, SHG anisotropy on Ti shows the 3-fold symmetry. Hence, we can tentatively conclude that the erratic SHG anisotropy on Zr in Figure 3-8 is due to the effect of strain.

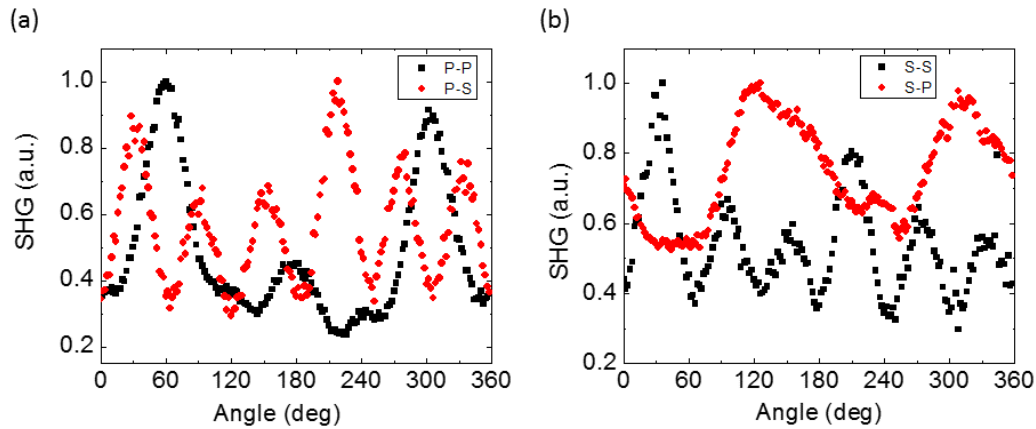


Figure 3-9 SHG anisotropy on as grown Ti. (a) P-P (black) and P-S (red) geometries. (b) S-S (black) and S-P (red) geometries.

To relieve the strain on the interface, acid etching was conducted on the Zr sample as described in the experimental methods. After the etching, SHG anisotropy was measured again, shown in Figure 3-10 (black dots). The appearance of 3-fold structure indicates that strain had been removed mostly. SHG anisotropy can be fitted by ABM well (red curves in Figure 3-10) except some outliers. The greater fluctuation in the data was concluded into that the aggressive solution induced a rougher interface. Therefore, we fine polished the Zr sample again, and the SHG anisotropy results are in Figure 3-11.

While fluctuation in SHG signal was reduced, however, the peaks are irregular and ABM is not applicable. We suspect that strain was again introduced in the polishing. We tried slightly diluter chemical solution but the oxide film was not etched even in a much longer time. The carefully controlled polishing won't improve SHG anisotropy, either.

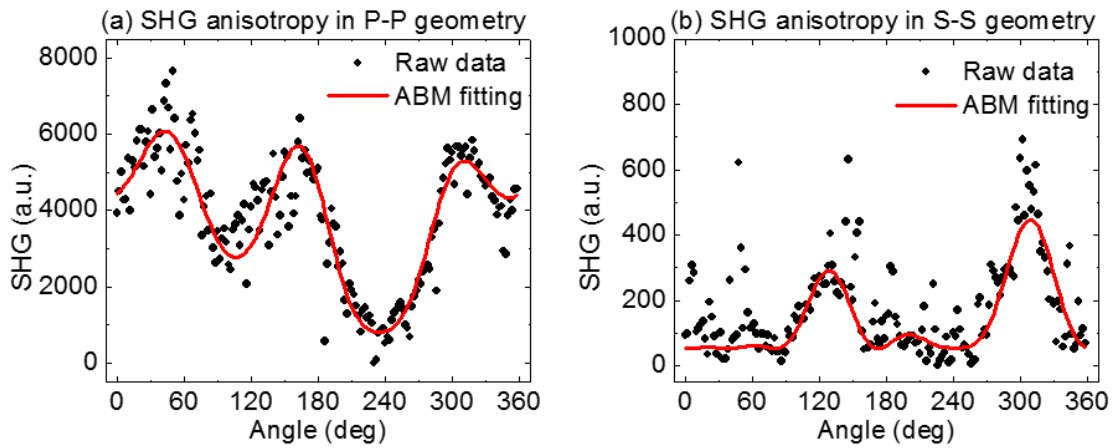


Figure 3-10 SHG anisotropy after chemical etching.

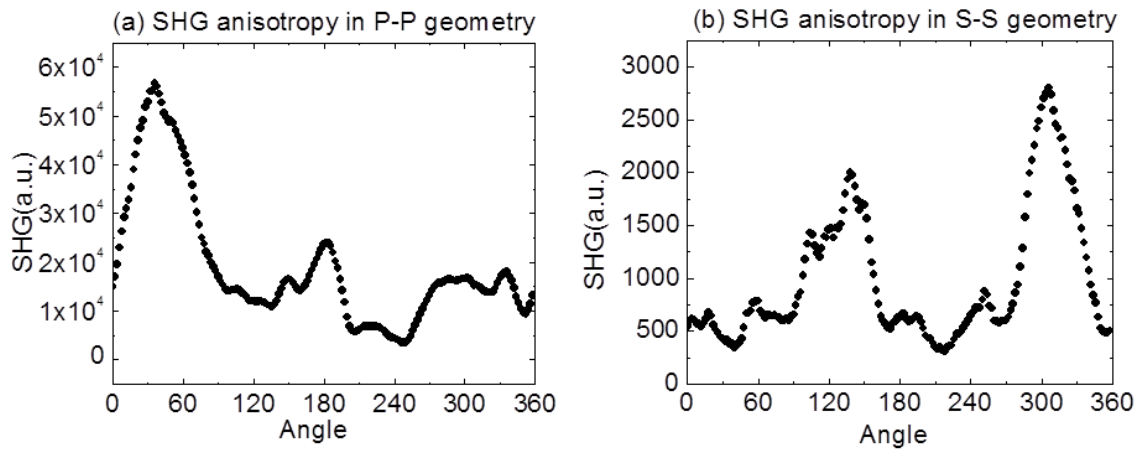


Figure 3-11 SHG anisotropy after fine polishing. (a) P-P geometry. (b) S-S geometry.

Our studies show that chemical etching can remove polishing-induced strain on the interface in the sack of a rougher surface. And the polishing can get smoother interface in the sack of introducing strain. Future works should be done to achieve a better balance between chemical etching and polishing in ambient air, which requires extremely delicate controls if possible.

3.1.3.2 Time dependent AES and SHG results during the oxidation of fresh Zr

As Zr will be oxidized immediately if exposed to ambient air, to extend the oxidation time of fresh Zr for study, we introduced Zr into UHV chamber and removed the oxide film with Ar ion sputtering and recovered the crystal with annealing. After the removal of oxide film, fresh Zr was sitting in the ambient environment with a vacuum of 1×10^{-9} Torr, as the residual gaseous components analyzed in Figure 3-3 (a) before baking.

AES gives an overview on the amounts of different atoms in its sensitive region near the surface of the sample. As we can see in the AES figure (Figure 3-12), after the exposure of processed fresh Zr, Zr peak decreases as O peak and C peak increase. O atom is from oxidation since Zr is highly reactive to oxidizers in the ambient environment, such as H₂O and CO₂ (Figure 3-3 a). C atom is from the contamination or the adsorption of CO₂.

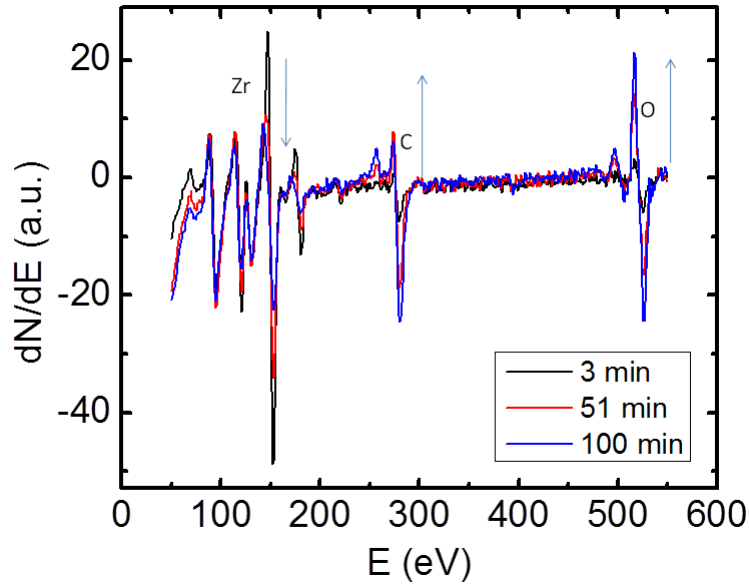


Figure 3-12 AES upon oxidation of fresh Zr in ambient environment of UHV.

A detailed trend can be found in Figure 3-13 on selected signature peaks.

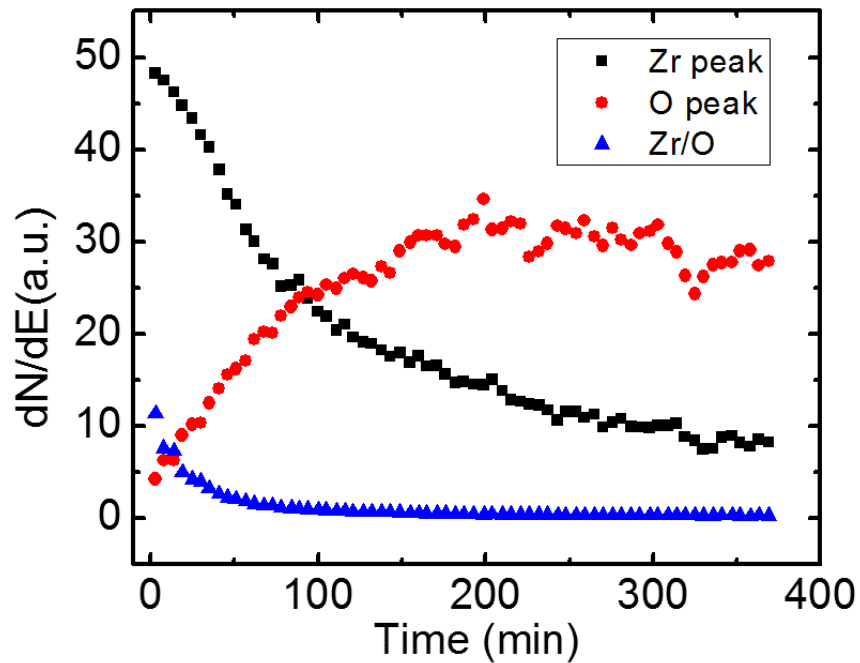


Figure 3-13 Change of Zr and O peaks in AES upon exposure of fresh Zr in ambient environment of UHV.

The thickness of Zr oxide can be derived from the ratio of Zr/O peaks in the AES.

We apply two assumptions:

1. The oxide is stable after 360 min in UHV $\sim 1.5 \text{ nm}^{109}$ (Figure 3-14)
2. AES sensitive range $\sim 2 \text{ nm}^{110}$.

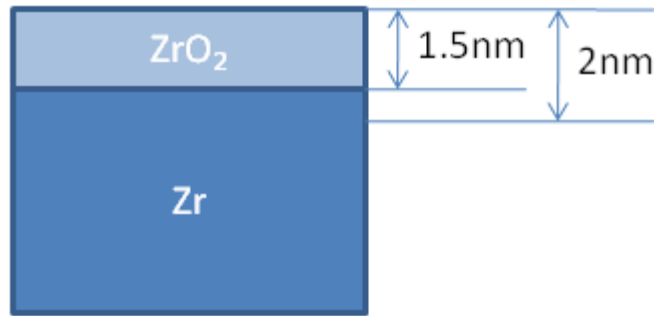


Figure 3-14 Diagram of Zr oxide on the surface of Zr

Because AES sensitivities to different atoms are different. Here we use N_{Zr} , N_O , S_{Zr} and S_O to denote the number of Zr atoms, the number of O atoms, the sensitivity to Zr and the sensitivity to O, respectively, in its sensitive region. The ratio between Zr peak and O peak is equal to:

$$\frac{Auger(Zr)}{Auger(O)} = \frac{N_{Zr}}{N_O} * \frac{S_{Zr}}{S_O}$$

Equation 3-1

When stable, in Figure 3-13 after 360 min:

$$\frac{Auger(Zr)}{Auger(O)} = 0.3$$

Equation 3-2

During the oxidation of Zr, O atom will penetrate into the Zr oxide film and form oxide and/or suboxide on the interface of Zr and Zr oxide. Since the thickness of Zr suboxide is negligible, a reasonable approximation is that Zr bi-oxide thickness grows on the surface of Zr. If T_{ZrO_2} denotes the thickness of Zr bi-oxide, assuming that Zr atom and O atom occupy similar space, the ratio of Zr atoms and O atoms detected by AES is:

$$\frac{N_{Zr}}{N_O} = \frac{T_{ZrO_2} * 1/3 + (2 - T_{ZrO_2}) * 1}{T_{ZrO_2} * 2/3}$$

Equation 3-3

When stale after 360 min, according to the Zr oxide diagram (Figure 3-14), we can get:

$$\frac{N_{Zr}}{N_O} = \frac{1.5 \text{ nm} * 1/3 + (2 - 1.5 \text{ nm}) * 1}{1.5 \text{ nm} * 2/3} = 1$$

Equation 3-4

Combine Equation 3-1, Equation 3-2 and Equation 3-4, and we get:

$$\frac{S_{Zr}}{S_O} = \frac{Auger(Zr)/Auger(O)}{N_{Zr}/N_O} = 0.3$$

Equation 3-5

Thus we get the ratio between the sensitivities of Zr and O.

With Equation 3-1, Equation 3-2, Equation 3-3 and Equation 3-5, the thickness of Zr oxide can be derived:

$$T_{ZrO_2} = \frac{3}{1 + \frac{N_{Zr}}{N_O}} = \frac{3}{1 + \frac{Auger(Zr)/Auger(O)}{S_{Zr}/S_O}} = \frac{3}{1 + \frac{10}{3} * \frac{Auger(Zr)}{Auger(O)}}$$

Equation 3-6

Now the relationship between AES and ZrO₂ thickness has been established. Figure 3-15 is the plot of the ZrO₂ thickness growth versus the exposure in Langmuir¹, and the single exponential function $y = A_0 + A_1 * e^{-x/\tau}$ fits well with $A_0 = 1.78 \pm 0.03$ nm, $A_1 = -1.81 \pm 0.03$ nm and $\tau = 10.8 \pm 0.5$ L.

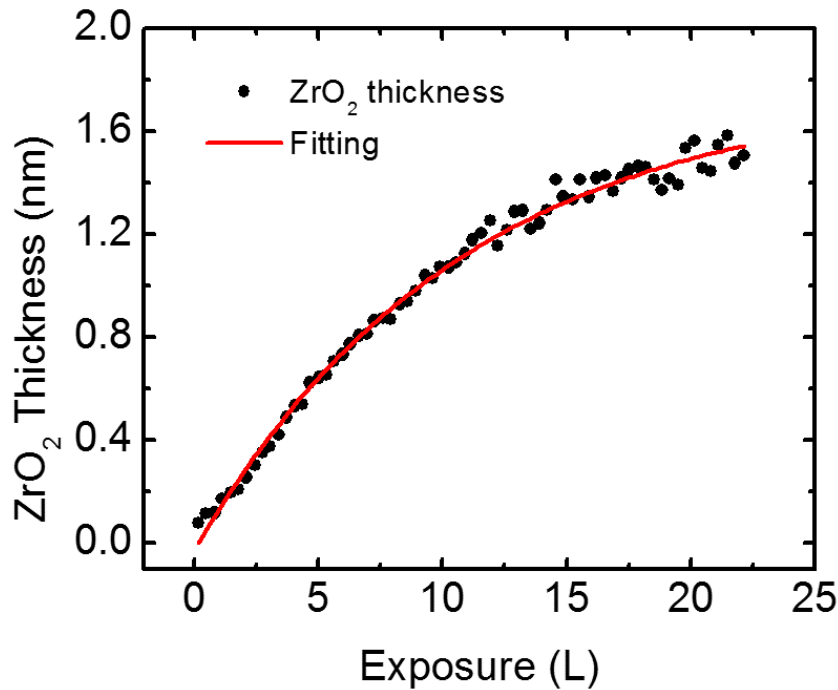


Figure 3-15 Change of ZrO₂ thickness along with the exposure in Langmuir (black dots). The fitting (red curve) using a single exponential function $y = A_0 + A_1 * e^{-x/\tau}$ gives $A_0 = 1.78 \pm 0.03$ nm, $A_1 = -1.81 \pm 0.03$ nm and $\tau = 10.8 \pm 0.5$ L.

AES can provide the atomic information of its sensitive region, whereas SHG has the power of extracting the bonding information between atoms¹⁰⁸. We introduced pulsed 800 nm lasing into the UHV chamber, directed it on the surface of Zr plate and collected the reflected beam through a 400 nm bandpass filter into the PMT. Figure 3-16 shows the

¹ 1 Langmuir = 1×10^{-6} Torr·s

collected SHG upon the exposure of fresh Zr with an exponential fitting. And the two exponential function $y = A_0 + A_1 * e^{-x/\tau_1} + A_2 * e^{-x/\tau_2}$ fits well with $A_0 = 1.079 \pm 0.004$, $A_1 = 22.88 \pm 0.08$, $\tau_1 = 0.360 \pm 0.002$ L, $A_2 = 4.21 \pm 0.05$ and $\tau_2 = 2.52 \pm 0.03$ L (adjusted $R^2 = 0.99773$), implying a two-stage process in the oxidation of fresh Zr. The general trend shows that SHG decays fast at the beginning and starts to decay slowly later. To explain the underlying physical meanings, a detailed discussion is demonstrated below.

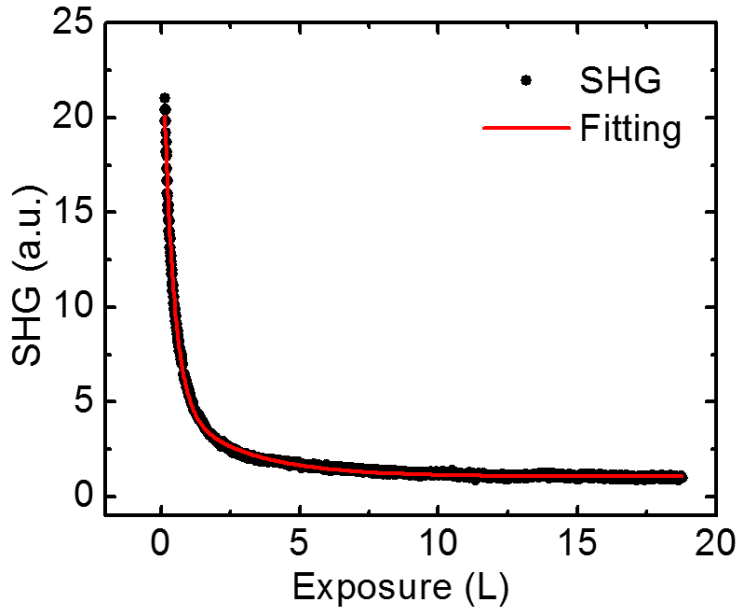


Figure 3-16 Change of SHG from Zr surface along with the exposure in Langmuir (black) with the fitting (red curve). The fitting (red curve) using a two exponential function $y = A_0 + A_1 * e^{-x/\tau_1} + A_2 * e^{-x/\tau_2}$ gives $A_0 = 1.079 \pm 0.004$, $A_1 = 22.88 \pm 0.08$, $\tau_1 = 0.360 \pm 0.002$ L, $A_2 = 4.21 \pm 0.05$ and $\tau_2 = 2.52 \pm 0.03$ L (adjusted $R^2 = 0.99773$).

Zr and crystalline or poly-crystalline Zr oxide have inversion symmetry, thus, SHG can only be generated at the surface of Zr or the interface between Zr and Zr oxide if oxidized. In other words, SHG is only sensitive to the surface of Zr. As a metal, electrons

are free on the fresh Zr surface. Whereas the electrons will be confined in the valent bondings between Zr atoms and O atoms once oxide forms on the interface. Thus, fresh Zr surface will have a much higher SHG intensity compared to oxidized Zr surface because the surface nonlinearity is mostly dominated by free electrons¹¹¹. In the exposure of Zr surface to the ambient environment in UHV, the density of free electrons decreases as molecules are adsorbed on Zr surface, rendering to a decrease in SHG, which is shown in Figure 3-16 as well. To establish the relationship between SHG and the coverage of oxide at the beginning stage, we tentatively assume the ratio of the 2nd order nonlinear coefficients from fresh Zr surface versus Zr/ZrO₂ interface is 1:R (R<<1).

$$\chi_{Zr}^{(2)} : \chi_{ZrO_2/Zr}^{(2)} = 1 : R \quad (R \ll 1)$$

Equation 3-7

The initial adsorption of molecules can be described by Langmuir kinetics:

$$\tau * \dot{\theta} = 1 - \theta \Rightarrow \theta = 1 - e^{-t/\tau}$$

Equation 3-8

θ is the surface adsorption coverage, τ is the adsorption time constant (the inverse of adsorption rate), and t is the exposure duration in Langmuir. Set $\chi_0^{(2)}$ as the 2nd order nonlinear coefficient when the oxidation is stabilized. We can get $\chi^{(2)}$ during the oxidation is:

$$\chi^{(2)} = \theta * R + (1 - \theta) * 1$$

Equation 3-9

Thus, assuming I_0 as the SHG intensity when the surface is stable, then, during oxidation, SHG intensity I is equal to:

$$I = I_0 * |1 - \theta * (1 - R)|^2$$

Equation 3-10

Combine Equation 3-8 and Equation 3-10:

$$I = I_0 * |1 - (1 - e^{-t/\tau}) * (1 - R)|^2$$

Equation 3-11

Besides the Langmuir kinetics, we need to include one more process, as observed in the continuous decrease of SHG within our exposure window after several Langmuirs, which can be reasonably concluded into the further change on the interface after the formation of the first several monolayers. We tentatively attribute an exponential term in addition to Equation 3-11, thus we have:

$$I = I_0 * |1 - (1 - e^{-t/\tau_1}) * (1 - R)|^2 + A_0 * e^{-t/\tau_2}$$

Equation 3-12

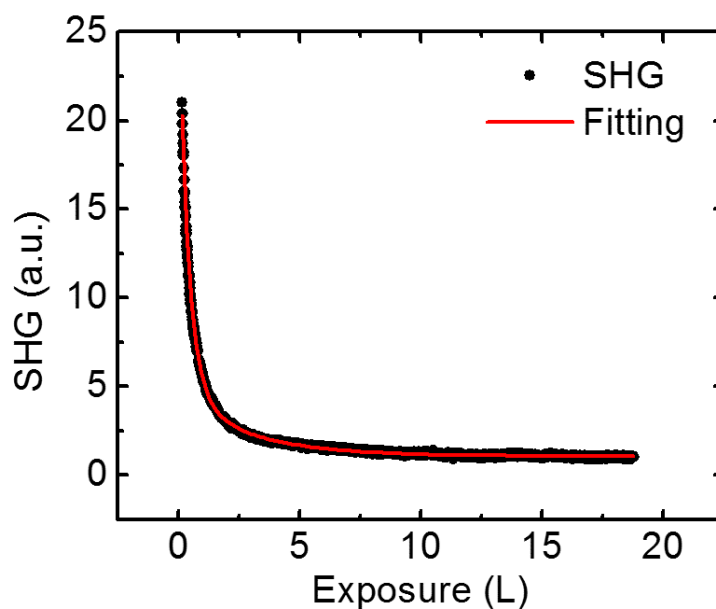


Figure 3-17 Change of SHG from Zr surface along with the exposure in Langmuir (black) with the fitting (red curve). The fitting (red curve) using Equation 3-12 gives $I_0 = 25.73$, $R = 0.20$, $\tau_1 = 0.57$, $A_2 = 3.42$, $\tau_2 = 2.93$ (adjust $R^2 = 0.99847$)

The fitting using Equation 3-12 gives: $I_0 = 25.73$, $R = 0.20$, $\tau_1 = 0.57$, $A_2 = 3.42$, $\tau_2 = 2.93$ (adjust $R^2 = 0.99847$). The time constant of the Langmuir kinetics is in the same order of 1 Langmuir, showing that any molecule that hits the surface of Zr will be trapped, an indication of Zr's high reactivity. A direct compare between Figure 3-16 and Figure 3-17 shows that Equation 3-12 fits the experimental data slightly better (adjust $R^2 = 0.99847 > 0.99773$). While the estimates in the time constants yield similar values, in future works, we can adopt the two exponential function fitting for convenience.

In Figure 3-18, when the x-axis (exposure time) is in log-scale, a two-stage process for both SHG and ZrO_2 growth is clear, while the transition point is right around 1 Langmuir, when Zr is covered by one monolayer of adsorbed gas molecules on the surface.

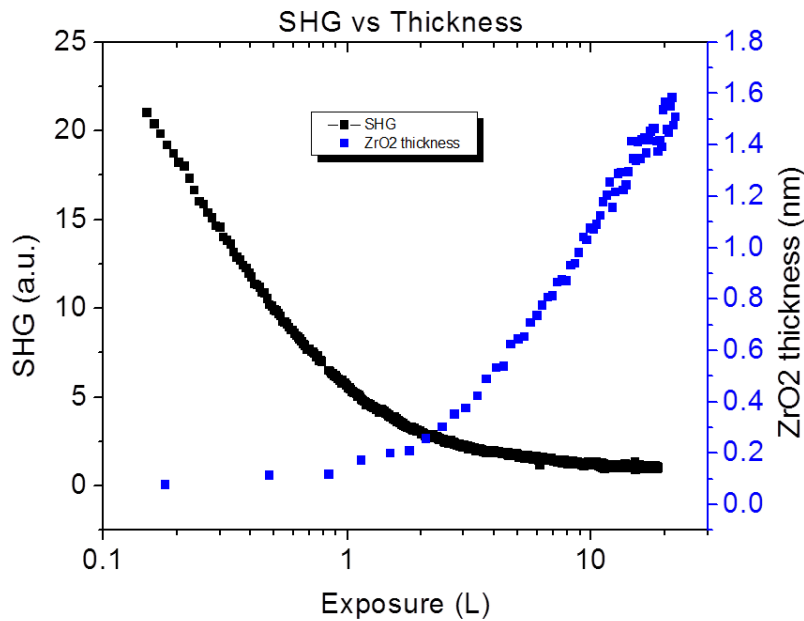


Figure 3-18 Change of ZrO₂ thickness (black squares) and SHG (blue squares) along with the exposure in Langmuir (x-axis in log scale).

3.1.4 Conclusions

A recipe is developed for surface processing on Zr. SHG anisotropy has been successfully applied to access the interface between Zr and its oxide film and is very sensitive to the interface conditions, such as the strain and roughness. ABM could be used as the model to extract the bonding information.

Under the ambient environment in UHV, SHG and AES have successfully revealed the two-stage oxidation process on Zr. With SHG, it was found that the initial oxidation of Zr obeys Langmuir kinetics with a time constant of 0.57 Langmuir. In addition, the phase change of ZrO₂/Zr interface has a time constant of 2.93 Langmuir. With AES, the subsequent oxidation follows an exponential decay with a time scale of 10.8 Langmuir.

The two-stage oxidation process on Zr surface gives insights into the detailed oxidation process of Zr.

3.2 Bi₂Se₃²

3.2.1 Overview

The time evolution of electrostatic fields near a Bi₂Se₃ surface after a mechanical cleave was observed using SHG. By comparing samples with different bulk doping levels and samples cleaved in different gas environments, these observations indicate multiple contributions to electric field evolution. These include the intrinsic process of Se vacancy diffusion as well as extrinsic processes due to both reactive and nonreactive surface adsorbates.

Here, new experiments that monitor the very long time evolution of SHG from Bi₂Se₃ surfaces cleaved under different conditions are reported. These experiments allow deconvolution of the impact of multiple surface processes, both intrinsic and extrinsic. We resolve intrinsic SHG changes due to the accumulation of electrons and Se vacancies near the surface. In addition, extrinsic electrostatic impacts of surface adsorbates are observed by cleaving in different gas environments. Finally gradual and extensive chemical modification of the surface due to long-time exposure to ambient air is observed.

² This work is in part published in the reference 112. C. Xu, A. Hewitt, J. Wang, T. Guan, J. Boltersdorf, P. A. Maggard, D. B. Dougherty and K. Gundogdu, *Journal of Applied Physics* **116** (4), - (2014).

3.2.2 Experimental Methods

Single crystal samples were grown from the binary melt by sealing Bi shot (Aldrich, 99.999%; 1-5 mm) and an excess of Se pellets (Aldrich, 99.999%; < 5 mm) in two different Bi:Se ratios of 0.62 and 0.54 in vacuum-sealed fused-silica ampoules. Details of growth and characterization can be found as described previously.¹¹³ SHG experiments were performed in reflection geometry using ultra-short laser pulses tuned at 800 nm with a repetition rate of 250 kHz and incident on the sample at 45 degrees. The beam was focused to a ~40 μm spot with a power density of 0.06 kW/cm^2 , which is below the damage threshold. Detailed laser specifications can be found in Appendix A and the diagram of SHG set-up is similar to that in Figure 3-2. SHG Anisotropy at 400 nm was collected as the sample was rotated along its azimuthal axis. Excitation and detection paths utilized wave-plates, polarizers and analyzers to measure the resulting SHG for $P_{\text{in}}/P_{\text{out}}$, $P_{\text{in}}/S_{\text{out}}$, $S_{\text{in}}/P_{\text{out}}$, and $S_{\text{in}}/S_{\text{out}}$ excitation and radiation polarization configurations, where P means light polarization in the plane of incidence and S means polarization perpendicular to the plane of incidence. To control the gaseous environment, the sample was sealed in a glove box, which was purged with desired gas.

3.2.3 Ambient Air Cleave

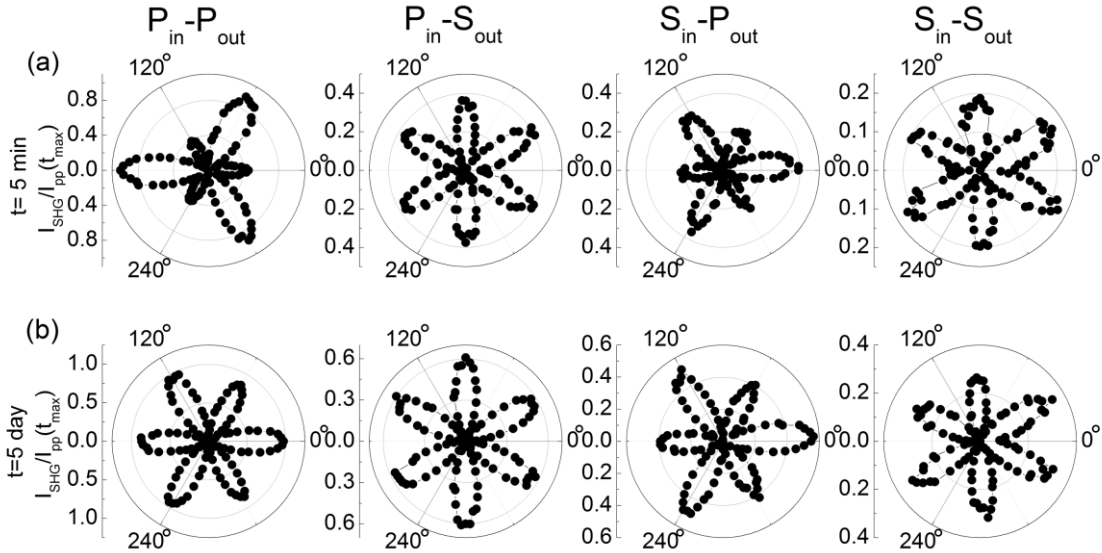


Figure 3-19 Normalized SHG Anisotropy from the Bi_2Se_3 (111) surface as a function of azimuthal angle φ . Measurements taken (a) 5 min and (b) 5 day after cleavage in ambient air. <1> $P_{\text{in}}-P_{\text{out}}$, <2> $P_{\text{in}}-S_{\text{out}}$, <3> $S_{\text{in}}-P_{\text{out}}$, <4> $S_{\text{in}}-S_{\text{out}}$ indicate different incident and outgoing photon geometries.

Figure 3-19 shows the SHG response of (111) oriented Bi_2Se_3 (Bi:Se=0.62) surface after cleaving mechanically in air with scotch tape. Panels (a) and (b) display the experimental results measured in ambient air conditions 5 minutes and 5 days after cleaving the surface, respectively. The 3-fold rotational symmetry of the surface results in this flower pattern with 3 major and 3 minor peaks. The evolution of the anisotropy of the SHG response after 5 days is evident in Figure 3-19 (b) in which the relative intensity of the major and minor peaks is reversed compared to the early time pattern in Figure 3-19 (a).

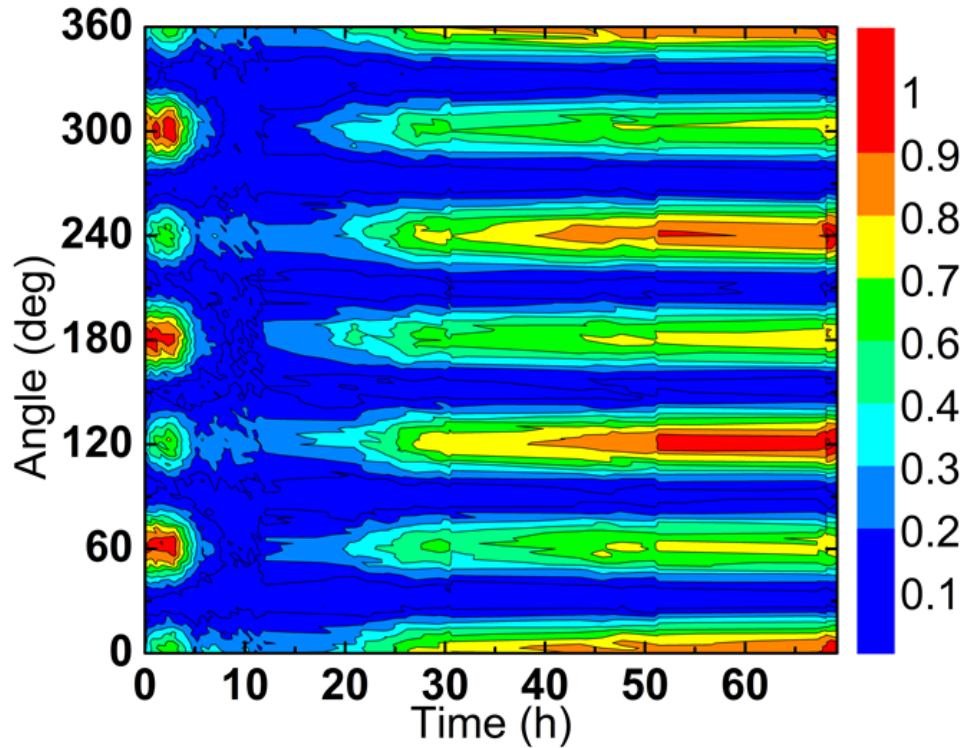


Figure 3-20 Time dependent SHG anisotropy after cleavage in ambient air for P_{in} - P_{out} geometry.

Figure 3-20 displays the complete time evolution of the SHG response on Bi_2Se_3 ($Bi:Se=0.62$) during the 69 hours after a mechanical cleavage in ambient air. In Figure 3-20, the SHG evolution for all azimuthal angles is shown for only p-polarized excitation and emission (P_{in} - P_{out}), whereas in Figure 3-21, only the minor and major peak evolutions are shown for all different input and output polarization combinations. The results exhibit a very complex dynamic response. For the first ~ 2 hours, there is a rise or plateau in the SHG for both major and minor peaks similar to the reports of Hsieh and co-workers for related samples.^{34, 35} After this initial rise, the SHG response decays during the next 10 hours. At the end of this decay, the anisotropy of the response exhibits a remarkable phase shift that changes the relative intensity of the major and minor peaks. Subsequently, all the peaks rise monotonically for the next 57 hours. The 3-fold

rotational anisotropy with reversed phase prevails with less difference between the major and minor peaks. We note that the four different polarization configurations in Figure 3-21 all follow the same trend. Therefore, in the following part, we will mainly focus on p-polarized excitation/emission configuration for our analysis.

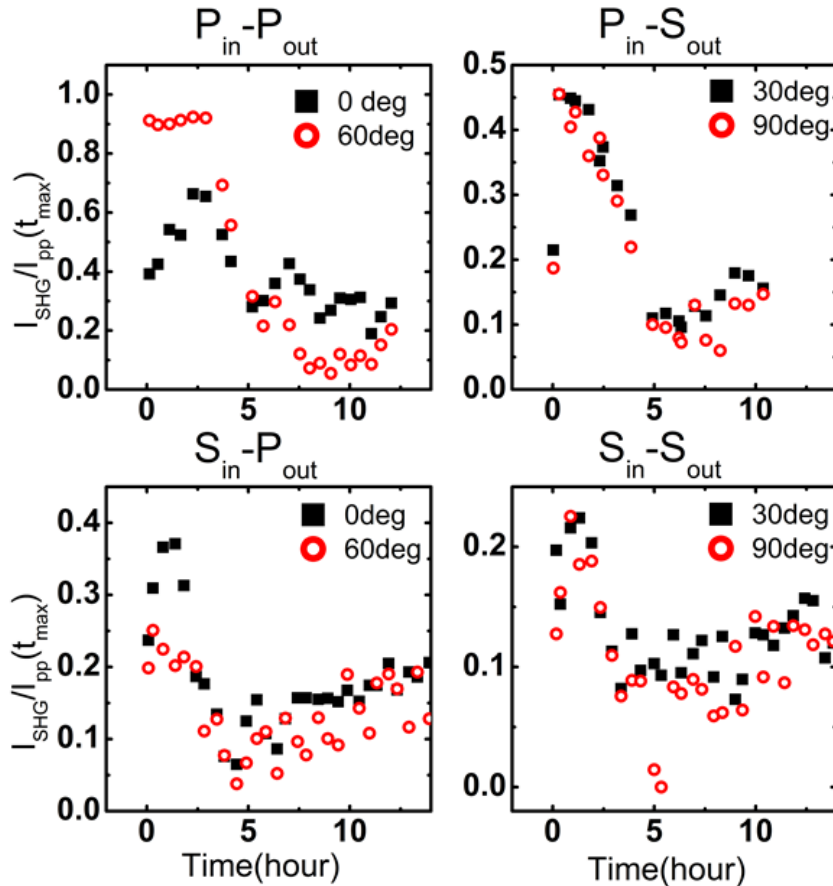


Figure 3-21 Evolution of SHG signal at high symmetric angles for different photon geometries.

The SHG evolution in Figure 3-19, Figure 3-20 and Figure 3-21 is substantially more complex compared to previous early-time measurements reported by Hsieh et al. that showed only a monotonic change in SHG intensity over ~ 100 minutes after cleaving in air.^{34, 35} We thus infer that there are multiple processes that contribute to the evolution of SHG in our samples. In order to isolate the contributions of various processes to the

SHG, we performed experiments that vary first the bulk carrier concentration and then ambient gas environment.

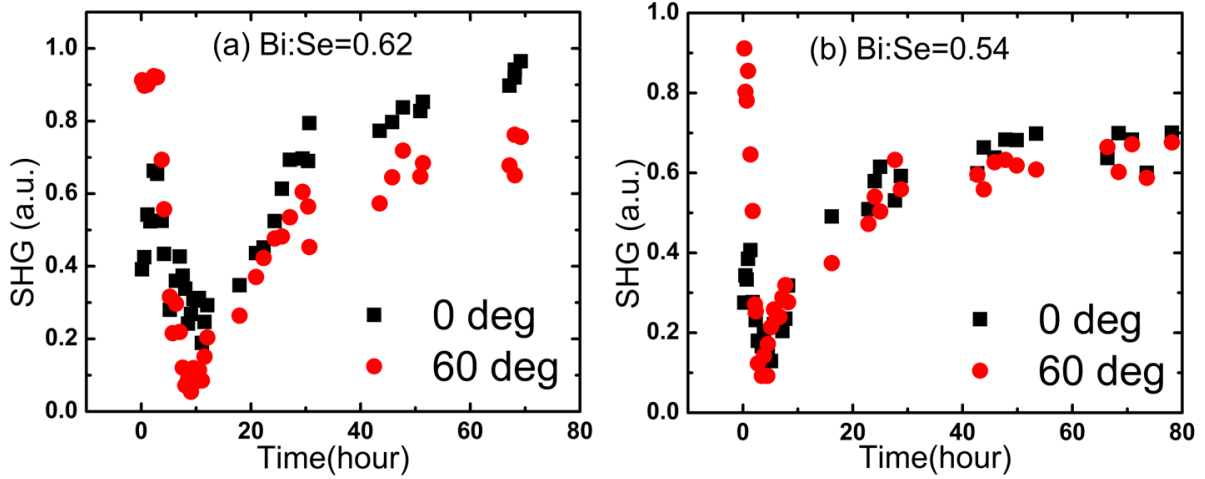


Figure 3-22 Time dependent SHG at 0° and 60° for different Bi_2Se_3 samples. (a) $\text{Bi}:\text{Se} = 0.62$ ($\sim 6 \times 10^{18} \text{ cm}^{-3}$); (b) $\text{Bi}:\text{Se} = 0.54$ ($\sim 5 \times 10^{17} \text{ cm}^{-3}$) after cleavage in ambient air in $P_{\text{in}}\text{-}P_{\text{out}}$ photon geometries.

First we focused on the intrinsic effect of bulk carrier concentration in the Bi_2Se_3 samples due to Se vacancies. Figure 3-22 (a) and (b) show the SHG evolution in ambient air for two samples grown with different melt compositions of Bi and Se that are known to result in an order of magnitude difference in carrier density. The melt composition of 0.62 is expected to give a carrier density of $\sim 6 \times 10^{18} \text{ cm}^{-3}$ and the composition of 0.54 is expected to give $\sim 5 \times 10^{17} \text{ cm}^{-3}$.³⁰ While the qualitative evolution is the same for both samples, there is a difference in the time scale of the early evolution. The early SHG rise and decay occurs within the first 10 hours in the high carrier concentration sample, whereas it takes about 4 hours in the low concentration material. However, the slow rise at very long time takes place over a similar time period for the different samples. After about 30 hours, SHG for the high concentration sample increased to its saturation level, whereas it took about 28 hours for the low concentration sample. This dependence on

carrier concentration will be discussed in more details below. Generally, it shows an important impact of electrostatic band bending near the surface in line with the general picture of SHG evolution in Bi_2Se_3 developed in previous work.^{34, 35}

3.2.4 Cleaves in Controlled Gas Environments

Given that ambient air is a mixture of O_2 , H_2O , N_2 , and other gases, interactions with several adsorbate molecules could modify the surface and may potentially lead to chemical and/or structural changes. In order to study the effect of surface adsorption, we performed controlled experiments with different gas exposure conditions. Based on previous studies, highly electronegative O_2 is a strong electron acceptor^{34, 35, 114} and H_2O is a strong electron donor.¹¹⁵ Generally, N_2 can be treated as chemically inert to the Bi_2Se_3 surface. Thus, we used an N_2 (ultra-high purity) environment to isolate samples from reactive gases and to establish direct proof of the two-component intrinsic dynamics.

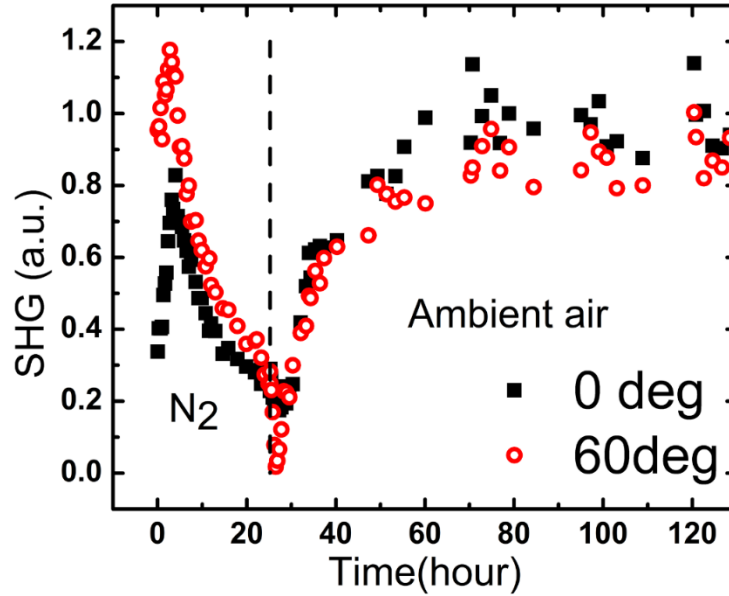


Figure 3-23 Time dependent SHG intensity with Bi₂Se₃ (Bi:Se = 0.62) cleaved in N₂ and kept for 25.23 h before exposure to ambient air at the time indicated by the dashed line.

Figure 3-23 shows the SHG evolution of a high carrier concentration sample cleaved in N₂. Both 0° and 60° azimuthal angles show a monotonic increase in about the first 3 hours, similar to Figure 3-22 (a), and a decrease afterwards. Unlike the evolution in ambient air, the decrease occurs over a much longer initial time. Once the sample is introduced to ambient air, marked by the dashed line, the signal rapidly decreases and then the whole trend of SHG repeats the slow evolution already observed for ambient air cleaves.

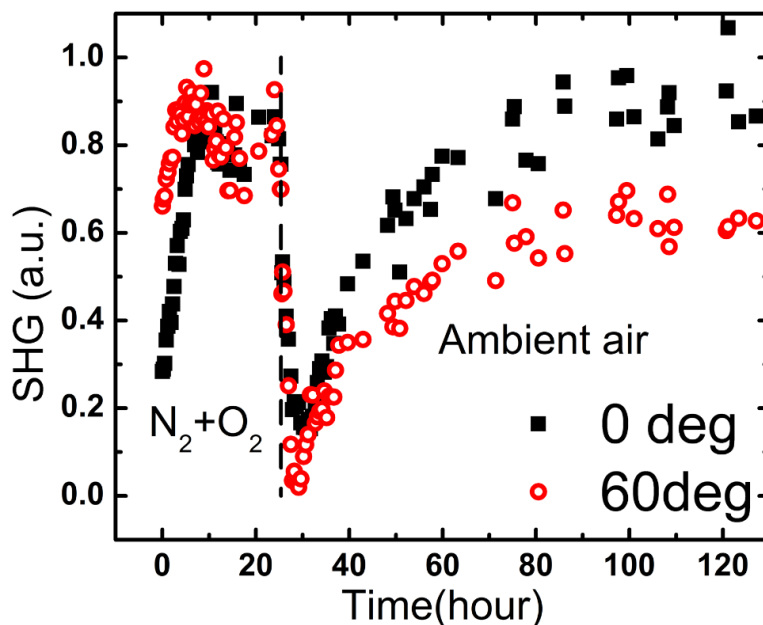


Figure 3-24 Time dependent SHG intensity with Bi_2Se_3 (Bi:Se = 0.62) cleaved in zero-air and kept for 25.38 h before exposure to ambient air at the time indicated by the dashed line.

We then performed experiments in a water-free environment by using a mixed gas (Air, zero grade) of O_2 (20%) and N_2 (80%) (also known as "zero air"). This simulates the composition of ambient air while excluding the impact of H_2O . In Figure 3-24, the results for cleaving in zero air show remarkable differences compared to the evolution in either an inert N_2 environment or in normal ambient air. In the first 4-5 hours the SHG rises to its maximum amplitude for both 0 deg and 60 deg azimuthal angles. Then it stays almost constant up until the sample is exposed to ambient air. In ambient air, the SHG signal behaves in a manner broadly consistent with the ambient air evolution in Figure 3-19, Figure 3-20 and Figure 3-21.

3.2.5 Discussion

In this section, we sketch a qualitative picture of the time dependence of electrostatic fields near the cleaved Bi_2Se_3 surface based on the SHG observations just presented. It is clear that the SHG response in Bi_2Se_3 depends on multiple processes including the intrinsic effects of charge and ionized impurity redistribution and the extrinsic effects of surface doping and impurity composition due to ambient gases. As a result, SHG exhibits a complex evolution over multiple time scales.

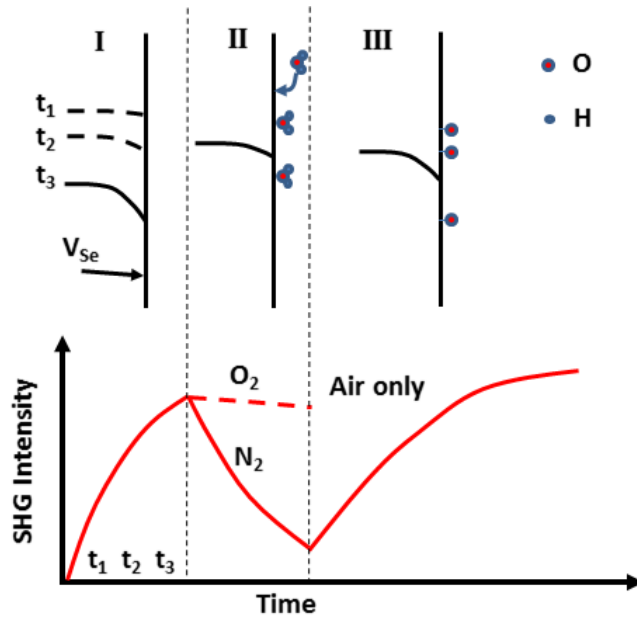


Figure 3-25 Schematic depiction of the different regimes of time evolution of the surface electric field considered in the discussion section. The top and bottom panels are schematics of the crucial physical processes in each regime and the time evolution of SHG intensity, respectively. Regime I involves gradual band bending due to redistribution of Se vacancy donors and their associated conduction band electrons. Region II shows surface adsorption of ambient gases where the arrow indicates arrival of a molecule (H_2O here, can also be N_2 or O_2) to the surface from the gas phase. Region III depicts more extensive surface oxidation where a clear chemical bond is drawn between O atoms and the surface.

The general evolution is depicted schematically in Figure 3-25. We divide the time evolution into three separate regimes that we propose are dominated by distinct physical processes. The initial rise in regime I is dominated by Se vacancy and associated free carrier motion that establishes a depletion region near the surface. The intermediate time evolution in Regime II shows the most variability depending on ambient conditions and thus inferred to be controlled by the electrostatic impact of ambient adsorbates. In ambient air, the presence of water convolutes some chemical reactivity with the electrostatic effects in this regime. The very long time evolution in Regime III shows dramatic surface changes in the SHG anisotropy and corresponds to significant surface chemical reactions in ambient air due to the combined presence of O₂ and H₂O.

3.2.5.1 Regime I: Intrinsic charge redistribution

The initial SHG response in Regime I after cleaving a sample is always dominated by the motion of the Se vacancies and free carriers results in the build-up of a depletion region near the surface. The associated electrostatic field increases the SHG signal monotonically as described by Hsieh and co-workers.^{34, 35} This process is also apparent in samples cleaved in ultra-high vacuum and cryogenic conditions where ARPES measurements show a slow shift in the Dirac point due to downward band bending at the cleaved surface.^{46, 47} The time constant for such processes is temperature dependent and at room temperature was reported to saturate in ~ 22 hours for a nominally stoichiometric sample with carrier density of ~ 10¹⁹ cm⁻³.⁴⁷ In our experiments the rate of initial SHG evolution is significantly faster, which we attribute to lower bulk carrier concentration in

our samples due to growth in excess Se. In addition, SHG evolution can be complicated by air cleaves owing to the simultaneous contribution of reactive gas adsorption.

The observation that the rate of electric field build-up near the surface depends on the sample composition (hence on carrier density) suggests a composition-dependence of Se-vacancy mobility. The larger the Se vacancy concentration inferred from melt composition, the longer the initial rise period lasts. This trend also includes the nominally p-doped samples considered in previous SHG studies^{34, 35} which observed a much more rapid initial rise than in any of our observations. Alternatively, Zhu et al. used ARPES to monitor band bending for UHV cleaves and observed a much slower initial evolution, as has already been mentioned for ~22 hours of very highly n-doped samples.⁴⁷

We hypothesize that this dependence of Se vacancy diffusion time scale on carrier density is connected to vacancy clustering at high Se vacancy concentrations that limits their mobility. A similar decrease in arsenic donor ion mobility in Si with increasing As concentration has been attributed to the formation of immobile vacancy clusters at very high impurity concentrations.¹¹⁶ From this perspective, the high rate of evolution reported in earlier SHG studies most closely reflects the diffusion of independent Se vacancies while our measurements correspond to an increasing contribution of less mobile vacancy clusters. More dedicated studies of defect dynamics are required to provide insights into the dynamics of defects in TI materials. While perhaps outside the main trend of enthusiasm in this new field, such ideas must be carefully considered in assessing possible applications.

3.2.5.2 Regime II: Adsorbate Modifications of Electrostatic Fields

Following the initial rise in Regime I the SHG intensity drops in both N₂ and ambient air. In the “zero air” mixture of N₂ and O₂, the SHG is approximately constant, with only a weak decreasing trend over multiple hours in this environment. We attribute the evolution in this time regime to be dominated by the electrostatic impact of ambient gas adsorption, especially in the controlled gas environments of nitrogen and zero air (Figure 3-23 and Figure 3-24).

The physics behind this physical process is similar to that underlying adsorbate-induced work function changes.¹¹⁷ The work function of a metal surface is determined by the barrier created due to the surface dipole layer. Even very inert adsorbates such as rare gases (or N₂ in our experiments) can have a significant impact on the surface dipole layer due to dielectric screening and Pauli repulsion.¹¹⁸ These changes have been measured using SHG intensity and correlations with direct work function changes in response to controlled gas adsorption.¹¹⁹

In an N₂ environment, the change in electrostatic field near the surface due to adsorption is attributed mostly to Pauli repulsion that tends to undo the downward band bending upon cleavage. This can be viewed as weakly adsorbed N₂ molecules slightly pushing back the negative charge that has moved toward the surface to create the surface dipole associated with downward band bending.

In “zero air”, the more reactive O₂ molecules adsorb in addition to N₂ and interact with the surface primarily by a tendency to accept electrons. In fact, an early study of the impact of work function changes on SHG intensity revealed a strong increase in SHG associated with O₂ - induced work function increase.^{120, 121} The net effect of the

competing processes of N₂ and O₂ adsorption is only a weak net modification of near-surface electric fields that leads to a nearly constant SHG intensity in Regime II. Finally, evolution in Regime II after cleaving in ambient air is more similar to N₂ and these changes are attributed to combined effects of N₂, O₂, and H₂O from the air, which are known to lead to extensive oxidation.^{40, 41} In addition, water is expected to be a strong donor adsorbate¹¹⁵ that moves the Fermi level in the opposite direction as O₂ so that the net effect is plausibly a work function reduction as observed in our SHG evolution. Furthermore, in ambient air the evolution in regime II may not be entirely electrostatic in origin due to simultaneous contributions from surface chemical changes due to O₂ and H₂O. This possibility is suggested in the 2D plot in Figure 3-20 where a reversal in relative intensity of the SHG anisotropy occurs already near the end of the slow Regime II decay. This suggests that reactive surface restructuring occurs simultaneously with the electrostatic effects in the controlled gas environments.

3.2.5.3 Regime III: Chemical Modification of the Surface

After long exposure to ambient air, the changes in SHG signal are dramatic and independent of sample composition or previous sample environment. After 1 day in air, the SHG signal shows a monotonic rise toward saturation. This time scale corresponds with the onset of observable oxidation due to air exposure in X-ray photoelectron spectroscopy experiments⁴¹. In addition, the reversal of relative intensities in the SHG anisotropy shows that at these long times the surface structure is altered significantly compared to the pristine cleaved surface. This is consistent with new surface covalent bond formation as indicated schematically in Figure 3-25.

It is important to note that this surface chemical reaction only occurs in the presence of ambient air, which has been previously shown to be due to the combination of O_2 and H_2O .⁴⁰ In either N_2 or zero air (N_2+O_2) the gradual electrostatic-dominated decay persists for very long times without a change in relative intensities in SHG anisotropy. This is consistent with the recent XPS study that showed minimal reactivity of the Bi_2Se_3 surface to O_2 alone and only significant oxidation due to the presence of O_2 and H_2O .⁴⁰ It is likely that at least some surface covalent bonds to hydroxyl species are formed in this situation, though explicit demonstration of this specific surface species does not yet exist.

Finally, we remark that the very significant changes in SHG anisotropy due to surface oxidation in ambient air could be amenable to treatment within the bond models of SHG developed by Aspnes and co-workers⁹⁹ and applied extensively to Si surface oxidation.^{94, 122-124} This would lead to important microscopic insights into surface chemical bonding via the associated changes in bond hyperpolarizabilities.

3.2.6 Conclusions

The results presented here show that the time evolution of electrostatic fields near the surface of the topological insulator after a mechanical cleave exhibits extraordinary complexity that can involve both intrinsic charge redistribution and extrinsic effects due to gas adsorption and surface chemical reactions. These changes were probed by monitoring SHG intensity over time for different samples and in different gas environments. Our analysis of the SHG evolution suggests a general trend that near surface electric field evolution is faster with fewer Se vacancies and hence lower carrier densities. This is probably due to a reduction in Se vacancy mobility for higher vacancy

concentrations, which leads to clustering. Furthermore, the evolution of an electric field is substantially impacted by an ambient gas environment that can lead to adsorption-induced changes in electrostatic fields near the surface by Pauli repulsion and charge transfer. Finally, it was shown that significant oxidation in ambient air over the course of 1-3 days changes the electrostatic field near the surface as well as the surface symmetry by monitoring qualitative changes in SHG anisotropies.

Our SHG observations exemplify the materials science challenges associated with even the simplest topological insulators, like Bi_2Se_3 , are significant. Complexities of charge redistribution and surface contamination and reactivity effects mean that the details of sample surface preparation will play a major role in determining the measureable sample properties. We note in particular that SHG evolution shows marked sample variations would be expected depending on the time scale of experiments up to several days after mechanical cleaving of a new surface. Even though the topological character of Bi_2Se_3 is expected to be extremely robust to surface contaminants and field effects, experimental access to the unique TSS is not robust to surface and near surface effects. Controlling these interfacial complexities is contingent upon careful sample handling, preparation, and experimental design.

3.3 MoS_2 and WS_2 Monolayers³

3.3.1 Overview

Two-dimensional (2D) transition metal dichalcogenide (TMDC) materials such as monolayer MoS_2 and WS_2 promise the development of atomic-scale light emission

³ This work is in part submitted for publication on peer reviewed journal.

devices, but their luminescence efficiencies are very low despite perfect surface passivation and strong exciton binding energy. Here it is demonstrated that the luminescence efficiency is significantly limited by the substrate and can be improved by orders of magnitude through substrate engineering. The substrate effects mainly lie in doping the monolayers and affecting the monolayers' exciton dynamics, including facilitating the non-radiative recombination and slowing the radiative decay. Using proper substrates like mica and Teflon can minimize the adverse effect of doping, and by suspending the monolayer can mitigate both effects. Suspended monolayers generally show luminescence efficiency more than one order of magnitude higher than supported monolayers, which can be up to 40% at room temperatures. The result provides useful guidance for the rational design of high-performance 2D TMDC light emission devices. Here in this thesis, the focus is mainly on the ultrafast exciton dynamics of the suspended and substrate-supported MoS₂ and WS₂ monolayers.

3.3.2 Experimental Methods

The MoS₂ (WS₂) monolayers were grown using a chemical vapor deposition (CVD) reported previously¹²⁵. Typically, 1 g sulfur powder (Sigma-Aldrich) and 15-30 mg MoO₃ (WO₃) (99.99%, Sigma-Aldrich) source material were placed in the upstream and the center of a tube furnace, respectively. And substrates (usually sapphire) were placed at the downstream of the tube. Typical growth was performed at 750 °C (900 °C) for 10 (30) minutes under a flow of Ar gas in rate of 100 sccm and ambient pressure.

The transfer of the monolayers followed a surface-energy-assisted transfer approach reported previously¹²⁶. In a typical transfer process, 9 g of polystyrene (PS) with a

molecular weight of 280 kg/mol was dissolved in 100 mL of toluene, and then the PS solution was spin-coated (3000 rpm for 60 s) on the as-grown monolayers. This was followed by a baking at 80–90 °C for 1 hour. A water droplet was then dropped on top of the monolayer. Due to the different surface energies of the monolayer and the substrate, water molecules could penetrate under the monolayer, resulting the delamination of the PS-monolayer assembly. We could pick up the polymer/monolayer assembly with a tweezers and transferred it to different substrates. After that, we baked the transferred PS-monolayer assembly at 80 °C for 1 h and performed a final baking for 30 min at 150 °C. Finally, PS was removed by rinsing with toluene several times.

PL measurement was performed using a home-built setup that consists of a confocal microscope (Eclipse C1, Nikon) connected with a monochromator (SpectraPro, Princeton Instruments) and a detector (Pixis, Princeton Instruments) with an excitation wavelength of 532nm (Verdi G5, Coherent). Photoluminescence (PL) mapping was carried out by Horiba Labram HR800 system with a 532 nm laser. Raman spectra were collected on a Renishaw-1000 Raman spectroscopy with an excitation wavelength of 514.5 nm. Shimadzu UV-3600 UV-VIS-NIR Spectrophotometer and Edinburgh FL/FS920 Spectrometer were used to measure the absorption and PL of rhodamine-6g (R6G) doped PMMA film and rhodamine-6g solution (300 μM in methanol).

We performed the first-principles calculations by using Vienna ab initio simulation package (VASP) within the framework of density functional theory (DFT). Van der Waals corrected functional with Becke88 optimization (optB88) was adopted to consider the dispersive interaction between the MoS₂ and the substrate. A kinetic energy cutoff of 400 eV of the plane wave basis was used. We used a criterion for the k-point sampling

based on Monkhorst-Pack (MP) grid such that the number of the k points along the in-plane periodic direction was determined by the smallest integer that fulfills $nkL=60 \text{ \AA}$, where L is the lattice constant of the supercell in the periodic direction. The various substrates supported MoS₂ systems were simulated by creating slab models and supercells were created by consider the lattice commensuration between each type of substrate and the MoS₂ layer. A vacuum layer with thickness greater than 15 \AA was adopted to avoid the spurious interaction due to the periodic image and dipole corrections were implemented to consider the asymmetry of the slabs. The structures were relaxed until the forces on each atom are less than 0.005 eV/ \AA . To analyze the charge dynamics across the MoS₂-substrate interface, we calculated the differential charge density (DCD) $\Delta\rho(\mathbf{r})$ and the plane-averaged DCD $\Delta\rho(z)$ along the direction normal to the interface by integrating DCD within the x-y plane. The amount of transferred charge at the z point from the bottom layer was obtained according to $\Delta Q(z) = \int_{-\infty}^z \Delta\rho(z') dz'$.

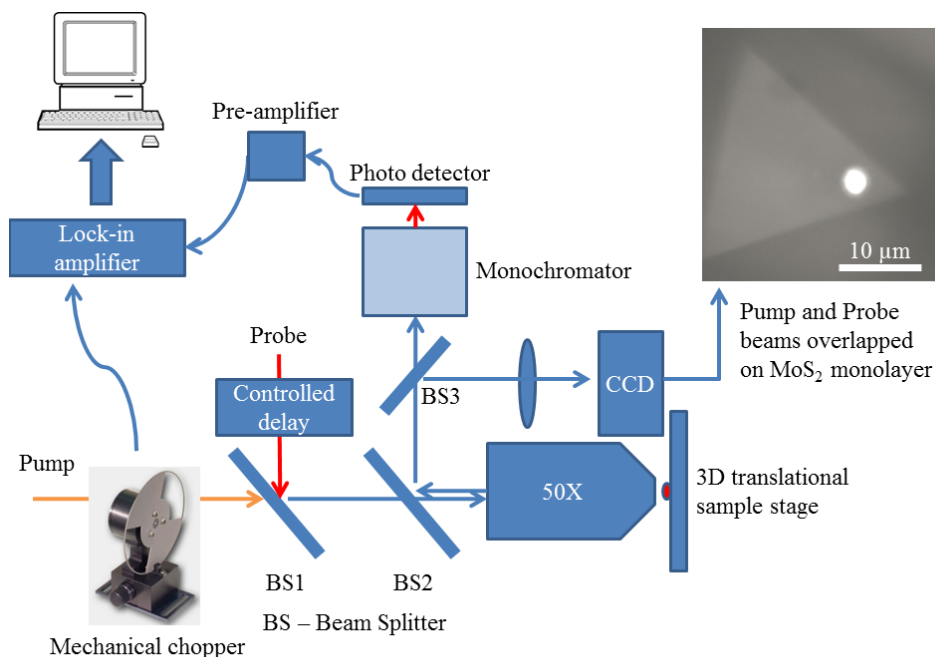


Figure 3-26 Diagram of Transient Reflection Spectroscopic Microscopy (TRSM).

Exciton dynamics was studied by transient reflection (TR) spectroscopy. Because of the limited sample size (typically in $\sim 10 \mu\text{m}$), regular pump-probe experiment cannot image the sample and focus pump and probe beams precisely within the sample region. For this purpose, we investigated the exciton dynamics in the suspended and substrate-supported monolayers by self-developed transient reflection spectroscopic microscopy (TRSM), as diagramed in Figure 3-26. The pump pulse at 2.10 eV was used to pump electrons from the valence band into conduction band of the monolayers. The pump fluence was chosen to be small enough such that the differential reflection ($\Delta R/R$) of the probe beam is linearly dependent on the concentration of photoexcited charge carriers at the band edges. The differential reflection ($\Delta R/R$) of a time-delayed pulse, whose wavelength was chosen to match the A exciton ($\sim 1.88 \text{ eV}$ for MoS₂ and $\sim 2 \text{ eV}$ for WS₂, respectively), was used to probe the monolayers after the photoexcitation.

In Figure 3-26, the pump and probe beams were collinearly polarized before entering into a 50X long working distance objective (TU Plan EPI ELWD, Nikon) and the reflected probe pulse was collected using the same objective. The size of the focused beam was about 2 μm in diameter. The reflected probe beam was collected through a monochromator (CM110, Spectral Products) into a Si photodiode (DET10A, Thorlabs). The signal from the Si photodiode was pre-amplified by a photodiode amplifier (PDA200C, Thorlabs) and DR was measured using a lock-in amplifier (SR810, Stanford Research Systems). The pump beam was mechanically chopped (SR540, Stanford Research Systems) at 400 Hz yielding to the narrowed bandwidth (1kHz) of the photodiode amplifier while operating at high amplification mode. Typical pump fluence used in the experiment was 10 $\mu\text{J}/\text{cm}^2$. This was to ensure that only a minor fraction of the density of state at the band edges could be filled (<5% as estimated). The time delay between pump and probe pulses was controlled by changing the optical path length of the probe beam with the probe beam reflected by a retroreflector fixed on a mechanical delay stage (ILS250CC, Newport) controlled by a motion controller (ESP300, Newport). The motion controller, the monochromator, and the lock-in amplifier were connected to a computer, where all the controls and signal processing were finished with a self-compiled LABVIEW code.

The microscopic image of the sample was resolved by inserting a LED light source between the monochromator and BS3 and shining whitelight onto the sample through the objective. The reflected image by BS2 and BS3 was focused through a lens ($f=15\text{ cm}$) onto a CCD camera (EO-5012, Edmund Optics). The inset at the upper-right corner

shows a typical image of the sample with pump and probe beams overlapped on it. As a side note, the LED light source was removed during the DR measurement.

Unless otherwise specified, all experiments were performed at room temperature in ambient air. The detailed laser specifications can be found in Appendix A. Temperature dependent experiments were performed with the sample stored in a cold finger continuous-flow cryostat (ST-500, Janis) cooled by liquid nitrogen.

3.3.3 Exciton dynamics on MoS₂ and WS₂ monolayers

In this section, we will focus on the investigation of exciton dynamics on suspended and substrate supported MoS₂ and WS₂ monolayers. Through the compare of exciton dynamics, we can find out the underlying effects from the substrate.

Specifically, we can also quantitatively evaluate the rate of exciton-exciton annihilation (EEA) based on the exciton dynamics. The substrate has a significant effect on the EEA rate as revealed by TRSM.

3.3.3.1 Suspended versus substrate-supported monolayers

We started with examining the PL of suspended MoS₂ and WS₂ monolayers and compared it with that of as-grown monolayers. The monolayers were synthesized on sapphire substrates using a chemical vapor deposition (CVD) process reported previously.¹²⁷⁻¹²⁹ The suspended monolayers were prepared by manually transferring¹²⁶ the synthesized monolayers from sapphire substrates onto SiO₂/Si substrates pre-patterned with holes (Figure 3-27 a&b). The power density of the incident laser (532 nm) used in the PL measurement was controlled to be small enough to ensure no substantial

heating generated in the monolayers. Significantly, the suspended monolayers show PL intensities more than one order of magnitude (~30-60 times) stronger than the as-grown counterparts (Figure 3-27 c&d) under the same incident power. We quantitatively evaluate the quantum yield (QY, the number of photons emitted versus the number of photons absorbed) of the monolayers by using R6G dye molecules as a reference.^{130, 131} The evaluation takes into account the different absorption efficiencies of the suspended and as-grown monolayers for the incident light. The QYs (PL efficiency) are found to be 0.15% and 5% for the supported and suspended MoS₂, and 3% and 40% for the supported and suspended WS₂ monolayers, respectively. The PL measurements were performed in ambient environment, but we can exclude out the effect of air-borne moistures on the measured PL as we did not observe any changes in the PL and topology of the monolayer with increased ambient exposure time. According to previous studies, changes in the PL and topology would be expected when substantial amount of air-borne moistures are adsorbed.¹³²

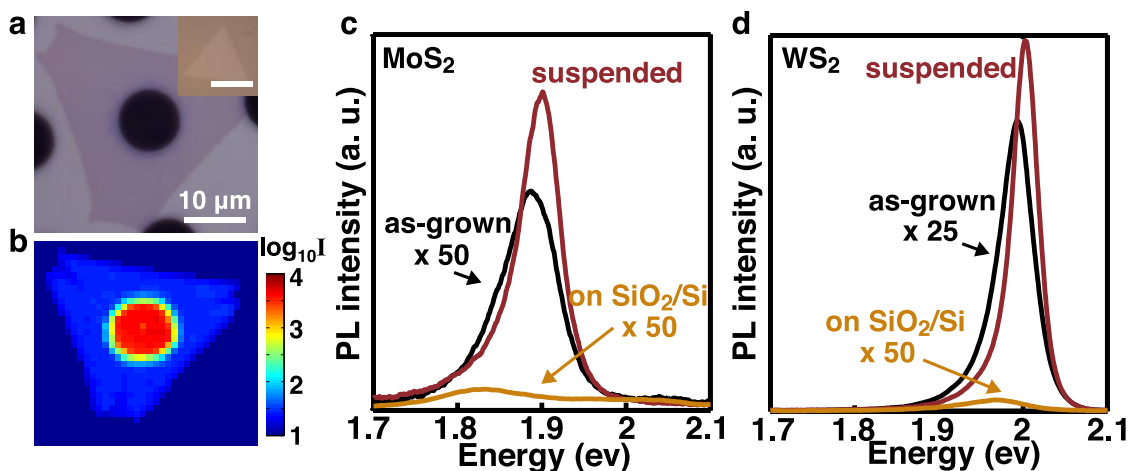


Figure 3-27 Dramatically improved PL efficiency of suspended monolayer MoS₂ and WS₂. (a) Optical image of a typical suspended monolayer. Inset: optical image of as-grown monolayers with a scale bar of 10 μm. (b) PL mapping of a typical suspended monolayer. The colorbar of PL intensity is in log scale. (c) PL spectra of as-grown monolayer MoS₂, suspended monolayer MoS₂, and the monolayer MoS₂ transferred onto SiO₂/Si substrates. The spectra of the as-grown monolayer and the monolayer MoS₂ transferred onto SiO₂/Si substrates are multiplied by 50 for visual convenience. (d) PL spectra of as grown monolayer WS₂, suspended monolayer WS₂, and the monolayer WS₂ transferred onto SiO₂/Si substrates. The spectra of the as-grown monolayer and the transferred monolayer on SiO₂/Si substrates are multiplied by 25 and 50, respectively, for visual convenience.

We can exclude out the transfer process to be the reason for the improved PL efficiency of the suspended monolayers. The transfer process has been previously demonstrated able to transfer the synthesized monolayers onto arbitrary substrates without compromising the crystalline quality¹²⁶. The preservation of the crystalline quality during the transfer process is also supported by the uniform, strong PL observed at the suspended monolayers (Figure 3-27 b). Additionally, the supported part of the transferred monolayer, which has experienced the same transferring process as the suspended part, shows PL intensities even weaker than that of the as-grown one (Figure 3-27 c). Should the transfer process have introduced defects in the monolayers,^{133, 134} which could enable improvement in the PL efficiency, we would expect a non-uniform

spatial distribution of PL intensity in the suspended monolayer and would also expect similarly improved PL efficiencies at both the supported and suspended parts of the transferred monolayers. This is apparently not what observed in experiments here. Actually, we found that the transfer process may likely lower the PL efficiency by inducing n-doping to the monolayers. For instance, the monolayer transferred onto sapphire substrates shows much weaker (by more than one order of magnitude), broader, and red-shifted PL compared to the as-grown one on sapphire substrates, indicating more n-doping in the transferred monolayer. This doping can be correlated to the residual moisture trapped between the monolayer and the substrate.¹³² We have confirmed that the other chemicals involved in the transfer process, including polymer (polystyrene), solvent (toluene), and the moisture adsorbed on top of the monolayer, can all be readily removed by the baking(200 °C under Ar) in the transfer process and may leave only minor effects to the PL afterward. Moisture is able to dramatically lower the PL efficiency by orders of magnitude through n-doping the monolayers,¹³⁵ and the n-doping may facilitate the formation of trions (charged excitons) that have lower luminescence, broader emission peaks, longer emission wavelengths than neutral excitons.¹³⁶ Therefore, we can conclude that the absence of the substrate, instead of the involvement of the transfer process, leads to the improved PL efficiency of the suspended monolayers.

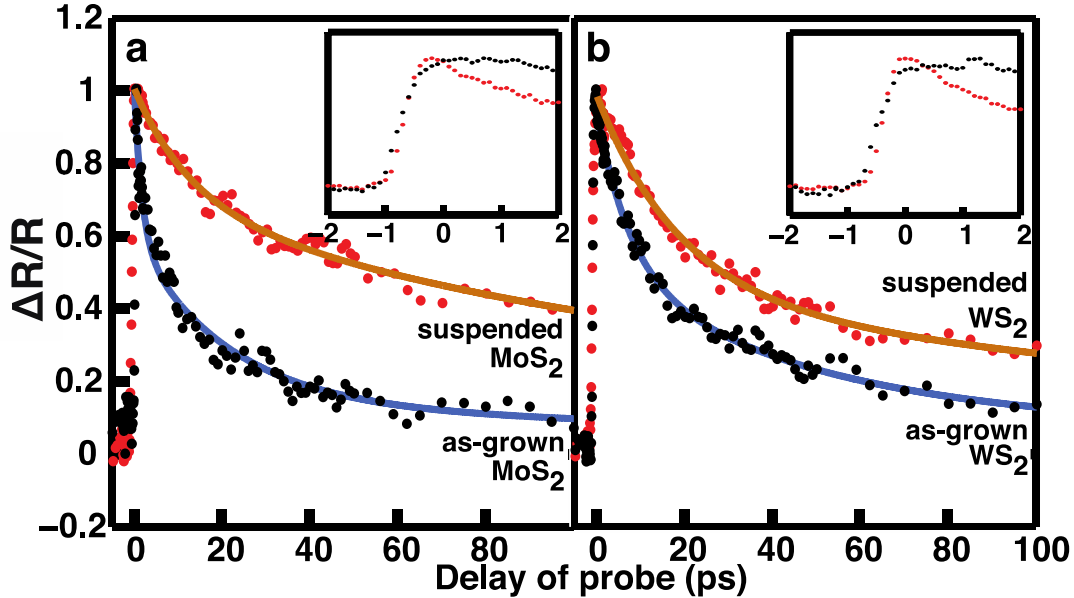


Figure 3-28 Exciton dynamics of suspended and supported monolayers. The normalized DR of the probe pulse from (a) suspended and as-grown MoS₂ monolayers and (b) suspended and as-grown WS₂ monolayers as a function of the probe delay. The insets are magnified versions for the measured results around the zero-ps decay. Both experimental (dotted lined) and fitted (solid lines) results are plotted.

To better understand the mechanism underlying the improved PL efficiency of the suspended monolayers, we investigated the exciton dynamics in the suspended and supported monolayers using TRSM. Figure 3-28 shows the normalized $\Delta R/R$ results measured at the suspended and as-grown MoS₂ and WS₂ monolayers. Upon photoexcitation, $\Delta R/R$ arises to its maximum value within ~ 500 fs. This corresponds to the cooling of photoexcited charge carriers down to the band edges and the measured timescale of ~ 500 fs is due to the limited resolution because of the chirp in the supercontinuum light used as the probe, consistent with what previously reported⁸⁶. It is followed by a decrease of $\Delta R/R$ with time that results from the decay of the charge carriers at band edges. We confirmed no substantial heating effect in both suspended and

supported monolayers at the pump fluence used in the experiment (Figure 3-29 and Figure 3-30).

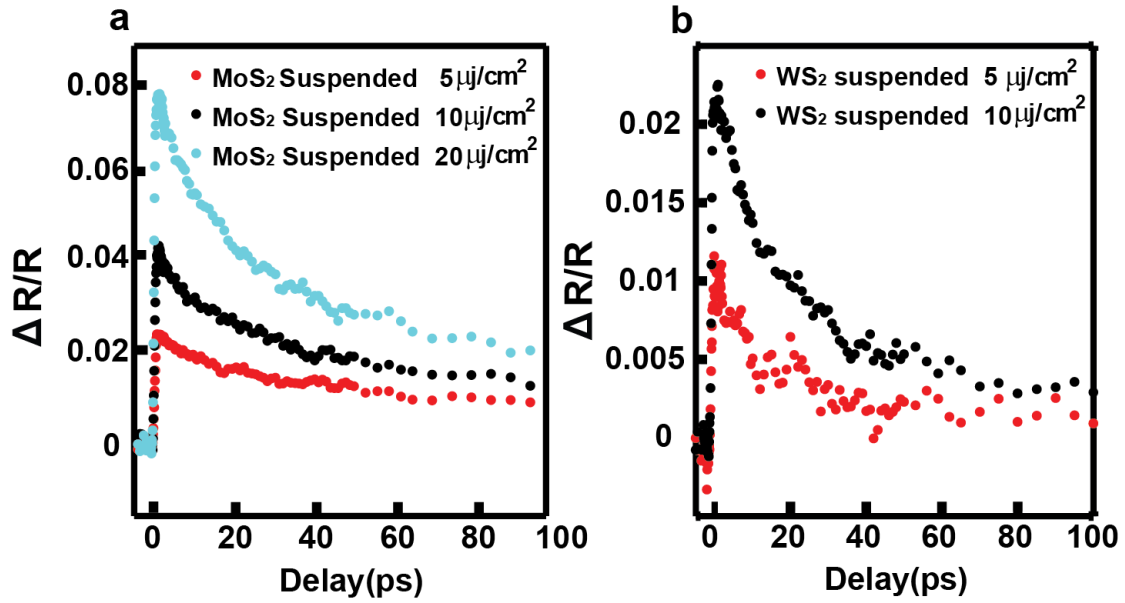


Figure 3-29 Dependence of transient reflection $\Delta R/R$ of suspended monolayers on pump fluence. (a) For suspended MoS₂ monolayer and (b) For suspended WS₂ monolayer. The $\Delta R/R$ at the peak is linearly dependent on the pump fluence, and this indicates no substantial heating effect with the applied pump fluence.

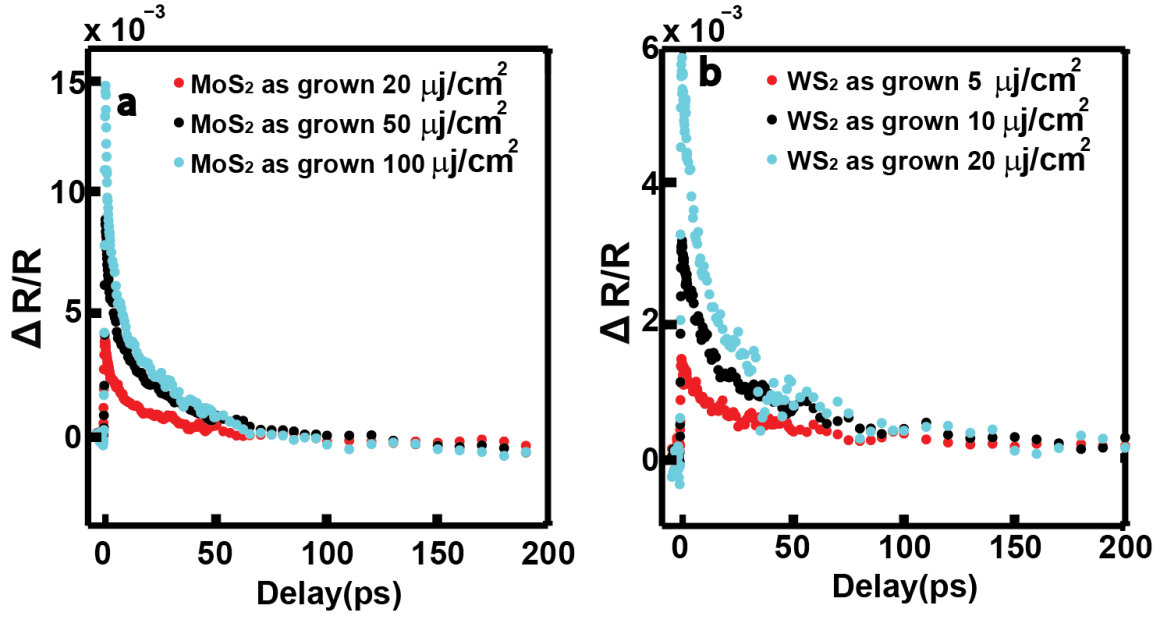


Figure 3-30 Dependence of transient reflection $\Delta R/R$ of as-grown monolayers (sapphire substrates) on pumping fluence. (a) For MoS₂ monolayer and (b) For WS₂ monolayer. The $\Delta R/R$ at the peak is linearly dependent on the pump fluence, and this indicates no substantial heating effect with the applied pump fluence.

The dynamics measurement provides useful insights into the improved PL of suspended monolayers. There is no obvious resolved difference in the cooling of hot charge carriers between the suspended and supported monolayers as both show similar time for the $\Delta R/R$ to rise to its maximum value. However, the decay of the charge carriers in the suspended monolayers is substantially slower than that in the supported monolayers. We fit the experimental result using multiple exponential functions $A_1 e^{-t/\tau_1} + A_2 e^{-t/\tau_2} + A_3 e^{-t/\tau_3}$ (fitted parameters are in Table 3-1) as what previously done by other groups^{84, 85, 87}.

Table 3-1 Fitting parameters for the measured dynamic results on as-grown MoS₂ and WS₂ monolayers.

	A ₁	A ₂	A ₃	τ ₁ (ps)	τ ₂ (ps)	τ ₃ (ps)
As-grown MoS ₂	0.44	0.49	0.13	1.72	21.3	~250
Suspended MoS ₂	0.31	0.56	0.13	12.0	132	~5000
As-grown WS ₂	0.42	0.44	0.07	7.5	49	~3200
Suspended WS ₂	0.55	0.39	0.04	18.8	192	~3750

Although the physical processes involved in the decay is not well understood at this moment, the fitting nevertheless may provide useful quantitative insight into the dynamics. It indicates that τ₁ changes from ~1-3 ps to ~12 ps and τ₂ from ~20 ps to ~100-130 ps for the supported and suspended MoS₂, and for the supported and suspended WS₂ τ₁ changes from ~6-8 ps to ~20 ps and τ₂ from ~50 ps to ~170-200 ps, respectively. The less increase at the suspended WS₂ is related with the materials' stronger exciton binding energy, which may make the dynamics less susceptible to the influence of the substrate. The time scale τ₃ substantially varies from hundreds to thousands of picoseconds even in the same kinds of samples and no obvious difference can be found between the suspended and supported monolayers. It is safe to conclude that the decay process of τ₃ does not provide any significant contribution to the PL and thus is not of our interest. The increase of exciton lifetime indicates the suppression of non-radiative recombinations that dominate the exciton decay as indicated by the observed PL efficiency. Previous studies have demonstrated that the interband recombination of charge carriers in supported monolayers is assisted by defects,^{137, 138} and this is also confirmed by our own results of no pump or temperature dependence (Figure 3-31). The observed increase of exciton lifetime also indicates that the substrate stands as a major source for the defects involved

in the decay. The removal of the substrate essentially eliminates the non-radiative decay mediated by the defects at the surface of the substrates.

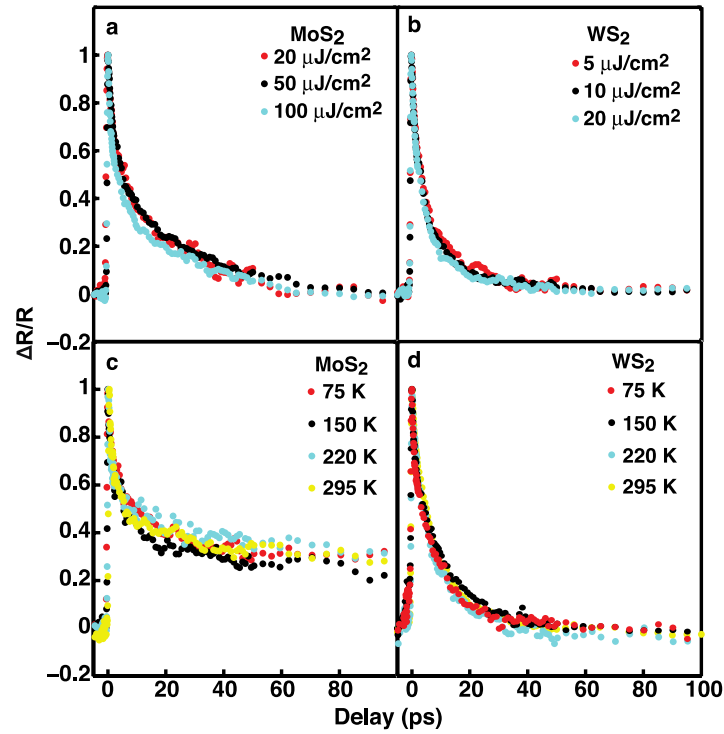


Figure 3-31 Independence of the transient reflection $\Delta R/R$ on pumping fluence and temperature. Normalized differential reflection $\Delta R/R$ of (a) as-grown monolayer MoS₂ and (b) as-grown monolayer WS₂ on sapphire substrates as a function of pumping fluence. Normalized differential reflection $\Delta R/R$ of (c) as-grown monolayer MoS₂ and (d) as-grown monolayer WS₂ on sapphire substrates as a function of temperatures, 75K, 150K, 220K, and 295K. The result indicates negligible dependence of the differential reflection on the pumping fluence and temperature, suggesting the dominance of defect-assisted recombination as reported previously.

3.3.3.2 Different substrate-supported monolayers

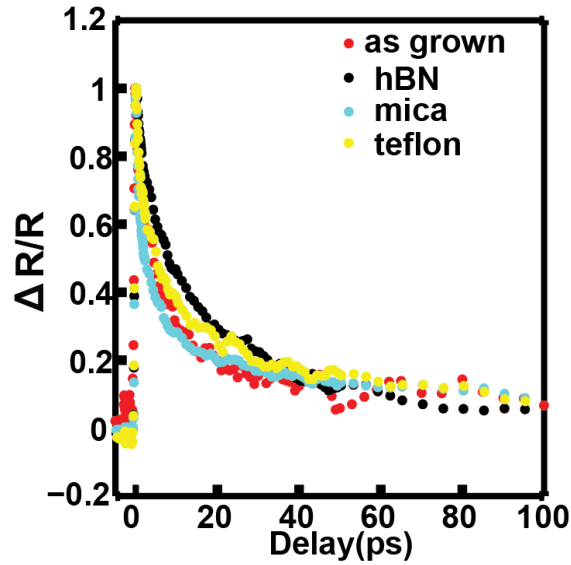


Figure 3-32 Comparable exciton dynamics in the supported monolayer MoS₂ on typical substrates. Normalized transient reflection $\Delta R/R$ shows similar decay trends for all the supported monolayers.

It is worthwhile to point out that all the supported monolayers, show similar exciton lifetimes (Figure 3-32 and Table 3-2). Nevertheless, in Figure 3-27 c&d, dramatic differences in PL intensities have been observed on as grown and SiO₂/Si supported MoS₂ (WS₂) monolayers, which indicates factors other than exciton dynamics affecting the PL.

Table 3-2 Fitting parameters for the measured dynamics results on different substrate supported MoS₂ monolayers.

	A ₁	A ₂	A ₃	τ_1 (ps)	τ_2 (ps)	τ_3 (ps)
As-grown MoS ₂	0.44	0.49	0.13	1.72	21.3	~250
MoS ₂ on Mica	0.56	0.29	0.14	1.5	21	~290
MoS ₂ on Teflon	0.37	0.49	0.18	1.7	24	~1000
MoS ₂ on hBN	0.26	0.58	0.19	2.1	25	~700

To better understand the role of the substrate in the PL, we investigated the PL of the monolayers on a wide variety of substrates. Figure 3-33 (a) shows the PL collected from the monolayer MoS₂ on typical substrates studied. As the absorption efficiencies of the monolayers on the different substrates for the incident laser (532 nm) are similar, the different PL intensities reflect different PL efficiencies (QY). Mica may enable the strongest PL among all the substrates tested, around three times as good as sapphire substrates. It is followed by Teflon. Hexagonal boron nitride (h-BN), which has been reported to be a good substrate for monolayer electronic devices,^{75, 139} is not as good as mica and Teflon in terms of promoting the PL. We can exclude out substrate-induced strains to be the major reason for the observed substrate-dependent PL efficiencies. Raman measurements show only minor difference in the frequency of the E_{2g}¹ peak, which is known to be sensitive to the strain¹⁴⁰⁻¹⁴², in the supported monolayers (Figure 3-33 b). It indicates that the strain in the supported monolayer is usually less than 1%.^{80, 81, 140} The small substrate-induced strain is consistent with what reported previously and what intuitively expected given the weak interaction (van der Waals forces) of the monolayers with the substrates.¹⁴³ The influence of such a small strain on PL efficiency is expected to be no more than 10-15%, far smaller than the observed difference.

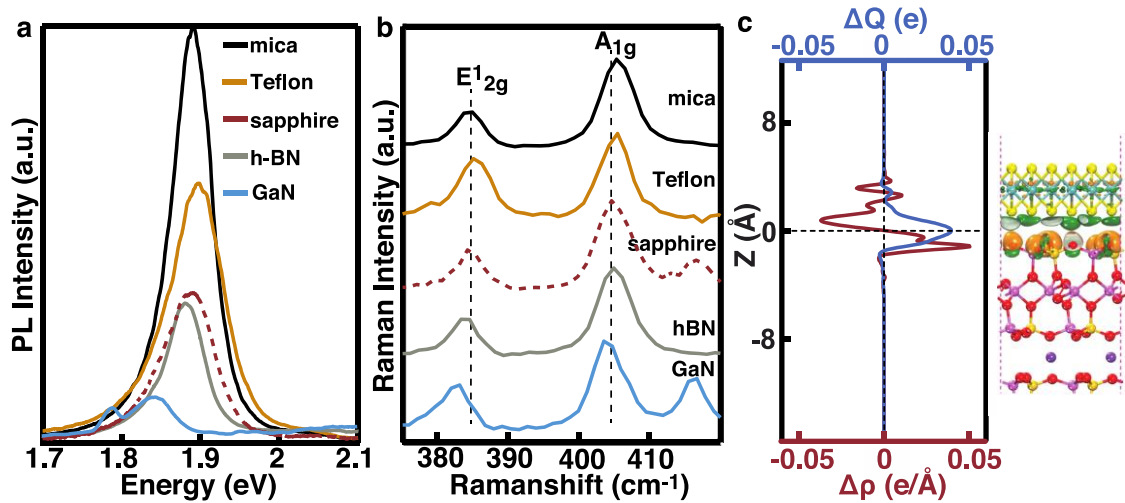


Figure 3-33 Substrate-dependent PL efficiency of supported monolayers. (a) PL spectra of monolayers MoS₂ on typical substrates. (b) Raman spectra of monolayers MoS₂ on different substrates. The two dashed lines indicate the E_{12g} and A_{1g} peaks of the as-grown monolayer. (c) Calculated charge transfer between monolayer MoS₂ and mica substrate, which shows plane-averaged differential charge density $\Delta\rho$ (red line) and amount of transferred charge ΔQ (blue line) as a function of the distance in the vertical direction. Also shown is a sideview of the structure used in the calculation (right).

The different PL efficiencies of the supported monolayers can be mainly correlated to the effect of doping. The doping level is known to dictate the population ratio of neutral excitons and trions (charged excitons) in monolayer MoS₂ and WS₂.^{82, 136} To compare the doping level in the supported monolayers, we evaluated the ratio of trion and exciton emissions by numerically fitting the PL spectra (see Table 3-3). The fitting result shows that the higher PL efficiency is indeed generally accompanied with a lower ratio of trion emission, indicating a lower n-doping level. For instance, the monolayer on mica substrates shows a ratio of trion emission obviously smaller than the as-grown monolayer on sapphire substrates, while the monolayer grown on GaN substrates, whose PL efficiency is lower, exhibits a higher ratio of trion emission. The different doping levels in the supported monolayers is also evidenced by Raman measurements.^{133, 140} The A_{1g}

peak, which may red shift with increase of n-doping, of the monolayers transferred onto mica substrates can be found blue shifting compared to that of the as-grown monolayers on sapphire. While stronger van der Waals interaction in the vertical direction may also cause the A_{1g} peak to blue shift,¹⁴⁴ the observed blue shift is due to the change of doping level since the interaction of the transferred monolayer with substrates is expected not as intimate as the as-grown one. Additionally, we simulated the charge transfer between the monolayer and the substrates using DFT techniques (Figure 3-33 c). The simulation result (Table 3-3) confirms that mica can provide the best capability to attract electrons from monolayer MoS_2 (positive charge transfer) among all the substrates studied, followed by Teflon.

Table 3-3 Exciton peak versus Trion peak ratios in PL spectra and DFT simulated substrate-induced dopings.

	Exciton : Trion	Charge Transfer
MoS_2 – Teflon	1 : 0.12	-0.003
MoS_2 – Mica	1 : 0.08	0.067
MoS_2 – hBN	1 : 0.11	-0.005
MoS_2 – As-grown	1 : 0.13	-0.003
MoS_2 – Suspended	1 : 0.075	N/A
MoS_2 – GaN	1 : 0.213	-0.043

3.3.3.3 Exciton-exciton annihilation (EEA) on MoS_2 and WS_2 monolayers

Besides the dramatic differences in the exciton dynamics on suspended and substrate-supported MoS_2 and WS_2 monolayers, which is mostly from the single-body effect, many-body effects can show up on the well-confined monolayers as well⁶⁰. For instance, the two-body effects, EEA will present obviously when exciton density is high (in the early time of pump excitation). Here, we can extract out the EEA rates from

exciton dynamics on suspended and substrate-supported monolayers, respectively. Our result shows strong EEA rates in the monolayers with amplitude depending on the presence of substrates.

If assuming that the exciton decay is dominated by EEA, the rate equation of exciton density can be written as a function of the rate constant of EEA k_{ee} :

$$\frac{dN}{dt} = -k_{ee} N^2$$

Equation 3-13

The solution to Equation 3-13 is:

$$N(t) = \frac{N_0}{1 + k_{ee} N_0 t}$$

Equation 3-14

And the exciton density $N(t)$ can be correlated to the total photo-generated excitons N_0 as:

$$\frac{N_0}{N(t)} - 1 = k_{ee} N_0 t$$

Equation 3-15

Assuming that each absorbed photon may generate one exciton at the band edge, as our peak $\Delta R/R - (\Delta R/R)_t$ is linearly dependent on the pump fluence, we can get the relationship between DR and exciton density:

$$\frac{N_0}{N(t)} = \frac{(\Delta R/R)_0}{(\Delta R/R)_t}$$

Equation 3-16

Thus, by combining Equation 3-15 and Equation 3-16, we get:

$$\frac{(\Delta R/R)_0}{(\Delta R/R)_t} - 1 = k_{ee} N_0 t$$

Equation 3-17

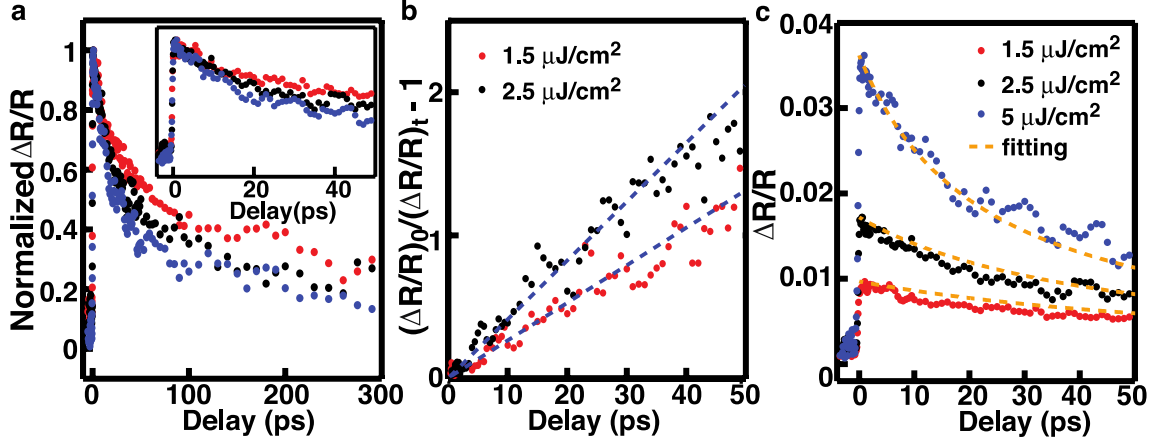


Figure 3-34 Dependence of the exciton dynamics on pumping fluence for suspended MoS₂ monolayers. (a) Normalized differential reflection of suspended MoS₂ as a function of the time delay and with different pumping fluences, 1.5 $\mu\text{J}/\text{cm}^2$ (red), 2.5 $\mu\text{J}/\text{cm}^2$ (black), and 5.0 $\mu\text{J}/\text{cm}^2$ (blue). Inset: the results for the early stage of the decay. (b) The result of $(\Delta R/R)_0/(\Delta R/R)_t - 1$ derived from the data in (a) as a function of the delay time. The result for the pumping fluence of 5.0 $\mu\text{J}/\text{cm}^2$ is not shown for the visual convenience. (c) Fitting for the measured differential reflection of suspended MoS₂ with different pumping fluences, The fitted results are plotted in dashed lines and the experimental results are dots, 1.5 $\mu\text{J}/\text{cm}^2$ (red), 2.5 $\mu\text{J}/\text{cm}^2$ (black), and 5.0 $\mu\text{J}/\text{cm}^2$ (blue).

For MoS₂ monolayer, we derive $(\Delta R/R)_0/(\Delta R/R)_t - 1$ from the data given in Figure 3-34a, which is plotted as a function of the delay time in Figure 3-34b. The result shows that $(\Delta R/R)_0/(\Delta R/R)_t - 1$ linearly depends on the delay time at the early stage of the decay (up to 50-100 ps) and the corresponding slope linearly increase with the pumping fluence (Figure 3-34b). This is consistent with what expected from Equation 3-17, indicating that the decay of the exciton is indeed dominated by EEA at the early delay time. The same rules can be applied to WS₂ monolayers as well in Figure 3-35.

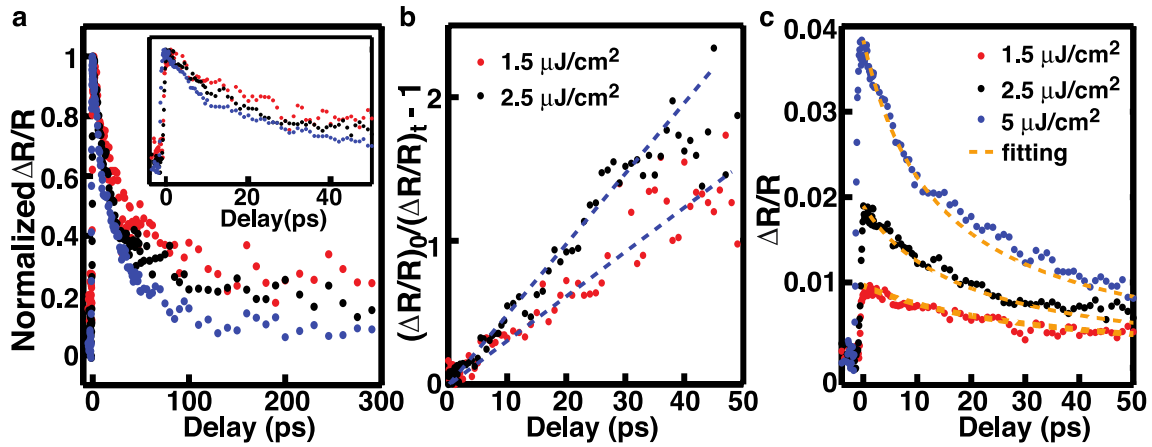


Figure 3-35 Dependence of the exciton dynamics on pumping fluence for suspended WS₂ monolayers. (a) Normalized differential reflection of suspended WS₂ as a function of the time delay and with different pumping fluences, 1.5 $\mu\text{J}/\text{cm}^2$ (red), 2.5 $\mu\text{J}/\text{cm}^2$ (blue), and 5.0 $\mu\text{J}/\text{cm}^2$ (black). Inset: the results for the early stage of the decay. (b) The result of $(\Delta R/R)_0/(\Delta R/R)_t - 1$ derived from the data in (a) as a function of the delay time. The dashed line serves to illustrate the slope of the result. (c) Fitting for the measured differential reflection of suspended WS₂ with different pumping fluences, The fitted results are plotted in dashed lines and the experimental results are dots, 1.5 $\mu\text{J}/\text{cm}^2$ (red), 2.5 $\mu\text{J}/\text{cm}^2$ (blue), and 5.0 $\mu\text{J}/\text{cm}^2$ (black).

The total photo-generated excitons N_0 can be calculated using the absorption efficiency of the monolayers (0.061 and 0.058 in suspended MoS₂ and WS₂ for the pumping wavelength), which can be estimated with the refractive index of the monolayers¹⁴⁵. We can thus evaluate the rate constant k_{ee} to be 0.1 cm^2/s and 0.3 cm^2/s for suspended MoS₂ and WS₂ monolayers, respectively.

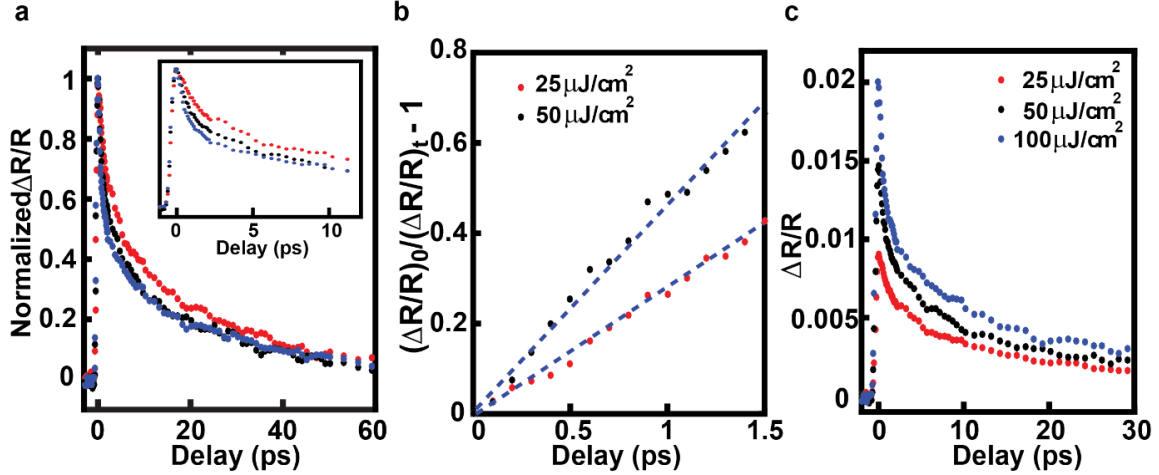


Figure 3-36 Dependence of the exciton dynamics on pumping fluence for as-grown MoS₂ monolayers. (a) Normalized differential reflection of as-grown MoS₂ as a function of the time delay and with different pumping fluences, 25 μJ/cm² (red), 50 μJ/cm² (black), and 100 μJ/cm² (blue). Inset: the results for the early stage of the decay. (b) The result of $(\Delta R/R)_0/(\Delta R/R)_t - 1$ derived from the data in (a) as a function of the delay time. The result for the pumping fluence of 100 μJ/cm² is not shown for the visual convenience. (c) The non-normalized differential reflection of as-grown MoS₂ at pumping fluence 25 μJ/cm² (red), 50 μJ/cm² (black), and 100 μJ/cm² (blue).

We find that substrates may have significant effects on the EEA. We performed similar pump-probe measurements and data analysis for the as-grown MoS₂ and WS₂ monolayers onto sapphire substrates (Figure 3-36 and Figure 3-37). The EEA rate of the supported monolayer is found smaller than that of the suspended counterpart, 0.05 cm²/s and 0.1 cm²/s for the supported MoS₂ and WS₂, respectively. Note that our result for the EEA rate of supported MoS₂ monolayers is reasonably consistent with what previously reported (0.04 cm²/s)¹⁴⁶.

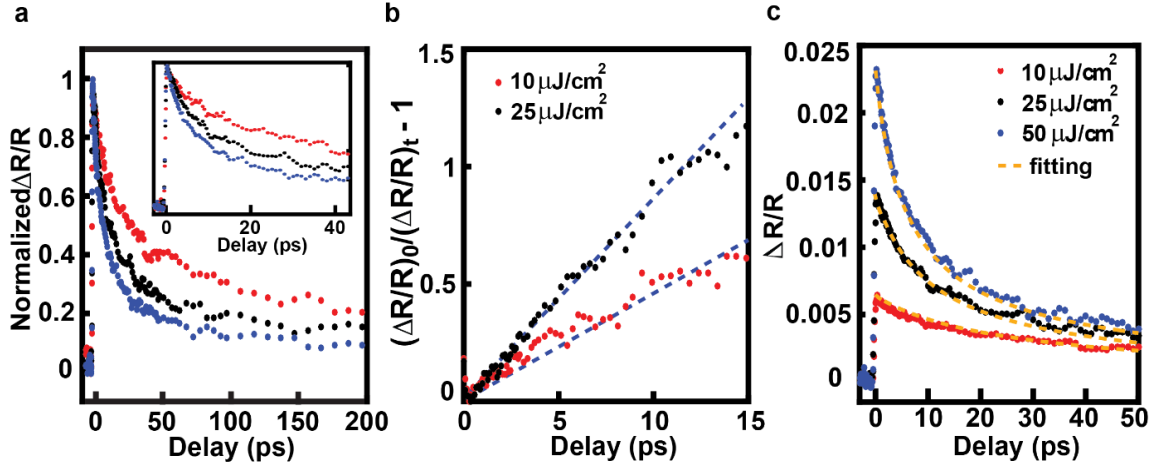


Figure 3-37 Dependence of the exciton dynamics on pumping fluence for as-grown WS₂ monolayers. (a) Normalized differential reflection of suspended WS₂ as a function of the time delay and with different pumping fluences, 10 μJ/cm² (red), 25 μJ/cm² (black), and 50 μJ/cm² (blue). Inset: the results for the early stage of the decay. (b) The result of $(\Delta R/R)_0/(\Delta R/R)_t - 1$ derived from the data in (a) as a function of the delay time. The result for the pumping fluence of 50 μJ/cm² is not shown for the visual convenience. (c) Fitting for the measured differential reflection of as grown WS₂ with different pumping fluences, The fitted results are plotted in dashed lines and the experimental results are dots, 10 μJ/cm² (red), 25 μJ/cm² (black), and 50 μJ/cm² (blue).

The smaller EEA rate in the supported monolayers can be understood from an intuitive perspective. Generally, the rate of EEA is related with the diffusion coefficient of excitons D and the annihilation radius R that represents the separation of two excitons when the annihilation may occur, $k_{ee} = 4\pi DR$ ¹⁴⁷. The presence of substrates may lower the mobility of excitons¹⁴⁸ as well as the exciton binding energy^{149, 150}, the latter of which could subsequently lead to decrease in R . Other than lowering the EEA rate, the substrate may also affect the EEA by providing extra pathways for the exciton to decay. In particular, the defect at the surface of the substrate can dramatically facilitate the decay of excitons by trapping photo-generated charges in the monolayers^{151, 152}. While the defect-assisted decay does not change the EEA rate constant, it could make the observation of the EEA more difficult when the defect-assisted decay is comparable to or faster than the

EEA rate. For instance, the EEA in the supported MoS₂ can be observed only in the first several ps (< 2 ps) and by using relatively high pumping fluence (> 25 μJ/cm²) (Figure 3-36). We found in experiments that it was generally more difficult to observe the EEA in the monolayers showing lower PL intensities and faster exciton decay due to stronger interactions with the substrate. Given the significant effect of substrates on the EEA, we believe that the discrepancies in the previous studies, i.e., the demonstration of different EEA rates in the same materials by different groups^{151, 153-156}, is likely due to different interactions of the monolayer with substrates.

As a summary, we concluded the EEA rates on suspended and substrate-supported MoS₂ and WS₂ monolayers in Table 3-4 for convenience.

Table 3-4 EEA rates on suspended and substrate-supported MoS₂ and WS₂ monolayers.

	MoS ₂	WS ₂
As-grown	0.05 cm ² /s	0.1 cm ² /s
Suspended	0.1 cm ² /s	0.3 cm ² /s

Although EEA will always present even at the lowest pump fluence as we observed, non-radiative decay of excitons will unambiguously dominate the exciton dynamics at low pump fluences in our experiments, especially for the substrate-supported monolayers. As a matter of fact, the previously fitted first exponential time constant in Table 3-1 and Table 3-2 is underestimated without considering the EEA. The underestimation is more on suspended monolayers than that on substrate-supported monolayers because of the higher EEA rate and longer affected time on suspended monolayers. Therefore, the effect of the substrate to the non-radiative decay of exciton should be slightly more than what we have evaluated before.

3.3.4 Conclusions

In conclusion, we have demonstrated that substrates can significantly limit the PL efficiency of 2D TMDC materials. The main effects of the substrate lie in doping the monolayer and affecting the monolayers' exciton dynamics, while the other effects of substrates, such as substrate-induced strains or changes in exciton binding energy, are expected to be minor. The result can provide very useful guidance for the rational design of high-performance 2D TMDC materials light emission devices. It indicates that key to improve the luminescence efficiency is to minimize the adverse effect of doping, decrease the non-radiative recombination. Suspended monolayers embedded in optical cavities would make the best platform for the development of light emission devices. In the case that substrates have to be involved, the substrates of mica or Teflon present a good choice to minimize the doping effect.

We have also quantitatively evaluated the EEA in monolayer TMDC materials by their exciton dynamics. We also show that the EEA rate is dependent on the interaction of the monolayer with substrates and this interaction is likely the reason for the discrepancy in the results of previous studies. While our works mainly focus on monolayer MoS₂ and WS₂, we believe that the analysis and conclusion may be applied to other monolayer TMDC materials such as MoSe₂ and WSe₂.

Chapter 4 Summary and Future works

4.1 Summary

This thesis investigates the applications of ultrafast optical characterization on surfaces and interfaces. Due to its selective sensitivity to surface or interface and ultrashort resolution, processes that are not easily accessible to other methods can be characterized here.

SHG anisotropy has been successfully used on evaluating the interface between Zr and its oxide film. This non-contact, easily accessible optical method is proven to be useful on buried interface characterization. Furthermore, with UHV techniques combined in controlling the surface chemistry, SHG can be applied to study in-situ process, such as adsorption mechanism and physical bonding during oxidation. By controlling gaseous environment and using SHG anisotropy, near surface charge transfer and surface modification were observed upon the cleavage, giving a full picture of surface physics and chemistry on the surface of Bi_2Se_3 . With TRSM, the exciton dynamics of MoS_2 and WS_2 monolayers are characterized. Combined with PL, Raman spectroscopy and first principle calculation, the substrate effects have been revealed.

All those nonlinear methods show unprecedented advantages on surface and interface characterizations and give insights on future surface and interface engineering. Furthermore, when complemented by other techniques, such as UHV technique, PL and Raman measurement, first principles calculation, a full picture on the properties of materials could be revealed.

4.2 Future works

4.2.1 Zr

Zircaloy, an important cladding material for nuclear active cores, has been shown to gradually brittle in nuclear reactors. Most of the studies have attributed this failure to a phenomenon known as hydrogen embrittlement¹⁵⁷⁻¹⁵⁹. At low temperatures, the surface of zircaloy forms a thick and dense zirconia film, posing as a barrier to hydrogen. As the temperature increases again, the zirconia film begins to crack, forming channels enhancing hydrogen re-entry. The interaction between hydrogen and Zr forms hydride, which reduces the hardness and ductility of Zr.

One promising study is to use SHG anisotropy to study the entry or interaction of hydrogen with Zr. Questions such as how hydrogen interacts with fresh and with oxidized Zr can be addressed with our nonlinear optical methods. With our experimental capability, through some optimization, we can introduce ultra-high pure hydrogen into our UHV chamber, and heat the Zr sample to relative high temperatures, thereby simulating the conditions within an actual nuclear reactor. If hydride forms on the interface, the bindings on the interface will change, which may be monitored by SHG anisotropy since its selective sensitivity to the interface.

4.2.2 Bi₂Se₃

Although nontrivial surface states retains due to the discontinuity of the topological numbers between two distinct insulators, the drifting in space will cause unforeseen problems in future application. Thus, how to stabilize or fix it, is still a question in the

research field. From my work, it shows that intrinsic doping will introduce the physical and chemical reaction near surface.

One promising study may be first neutralize the bulk doping by improving material engineering or introduce extrinsic atoms. After a pure insulator is made, SHG anisotropy can be used to characterize its surface dynamics. In this way, we can find out if bulk doping is the trigger of all these physical and chemical processes.

4.2.3 TMDC monolayers

Although the exciton dynamics have been determined using TRSM on supported and suspended MoS₂ and WS₂ monolayers. One question may arise that why the exciton dynamics on supported and suspended TMDC monolayers show ambiguously two different non-radiative processes within 200 ps, which are also not temperature dependent.

One possible explanation is that electron and hole experience different decay channels. One interesting study may be tuning the doping amount of TMDC monolayers. The easiest way is to control the doping electrically. Using TRSM while tuning the doping of TMDC monolayers, it may be able to reveal the two different non-radiative decay processes clearly.

REFERENCES

1. C. Meyer, G. Lüpke, U. Emmerichs, F. Wolter, H. Kurz, C. H. Bjorkman and G. Lucovsky, *Physical Review Letters* 74 (15), 3001-3004 (1995).
2. U. Emmerichs, C. Meyer, H. J. Bakker, F. Wolter, H. Kurz, G. Lucovsky, C. E. Bjorkman, T. Yasuda, Y. Ma, Z. Jing and J. L. Whitten, *Journal of Vacuum Science & Technology B* 12 (4), 2484-2492 (1994).
3. H. Park, J. Qi, Y. Xu, K. Varga, S. M. Weiss, B. R. Rogers, G. Lüpke and N. Tolc, *physica status solidi (b)* 247 (8), 1997-2001 (2010).
4. R. Ehlert, J. Kwon and M. C. Downer, *physica status solidi (c)* 5 (8), 2551-2555 (2008).
5. R. Ehlert, A. Prem, L. Loumakos and M. C. Downer, presented at the Nonlinear Optics, Kauai, Hawaii, 2011 (unpublished).
6. P. Platt, P. Frankel, M. Gass, R. Howells and M. Preuss, *Journal of Nuclear Materials* 454 (1-3), 290-297 (2014).
7. A. Lyapin, L. P. H. Jeurgens, P. C. J. Graat and E. J. Mittemeijer, *Surface and Interface Analysis* 36 (8), 989-992 (2004).
8. A. Lyapin, *Universitätsbibliothek der Universität Stuttgart*, 2005.
9. I. Bespalov, M. Datler, S. Buhr, W. Drachsel, G. Rupprechter and Y. Suchorski, *Ultramicroscopy*.
10. B. Li, A. R. Allnatt, C. S. Zhang and P. R. Norton, *Surface Science* 330 (3), 276-288 (1995).
11. A. Garner, A. Gholinia, P. Frankel, M. Gass, I. MacLaren and M. Preuss, *Acta Materialia* 80, 159-171 (2014).
12. V. G. Keramidas and W. B. White, *Journal of the American Ceramic Society* 57 (1), 22-24 (1974).
13. M. Z. Hasan and C. L. Kane, *Rev. Mod. Phys.* 82 (4), 3045-3067 (2010).
14. X. L. Qi and S. C. Zhang, *Rev. Mod. Phys.* 83 (4), 1057 (2011).
15. M. Z. Hasan and J. E. Moore, in *Annual Review of Condensed Matter Physics*, Vol 2, edited by J. S. Langer (2011), Vol. 2, pp. 55.

16. C. Ojeda-Aristizabal, M. S. Fuhrer, N. P. Butch, J. Paglione and I. Appelbaum, *Applied Physics Letters* 101 (2), 023102 (2012).
17. D. Pesin and A. H. MacDonald, *Nature Materials* 11 (5), 409 (2012).
18. F. Zhang, C. L. Kane and E. J. Mele, *Physical Review B* 86 (8), 081303 (2012).
19. S. S. Pershoguba and V. M. Yakovenko, *Physical Review B* 86 (7), 075304 (2012).
20. C. X. Liu, X. L. Qi, H. J. Zhang, X. Dai, Z. Fang and S. C. Zhang, *Physical Review B* 82 (4), 045122 (2010).
21. J. E. Moore, *Nature* 464 (7286), 194-198 (2010).
22. Y. Xia, D. Qian, D. Hsieh, L. Wray, A. Pal, H. Lin, A. Bansil, D. Grauer, Y. S. Hor, R. J. Cava and M. Z. Hasan, *Nature Physics* 5 (6), 398 (2009).
23. D. Hsieh, Y. Xia, L. Wray, D. Qian, A. Pal, J. H. Dil, J. Osterwalder, F. Meier, G. Bihlmayer, C. L. Kane, Y. S. Hor, R. J. Cava and M. Z. Hasan, *Science* 323 (5916), 919 (2009).
24. Y. Cao, J. A. Waugh, X. W. Zhang, J. W. Luo, Q. Wang, T. J. Reber, S. K. Mo, Z. Xu, A. Yang, J. Schneeloch, G. D. Gu, M. Brahlek, N. Bansal, S. Oh, A. Zunger and D. S. Dessau, *Nature Physics* 9 (8), 499 (2013).
25. L. Miao, Z. F. Wang, W. M. Ming, M. Y. Yao, M. X. Wang, F. Yang, Y. R. Song, F. F. Zhu, A. V. Fedorov, Z. Sun, C. L. Gao, C. H. Liu, Q. K. Xue, C. X. Liu, F. Liu, D. Qian and J. F. Jia, *Proc. Natl. Acad. Sci. U. S. A.* 110 (8), 2758 (2013).
26. D. H. Lu, I. M. Vishik, M. Yi, Y. L. Chen, R. G. Moore and Z. X. Shen, *Annual Review of Condensed Matter Physics*, Vol 3 3, 129 (2012).
27. D. Hsieh, D. Qian, L. Wray, Y. Xia, Y. S. Hor, R. Cava and M. Z. Hasan, *Nature* 452 (7190), 970-974 (2008).
28. H. Zhang, C.-X. Liu, X.-L. Qi, X. Dai, Z. Fang and S.-C. Zhang, *Nature physics* 5 (6), 438-442 (2009).
29. D. Hsieh, Y. Xia, D. Qian, L. Wray, J. Dil, F. Meier, J. Osterwalder, L. Patthey, J. Checkelsky and N. Ong, *Nature* 460 (7259), 1101-1105 (2009).
30. J. G. Analytis, J.-H. Chu, Y. Chen, F. Corredor, R. D. McDonald, Z. Shen and I. R. Fisher, *Physical Review B* 81 (20), 205407 (2010).
31. Y. Hor, A. Richardella, P. Roushan, Y. Xia, J. Checkelsky, A. Yazdani, M. Hasan, N. Ong and R. Cava, *Physical Review B* 79 (19), 195208 (2009).

32. M. Bianchi, D. D. Guan, S. N. Bao, J. L. Mi, B. B. Iversen, P. D. C. King and P. Hofmann, *Nature Communications* 1, 128 (2010).
33. D. Kim, S. Cho, N. P. Butch, P. Syers, K. Kirshenbaum, S. Adam, J. Paglione and M. S. Fuhrer, *Nat. Phys.* 8 (6), 459-463 (2012).
34. D. Hsieh, J. W. McIver, D. H. Torchinsky, D. R. Gardner, Y. S. Lee and N. Gedik, *Physical Review Letters* 106 (5), 057401 (2011).
35. J. W. McIver, D. Hsieh, S. G. Drapcho, D. H. Torchinsky, D. R. Gardner, Y. S. Lee and N. Gedik, *Physical Review B* 86 (3), 035327 (2012).
36. Y. Chen, J.-H. Chu, J. Analytis, Z. Liu, K. Igarashi, H.-H. Kuo, X. Qi, S.-K. Mo, R. Moore and D. Lu, *Science* 329 (5992), 659-662 (2010).
37. B. Zhou, Z. K. Liu, J. G. Analytis, K. Igarashi, S. K. Mo, D. H. Lu, R. G. Moore, I. R. Fisher, T. Sasagawa, Z. X. Shen, Z. Hussain and Y. L. Chen, *Semiconductor Science and Technology* 27 (12), 124002 (2012).
38. V. V. Atuchin, V. A. Golyashov, K. A. Kokh, I. V. Korolkov, A. S. Kozhukhov, V. N. Kruchinin, S. V. Makarenko, L. D. Pokrovsky, I. P. Prosvirin, K. N. Romanyuk and O. E. Tereshchenko, *Crystal Growth & Design* 11 (12), 5507-5514 (2011).
39. V. A. Golyashov, K. A. Kokh, S. V. Makarenko, K. N. Romanyuk, I. P. Prosvirin, A. V. Kalinkin, O. E. Tereshchenko, A. S. Kozhukhov, D. V. Sheglov, S. V. Eremeev, S. D. Borisova and E. V. Chulkov, *Journal of Applied Physics* 112 (11), 113702 (2012).
40. L. V. Yashina, J. Sanchez-Barriga, M. R. Scholz, A. A. Volykhov, A. P. Sirotnina, S. N. Vera, M. E. Tamm, A. Varykhalov, D. Marchenko, G. Springholz, G. Bauer, A. Knop-Gericke and O. Rader, *Acs Nano* 7 (6), 5181-5191 (2013).
41. D. S. Kong, J. J. Cha, K. J. Lai, H. L. Peng, J. G. Analytis, S. Meister, Y. L. Chen, H. J. Zhang, I. R. Fisher, Z. X. Shen and Y. Cui, *Acs Nano* 5 (6), 4698-4703 (2011).
42. N. Bloembergen and P. S. Pershan, *Physical Review* 128 (2), 606-622 (1962).
43. Y. Shen, *Annual Review of Physical Chemistry* 40 (1), 327-350 (1989).
44. J. L. Fiore, V. V. Fomenko, D. Bodlaki and E. Borguet, *Applied Physics Letters* 98 (4), 041905 (2011).
45. J. Qi, M. S. Yeganeh, I. Koltover, A. G. Yodh and W. M. Theis, *Physical Review Letters* 71 (4), 633 (1993).
46. M. S. Bahramy, P. D. C. King, A. de la Torre, J. Chang, M. Shi, L. Patthey, G. Balakrishnan, P. Hofmann, R. Arita, N. Nagaosa and F. Baumberger, *Nature Communications* 3, 1159 (2012).

47. Z. H. Zhu, G. Levy, B. Ludbrook, C. N. Veenstra, J. A. Rosen, R. Comin, D. Wong, P. Dosanjh, A. Ubaldini, P. Syers, N. P. Butch, J. Paglione, I. S. Elfimov and A. Damascelli, *Physical Review Letters* 107 (18), 186405 (2011).
48. P. D. C. King, R. C. Hatch, M. Bianchi, R. Ovsyannikov, C. Lupulescu, G. Landolt, B. Slomski, J. H. Dil, D. Guan, J. L. Mi, E. D. L. Rienks, J. Fink, A. Lindblad, S. Svensson, S. Bao, G. Balakrishnan, B. B. Iversen, J. Osterwalder, W. Eberhardt, F. Baumberger and P. Hofmann, *Physical Review Letters* 107 (9), 096802 (2011).
49. K. I. Bolotin, K. J. Sikes, Z. Jiang, M. Klima, G. Fudenberg, J. Hone, P. Kim and H. L. Stormer, *Solid State Communications* 146 (9–10), 351-355 (2008).
50. A. K. Geim and K. S. Novoselov, *Nat Mater* 6 (3), 183-191 (2007).
51. A. H. Castro Neto, F. Guinea, N. M. R. Peres, K. S. Novoselov and A. K. Geim, *Reviews of Modern Physics* 81 (1), 109-162 (2009).
52. S. Y. Zhou, G. H. Gweon, A. V. Fedorov, P. N. First, W. A. de Heer, D. H. Lee, F. Guinea, A. H. Castro Neto and A. Lanzara, *Nat Mater* 6 (11), 916-916 (2007).
53. P. A. Denis, *Chemical Physics Letters* 492 (4–6), 251-257 (2010).
54. T. Ohta, A. Bostwick, T. Seyller, K. Horn and E. Rotenberg, *Science* 313 (5789), 951-954 (2006).
55. Y. Zhang, T.-T. Tang, C. Girit, Z. Hao, M. C. Martin, A. Zettl, M. F. Crommie, Y. R. Shen and F. Wang, *Nature* 459 (7248), 820-823 (2009).
56. K. F. Mak, C. Lee, J. Hone, J. Shan and T. F. Heinz, *Physical Review Letters* 105 (13) (2010).
57. Z. Y. Zhu, Y. C. Cheng and U. Schwingenschlögl, *Physical Review B* 84 (15) (2011).
58. H. Zeng, J. Dai, W. Yao, D. Xiao and X. Cui, *Nat Nano* 7 (8), 490-493 (2012).
59. K. F. Mak, K. He, J. Shan and T. F. Heinz, *Nat Nano* 7 (8), 494-498 (2012).
60. C. Mai, A. Barrette, Y. Yu, Y. G. Semenov, K. W. Kim, L. Cao and K. Gundogdu, *Nano Letters* 14 (1), 202-206 (2014).
61. Q. Wang, S. Ge, X. Li, J. Qiu, Y. Ji, J. Feng and D. Sun, *ACS Nano* 7 (12), 11087-11093 (2013).
62. P. Tonndorf, R. Schmidt, P. Böttger, X. Zhang, J. Börner, A. Liebig, M. Albrecht, C. Kloc, O. Gordan, D. R. T. Zahn, S. Michaelis de Vasconcellos and R. Bratschitsch, *Opt. Express* 21 (4), 4908-4916 (2013).

63. H. R. Guti érez, N. Perea-L ópez, A. L. El ás, A. Berkdemir, B. Wang, R. Lv, F. L ópez-Ur ás, V. H. Crespi, H. Terrones and M. Terrones, *Nano Letters* 13 (8), 3447-3454 (2013).
64. O. Lopez-Sanchez, D. Lembke, M. Kayci, A. Radenovic and A. Kis, *Nature nanotechnology* 8 (7), 497-501 (2013).
65. Z. Yin, H. Li, H. Li, L. Jiang, Y. Shi, Y. Sun, G. Lu, Q. Zhang, X. Chen and H. Zhang, *ACS nano* 6 (1), 74-80 (2011).
66. B. Radisavljevic, A. Radenovic, J. Brivio, V. Giacometti and A. Kis, *Nature nanotechnology* 6 (3), 147-150 (2011).
67. R. Cheng, D. Li, H. Zhou, C. Wang, A. Yin, S. Jiang, Y. Liu, Y. Chen, Y. Huang and X. Duan, *Nano Letters* 14 (10), 5590-5597 (2014).
68. S. Bertolazzi, D. Krasnozhon and A. Kis, *ACS nano* 7 (4), 3246-3252 (2013).
69. X.-Q. Zhang, C.-H. Lin, Y.-W. Tseng, K.-H. Huang and Y.-H. Lee, *Nano Letters* (2014).
70. J. S. Ross, P. Klement, A. M. Jones, N. J. Ghimire, J. Yan, D. Mandrus, T. Taniguchi, K. Watanabe, K. Kitamura and W. Yao, *Nature nanotechnology* 9 (4), 268-272 (2014).
71. W. Wu, L. Wang, Y. Li, F. Zhang, L. Lin, S. Niu, D. Chenet, X. Zhang, Y. Hao, T. F. Heinz, J. Hone and Z. L. Wang, *Nature* 514 (7523), 470-474 (2014).
72. Y. Lin, X. Ling, L. Yu, S. Huang, A. L. Hsu, Y.-H. Lee, J. Kong, M. S. Dresselhaus and T. Palacios, *Nano Letters* 14 (10), 5569-5576 (2014).
73. K. I. Bolotin, K. Sikes, Z. Jiang, M. Klima, G. Fudenberg, J. Hone, P. Kim and H. Stormer, *Solid State Communications* 146 (9), 351-355 (2008).
74. T. Jin, J. Kang, E. S. Kim, S. Lee and C. Lee, *Journal of Applied Physics* 114 (16), 164509 (2013).
75. C. Dean, A. Young, I. Meric, C. Lee, L. Wang, S. Sorgenfrei, K. Watanabe, T. Taniguchi, P. Kim and K. Shepard, *Nature nanotechnology* 5 (10), 722-726 (2010).
76. M. Buscema, G. A. Steele, H. S. van der Zant and A. Castellanos-Gomez, *Nano Research* 7 (4), 561-571 (2014).
77. Y. Li, Z. Qi, M. Liu, Y. Wang, X. Cheng, G. Zhang and L. Sheng, *Nanoscale* 6 (24), 15248-15254 (2014).
78. W. Bao, X. Cai, D. Kim, K. Sridhara and M. S. Fuhrer, *Applied physics letters* 102 (4), 042104 (2013).

79. S. Najmaei, X. Zou, D. Er, J. Li, Z. Jin, W. Gao, Q. Zhang, S. Park, L. Ge and S. Lei, *Nano Letters* 14 (3), 1354-1361 (2014).
80. A. Castellanos-Gomez, R. Roldán, E. Cappelluti, M. Buscema, F. Guinea, H. S. van der Zant and G. A. Steele, *Nano Letters* 13 (11), 5361-5366 (2013).
81. H. J. Conley, B. Wang, J. I. Ziegler, R. F. Haglund Jr, S. T. Pantelides and K. I. Bolotin, *Nano Letters* 13 (8), 3626-3630 (2013).
82. S. Mouri, Y. Miyauchi and K. Matsuda, *Nano Letters* 13 (12), 5944-5948 (2013).
83. D. Sercombe, S. Schwarz, O. Del Pozo-Zamudio, F. Liu, B. Robinson, E. Chekhovich, I. Tartakovskii, O. Kolosov and A. Tartakovskii, *Scientific Reports* 3 (2013).
84. H. Shi, R. Yan, S. Bertolazzi, J. Brivio, B. Gao, A. Kis, D. Jena, H. G. Xing and L. Huang, *ACS Nano* 7 (2), 1072-1080 (2012).
85. H. Wang, C. Zhang and F. Rana, *Nano Letters* 15 (1), 339-345 (2015).
86. Z. Nie, R. Long, L. Sun, C.-C. Huang, J. Zhang, Q. Xiong, D. W. Hewak, Z. Shen, O. V. Prezhdo and Z.-H. Loh, *ACS Nano* 8 (10), 10931-10940 (2014).
87. J. He, D. He, Y. Wang, Q. Cui, F. Ceballos and H. Zhao, *Nanoscale* 7 (21), 9526-9531 (2015).
88. X. Guo, H. Chen, X. Wen and J. Zheng, *The Journal of Chemical Physics* 142 (21), 212447 (2015).
89. R. Wang, B. A. Ruzicka, N. Kumar, M. Z. Bellus, H.-Y. Chiu and H. Zhao, *Physical Review B* 86 (4), 045406 (2012).
90. F. Ceballos, M. Z. Bellus, H.-Y. Chiu and H. Zhao, *ACS Nano* 8 (12), 12717-12724 (2014).
91. X. Hong, J. Kim, S.-F. Shi, Y. Zhang, C. Jin, Y. Sun, S. Tongay, J. Wu, Y. Zhang and F. Wang, *Nat Nano* 9 (9), 682-686 (2014).
92. T. H. Maiman, *Nature* 187 (4736), 493-494 (1960).
93. P. A. Franken, A. E. Hill, C. W. Peters and G. Weinreich, *Physical Review Letters* 7 (4), 118-119 (1961).
94. B. Gokce, E. J. Adles, D. E. Aspnes and K. Gundogdu, *Proc. Natl. Acad. Sci. U. S. A.* 107 (41), 17503 (2010).
95. C.-J. Kim, L. Brown, M. W. Graham, R. Hovden, R. W. Havener, P. L. McEuen, D. A. Muller and J. Park, *Nano Letters* 13 (11), 5660-5665 (2013).

96. Y. Li, Y. Rao, K. F. Mak, Y. You, S. Wang, C. R. Dean and T. F. Heinz, *Nano Letters* 13 (7), 3329-3333 (2013).
97. L. Malard, T. Alencar, A. P. M. Barboza, K. F. Mak and A. de Paula, *Physical Review B* 87 (20), 201401 (2013).
98. C. Janisch, Y. Wang, D. Ma, N. Mehta, A. L. Elias, N. Perea-Lopez, M. Terrones, V. Crespi and Z. Liu, *Sci. Rep.* 4 (2014).
99. G. Powell, J.-F. Wang and D. Aspnes, *Physical Review B* 65 (20), 205320 (2002).
100. Y. R. Shen, *Principles of nonlinear optics.* (1984).
101. J. E. Sipe, D. J. Moss and H. M. van Driel, *Physical Review B* 35 (3), 1129-1141 (1987).
102. G. Lüpke, D. J. Bottomley and H. M. van Driel, *J. Opt. Soc. Am. B* 11 (1), 33-44 (1994).
103. J. W. McIver, D. Hsieh, S. G. Drapcho, D. H. Torchinsky, D. R. Gardner, Y. S. Lee and N. Gedik, *Physical Review B* 86 (3), 035327 (2012).
104. D. Hsieh, J. McIver, D. Torchinsky, D. Gardner, Y. Lee and N. Gedik, *Physical review letters* 106 (5), 057401 (2011).
105. P. Platt, V. Allen, M. Fenwick, M. Gass and M. Preuss, *Corrosion Science* 98, 1-5 (2015).
106. X. Wang, M. Khafizov and I. Szlufarska, *Journal of Nuclear Materials* 445 (1-3), 1-6 (2014).
107. F.-H. Wang, S.-Y. Liu, J.-X. Shang, Y.-S. Zhou, Z. Li and J. Yang, *Surface Science* 602 (13), 2212-2216 (2008).
108. B. Gokce, E. J. Adles, D. E. Aspnes and K. Gundogdu, *Proceedings of the National Academy of Sciences* 107 (41), 17503-17508 (2010).
109. G. Bakradze, L. P. H. Jeurgens and E. J. Mittemeijer, *Surface and Interface Analysis* 42 (6-7), 588-591 (2010).
110. S. Tanuma, C. J. Powell and D. R. Penn, *Surface and Interface Analysis* 11 (11), 577-589 (1988).
111. H. W. K. Tom, C. M. Mate, X. D. Zhu, J. E. Crowell, T. F. Heinz, G. A. Somorjai and Y. R. Shen, *Physical Review Letters* 52 (5), 348-351 (1984).
112. C. Xu, A. Hewitt, J. Wang, T. Guan, J. Boltersdorf, P. A. Maggard, D. B. Dougherty and K. Gundogdu, *Journal of Applied Physics* 116 (4), - (2014).

113. A. S. Hewitt, J. Wang, J. Boltersdorf, P. A. Maggard and D. B. Dougherty, *Journal of Vacuum Science & Technology B* 32 (4), - (2014).
114. Y. L. Chen, J. H. Chu, J. G. Analytis, Z. K. Liu, K. Igarashi, H. H. Kuo, X. L. Qi, S. K. Mo, R. G. Moore, D. H. Lu, M. Hashimoto, T. Sasagawa, S. C. Zhang, I. R. Fisher, Z. Hussain and Z. X. Shen, *Science* 329 (5992), 659 (2010).
115. H. M. Benia, C. T. Lin, K. Kern and C. R. Ast, *Physical Review Letters* 107 (17), 177602 (2011).
116. S. Solmi, M. Ferri, M. Bersani, D. Giubertoni and V. Soncini, *Journal of Applied Physics* 94 (8), 4950 (2003).
117. O. L. A. Monti, *Journal of Physical Chemistry Letters* 3 (17), 2342 (2012).
118. V. De Renzi, R. Rousseau, D. Marchetto, R. Biagi, S. Scandolo and U. del Pennino, *Physical Review Letters* 95 (4), 046804 (2005).
119. Z. Rosenzweig and M. Asscher, *Surface Science* 204 (1–2), L732 (1988).
120. F. Eisert, A. Elg and A. Ros n, *Applied Physics A* 60 (2), 209-215 (1995).
121. G. N. Derry and P. N. Ross, *The Journal of Chemical Physics* 82 (6), 2772-2778 (1985).
122. B. Gokce, D. E. Aspnes and K. Gundogdu, *Applied Physics Letters* 98 (12), 121912 (2011).
123. B. Gokce, D. E. Aspnes, G. Lucovsky and K. Gundogdu, *Applied Physics Letters* 98 (2), 021904 (2011).
124. B. Gokce, D. B. Dougherty and K. Gundogdu, *Journal of Vacuum Science & Technology A* 30 (4), 040603 (2012).
125. Y. Yu, C. Li, Y. Liu, L. Su, Y. Zhang and L. Cao, *Scientific Reports* 3, 1866 (2013).
126. A. Gurarlan, Y. Yu, L. Su, Y. Yu, F. Suarez, S. Yao, Y. Zhu, M. Ozturk, Y. Zhang and L. Cao, *ACS Nano* 8 (11), 11522-11528 (2014).
127. S. Najmaei, Z. Liu, W. Zhou, X. Zou, G. Shi, S. Lei, B. I. Yakobson, J.-C. Idrobo, P. M. Ajayan and J. Lou, *Nature Materials* 12 (8), 754-759 (2013).
128. A. M. van der Zande, P. Y. Huang, D. A. Chenet, T. C. Berkelbach, Y. You, G.-H. Lee, T. F. Heinz, D. R. Reichman, D. A. Muller and J. C. Hone, *Nature Materials* 12 (6), 554-561 (2013).

129. Y. H. Lee, X. Q. Zhang, W. Zhang, M. T. Chang, C. T. Lin, K. D. Chang, Y. C. Yu, J. T. W. Wang, C. S. Chang and L. J. Li, *Advanced Materials* 24 (17), 2320-2325 (2012).
130. K. F. Mak, C. Lee, J. Hone, J. Shan and T. F. Heinz, *Phys Rev Lett* 105 (13) (2010).
131. L. Yuan and L. Huang, *Nanoscale* 7 (16), 7402-7408 (2015).
132. C. Zheng, Z.-Q. Xu, Q. Zhang, M. T. Edmonds, K. Watanabe, T. Taniguchi, Q. Bao and M. S. Fuhrer, *Nano Letters* (2015).
133. H. Nan, Z. Wang, W. Wang, Z. Liang, Y. Lu, Q. Chen, D. He, P. Tan, F. Miao and X. Wang, *ACS nano* 8 (6), 5738-5745 (2014).
134. S. Tongay, J. Suh, C. Ataca, W. Fan, A. Luce, J. S. Kang, J. Liu, C. Ko, R. Raghunathanan and J. Zhou, *Scientific Reports* 3 (2013).
135. J. O. Varghese, P. Agbo, A. M. Sutherland, V. W. Brar, G. R. Rossman, H. B. Gray and J. R. Heath, *Advanced Materials* (2015).
136. K. F. Mak, K. L. He, C. Lee, G. H. Lee, J. Hone, T. F. Heinz and J. Shan, *Nature Materials* 12 (3), 207-211 (2013).
137. H. Wang, *Nano Letters* (2014).
138. H. Shi, R. Yan, S. Bertolazzi, J. Brivio, B. Gao, A. Kis, D. Jena, H. G. Xing and L. Huang, *ACS nano* 7 (2), 1072-1080 (2013).
139. G.-H. Lee, Y.-J. Yu, X. Cui, N. Petrone, C.-H. Lee, M. S. Choi, D.-Y. Lee, C. Lee, W. J. Yoo and K. Watanabe, *ACS nano* 7 (9), 7931-7936 (2013).
140. C. Rice, R. Young, R. Zan, U. Bangert, D. Wolverson, T. Georgiou, R. Jalil and K. Novoselov, *Physical Review B* 87 (8), 081307 (2013).
141. A. Castellanos-Gomez, R. Roldán, E. Cappelluti, M. Buscema, F. Guinea, H. S. J. van der Zant and G. A. Steele, *Nano Letters* 13 (11), 5361-5366 (2013).
142. H. J. Conley, B. Wang, J. I. Ziegler, R. F. Haglund, S. T. Pantelides and K. I. Bolotin, *Nano Letters* 13 (8), 3626-3630 (2013).
143. Z. Liu, M. Amani, S. Najmaei, Q. Xu, X. Zou, W. Zhou, T. Yu, C. Qiu, A. G. Birdwell and F. J. Crowne, *Nature communications* 5 (2014).
144. K.-G. Zhou, F. Withers, Y. Cao, S. Hu, G. Yu and C. Casiraghi, *ACS nano* 8 (10), 9914-9924 (2014).
145. L. C. Yiling Yu, (2015).

146. D. Sun, Y. Rao, G. A. Reider, G. Chen, Y. You, L. Brézin, A. R. Harutyunyan and T. F. Heinz, *Nano Letters* 14 (10), 5625-5629 (2014).
147. G. M. Akselrod, Y. R. Tischler, E. R. Young, D. G. Nocera and V. Bulovic, *Physical Review B* 82 (11), 113106 (2010).
148. N. Ma and D. Jena, *Physical Review X* 4 (1), 011043 (2014).
149. Y. X. Lin, X. Ling, L. L. Yu, S. X. Huang, A. L. Hsu, Y. H. Lee, J. Kong, M. S. Dressehaus and T. Palacios, *Nano Lett* 14 (10), 5569-5576 (2014).
150. M. M. Ugeda, A. J. Bradley, S. F. Shi, F. H. da Jornada, Y. Zhang, D. Y. Qiu, W. Ruan, S. K. Mo, Z. Hussain, Z. X. Shen, F. Wang, S. G. Louie and M. F. Crommie, *Nat Mater* 13 (12), 1091-1095 (2014).
151. H. N. Wang, C. J. Zhang and F. Rana, *Nano Lett* 15 (1), 339-345 (2015).
152. C. J. Docherty, P. Parkinson, H. J. Joyce, M.-H. Chiu, C.-H. Chen, M.-Y. Lee, L.-J. Li, L. M. Herz and M. B. Johnston, *ACS Nano* 8, 11147-11153 (2014).
153. S. Mouri, Y. Miyauchi, M. Toh, W. J. Zhao, G. Eda and K. Matsuda, *Phys Rev B* 90 (15) (2014).
154. D. Z. Sun, Y. Rao, G. A. Reider, G. G. Chen, Y. M. You, L. Brezin, A. R. Harutyunyan and T. F. Heinz, *Nano Lett* 14 (10), 5625-5629 (2014).
155. H. Shi, R. Yan, S. Bertolazzi, J. Brivio, B. Gao, A. Kis, D. Jena, H. G. Xing and L. Huang, *ACS Nano* 7, 1072-1080 (2013).
156. Q. Cui, F. Ceballos, N. Kumar and H. Zhao, *ACS Nano* 8, 2970-2976 (2014).
157. C. J. Simpson and C. E. Ells, *Journal of Nuclear Materials* 52 (2), 289-295 (1974).
158. L. Simpson and C. Cann, *Journal of Nuclear Materials* 87 (2), 303-316 (1979).
159. I. A. E. Agency, Delayed hydride cracking in zirconium alloys in pressure tube nuclear reactors: final report of a coordinated research project 1998-2002. (International Atomic Energy Agency, 2004).

APPENDICES

Appendix A Specifications of Laser System

We used a commercial ultrafast laser system from Coherent Inc. As in Fig. A-1, the laser system consists of 3 main components. First, Mira 900 is pumped by Verdi G7 at 532 nm, and Mira 900 has pulsed lasing centered around 800 nm with pulse width of <200 fs, maximum pulse energy of ~13 nJ and repetition rate of 76 MHz. Second, the regenerative amplifier Rega 9000, picks up part of the output from Mira 900, and amplifies the lasing centered around 800 nm (same as Mira 900) with pulse width of <160 fs, maximum pulse energy of 5 μ J and repetition rate of 250 kHz. Third, the optical parametric amplifier OPA 9400, is pumped by Rega 9000. Once the output from Rega 9000 enters into OPA 9400, the output splits into two beams: once is used to focus on sapphire crystal to generate supercontinuum whitelight; the other one is used to focus on SHG BBO crystal to generate SHG. The optical parametric amplification takes place twice (forward-1st and reflected backward-2nd) when whitelight and SHG are overlapped on OPA BBO crystal both in spatial and time domains. The wavelength of the signal (λ_s) can be controlled by the angle of OPA BBO crystal through the rule of phase matching. The relationship between the wavelength of the signal (λ_s) and that of the idler (λ_i):

$$\frac{1}{\lambda_s} + \frac{1}{\lambda_i} = \frac{1}{\lambda_{\text{SHG}}} = \frac{1}{400 \text{ nm}}$$

Eq. A-1

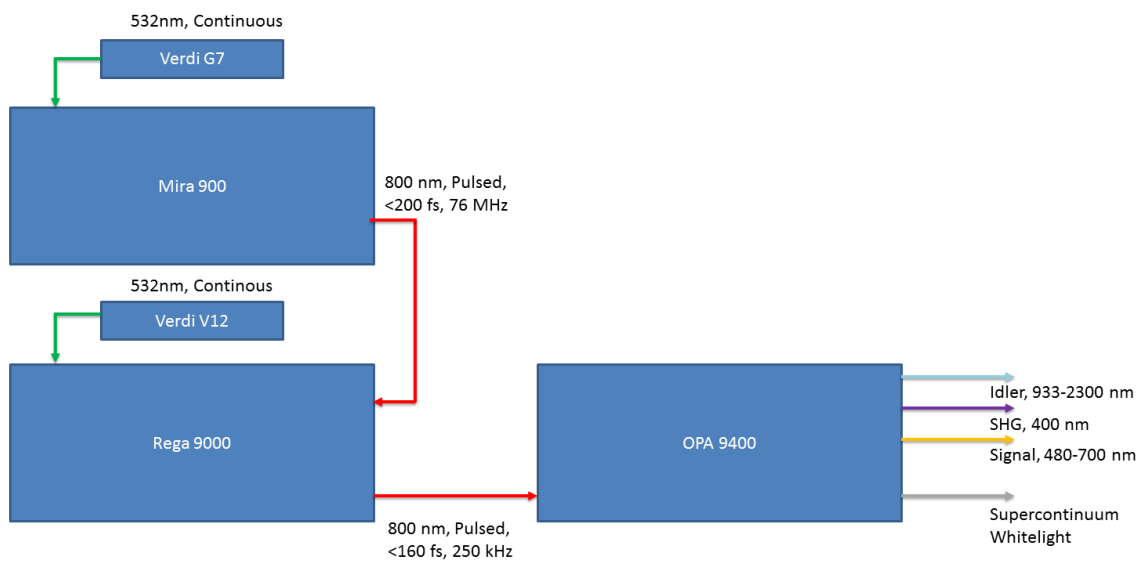


Fig. A-1 Diagram of the laser system.

The Gaussian fitting of cross correlation between OPA signal and whitelight with the monochromator fixed at one wavelength gives a full width half maximum (FWHM) of ~ 450 fs, which is the resolution of the pump-probe experiment when using OPA signal as pump and a fixed wavelength component in whitelight as probe.

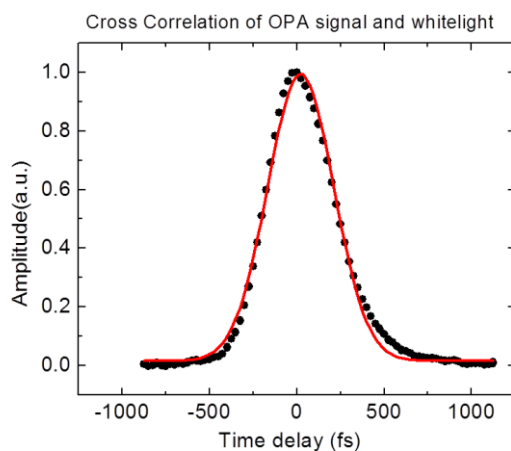


Fig. A-2 Cross correlation of pump and probe pulses.

Appendix B Focused Laser Beam Size

First, let's estimate the focus limit of a collimated laser beam through a normal lens⁴.

The diverging beam has a full angular width limit θ :

$$\theta = \frac{4\lambda}{\pi d}$$

Eq. B-1

d is the diameter limit of the focus, and λ is the wavelength of the laser.

Consider a collimated laser beam with a diameter of D on the lens, and a lens with focus distance F . θ is given by geometrical optics as the diameter illuminated on the lens, D , divided by the focal length of the lens, F :

$$\theta = \frac{D}{F}$$

Eq. B-2

Equating Eq. B-1 and Eq. B-2, the focus limit in diameter is:

$$d = \frac{4\lambda}{\pi} \cdot \frac{F}{D}$$

Eq. B-3

For example, in the SHG anisotropy experiment, a collimated 800 nm laser with beam width 2 mm in diameter focused by a 7.5 cm lens will have a focus limit in diameter:

⁴ Cited partially from Gaussian Beam Optics Tutorial, Newport Inc.

$$d = \frac{4\lambda}{\pi} \cdot \frac{F}{D} = \frac{4 * 800 \text{ nm}}{\pi} * \frac{7.5 \text{ cm}}{2 \text{ mm}} \approx 40 \mu\text{m}$$

Eq. B-4

Whereas in the SHG experiment for sample sitting in the UHV system, because of the limits in geometry, a 30 cm focus lens was used, instead. Thus the focus limit in diameter is:

$$d = \frac{4\lambda}{\pi} \cdot \frac{F}{D} = \frac{4 * 800 \text{ nm}}{\pi} \cdot \frac{30 \text{ cm}}{2 \text{ mm}} \approx 150 \mu\text{m}$$

Eq. B-5

For microscopic objective, the focus limit can be approximated by:

$$d = \frac{2\lambda}{\text{N.A.}}$$

Eq. B-6

N.A. represents numerical aperture. In our microscopic experiment, a 50X long working distance (1.1 cm) objective with N.A. of 0.60 was used. With $\lambda = 590 \text{ nm}$, the focus limit in diameter is estimated to be:

$$d = \frac{2\lambda}{\text{N.A.}} = \frac{2 * 590 \text{ nm}}{0.60} = 2 \mu\text{m}$$

Eq. B-7

The beam size can also be precisely measured by the knife edge experiment. The method is to record the total power of the beam as a knife edge is translated through the beam. In this way, the power measures the integral of the Gaussian beam between the position of the knife and $+\infty$. Assume a Gaussian beam with intensity profile:

$$I(x, y) = I_0 e^{-2(x^2+y^2)/\omega^2}$$

Eq. B-8

Assume P_{tot} is the total power of the laser beam, after the integration of Eq. B-8 from X to $+\infty$, the transmitted power is:

$$P(X) = \frac{P_{\text{tot}}}{2} \left[1 - \operatorname{erf} \left(\frac{\sqrt{2}X}{\omega} \right) \right]$$

Eq. B-9

To fit the function in Matlab, the following function instead of Eq. B-9 was used:

$$P_{\text{measured}} = \frac{p1}{2} \left[1 - \operatorname{erf} \left(\frac{\sqrt{2}(x - p2)}{p3} \right) \right]$$

Eq. B-10

Where $p1$ corresponds to the full power, $p2$ corresponds to the central position of the beam, and $p3$ corresponds to the beam waist. Fig. B-1 shows a typical knife edge measurement (black dots) of the focused beam using the 50X long working distance objective, with pump wavelength 590 nm from OPA. The fitting using Eq. B-10 gives $p1 = 5.67 \mu\text{W}$, $p2 = -0.45 \mu\text{m}$ and $p3 = 1.41 \mu\text{m}$. The estimate of $r = d/2 = 1 \mu\text{m}$ in Eq. B-7 yields reasonable deviation from the measured beam waist $\omega = 1.41 \mu\text{m}$.

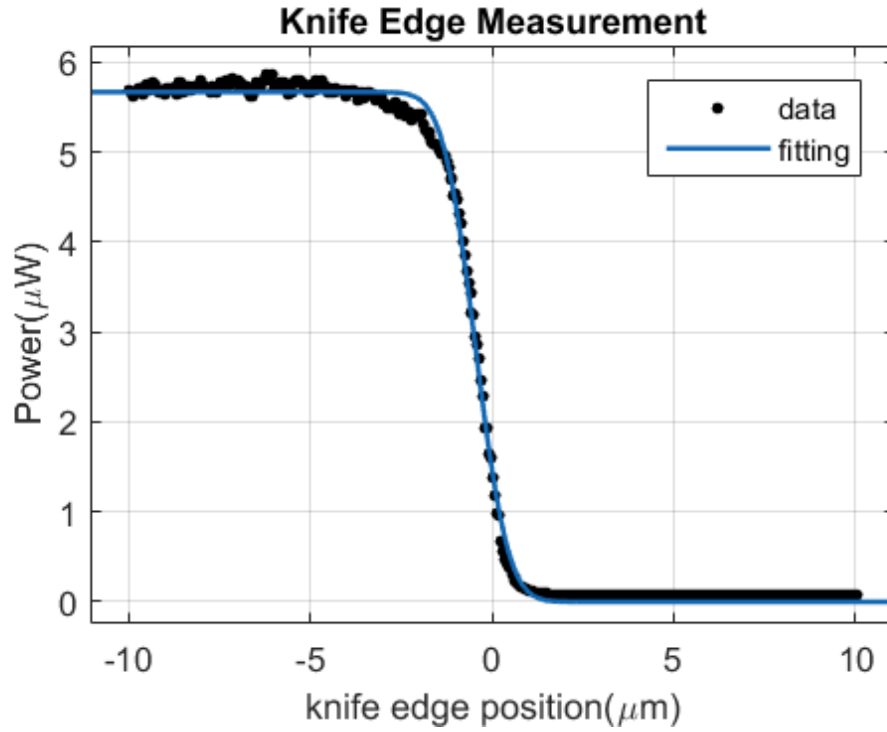


Fig. B-1 Knife edge measurement (black dots) of the focused beam using a 50X long working distance objective. The fitting (blue curve) using Eq. B-10 gives $p_1 = 5.67 \mu\text{W}$, $p_2 = -0.45 \mu\text{m}$ and $p_3 = 1.41 \mu\text{m}$.

Appendix C Pump Fluence Conversion

Here is one example to calculate the laser fluence of 1 μW , with 250 kHz repetition rate laser, focused on the sample by a 50X long working distance objective.

Here:

Laser beam size $D = 2 \mu\text{m}$,

Laser power $P = 1 \mu\text{W}$,

Repetition rate $\text{Rep} = 250 \text{ kHz}$.

Laser fluence is defined as the energy density per laser pulse. The beam shape can be approximated as a square. Thus:

$$\text{Beam area (S)} = D^2 = 4 \mu\text{m}^2 = 4 \times 10^{-12} \text{m}^2$$

$$\text{Energy per pulse (E)} = \frac{P}{\text{Rep}} = \frac{1\mu\text{W}}{250\text{kHz}} = \frac{1 \times 10^{-6} \text{W}}{250 \times 10^3 \text{s}^{-1}} = 4 \times 10^{-12} \text{J}$$

$$\text{Laser fluence} = \frac{E}{S} = \frac{4 \times 10^{-12} \text{J}}{4 \times 10^{-12} \text{m}^2} = \frac{1 \text{J}}{\text{m}^2} = \frac{1 \times 10^6 \mu\text{J}}{1 \times 10^4 \text{cm}^2} = 100 \mu\text{J}/\text{cm}^2$$

Si_3=0.5303*a0+0.5303*b0+0.333333*c0;

O_1=0.4135*a0+0.2669*b0+0.1191*c0;

O_2=0.2669*a0+0.4135*b0+0.547567*c0;

O_3=0.7331*a0+0.1466*b0+0.785767*c0;

O_4=0.5865*a0+0.8534*b0+0.214233*c0;

O_5=0.8534*a0+0.5865*b0+0.452433*c0;

O_6=0.1466*a0+0.7331*b0+0.8809*c0;

numofhypers=1; % # of different bond types

% Bond directions

% For quartz, here are 12 effective bonds, and all the bonds have the same

% hyperpolarizabilities.

bonds = [(Si_3-O_1)/norm(Si_3-O_1); % bond1 to Si3

(Si_3-O_2)/norm(Si_3-O_2); % bond2 to Si3

(Si_3-O_4)/norm(Si_3-O_4); % bond3 to Si3

(Si_3-O_5)/norm(Si_3-O_5); % bond4 to Si3

(Si_1-O_1)/norm(Si_1-O_1); % bond1 to Si1

(Si_1+c0-O_3)/norm(Si_1+c0-O_3); % bond2 to Si1

(Si_1+b0-O_4)/norm(Si_1+b0-O_4); % bond3 to Si1

(Si_1+b0+c0-O_6)/norm(Si_1+b0+c0-O_6); % bond4 to Si1

(Si_2-O_2)/norm(Si_2-O_2); % bond1 to Si2

(Si_2+a0-O_3)/norm(Si_2+a0-O_3); % bond2 to Si2

(Si_2+a0-O_5)/norm(Si_2+a0-O_5); % bond3 to Si2

(Si_2-O_6)/norm(Si_2-O_6) % bond4 to Si2

```

];

% Set the initial sample surface direction.
% ST-cut (42.75 deg): Euler angle(0,132.75,42.75)

theta_x = 35; % In degrees
theta_y = 132.75; % In degrees
theta_z = 42.75; % In degrees

surface_x=[1      0      0;
           0 cos(theta_x*pi/180) -sin(theta_x*pi/180);
           0 sin(theta_x*pi/180) cos(theta_x*pi/180)];
surface_y=[cos(theta_y*pi/180) 0 sin(theta_y*pi/180);
           0      1      0;
           -sin(theta_y*pi/180) 0 cos(theta_y*pi/180)];
surface_z=[cos(theta_z*pi/180) -sin(theta_z*pi/180) 0;
           sin(theta_z*pi/180) cos(theta_z*pi/180) 0;
           0      0      1];

surface_rotate = surface_z*surface_y*surface_x;
bonds = (surface_rotate*(bonds.')).'; % Rotate the unit cell

numofbonds=size(bonds,1); % Get # of bonds
hypers = sym('hyper',[1 numofhypers]); % Assign different hyperparameters based on the #
% Assign other parameters: phi_0 is the starting angle of azimuthal
% rotation; phi is the rotated angle
syms phi_0 phi;
% hypers, phi_0 and phi are in symbol (not numerical)
Z_rotate = [cos((phi+phi_0)*pi/180) -sin((phi+phi_0)*pi/180) 0;
            sin((phi+phi_0)*pi/180) cos((phi+phi_0)*pi/180) 0;
            0      0      1];

```

```

bonds_rotated = (Z_rotate*(bonds.)).';% Azimuthal rotation

#####

% Part 2: Construct functions of SHG_p and SHG_s with bond model.

% Select the polarization of the incoming beam
Ep = [-cos(theta_i*pi/180),0,sin(theta_i*pi/180)]; %p-polarized_input field
% Ep=[0 1 0]; %s-polarized_input field
% Calculate polarization
Polz=zeros(1,3); % Initialize polarization
for count=1:numofbonds;
    Polz = Polz + hypers(1)*(bonds_rotated(count,:)*Ep.)^2*bonds_rotated(count,:);
    % Sum up polarization from differennt bonds
end
% Calculate SHG light
k_shg = [-sin(theta_0*pi/180),0,cos(theta_0*pi/180)]; % Wave vector along the SHG light
E_shg = Polz - (k_shg*Polz.)*k_shg; % SHG radiation
% P-polarized
SHG_p = abs(E_shg*[1;0;0])^2+abs(E_shg*[0;0;1])^2; % P-polarized SHG
disp('#####SHG P polarized#####');
disp(SHG_p);
disp('#####');
% for n=1:numofhypers
%   SHG_p=subs(SHG_p,hypers(n),strcat('a(',num2str(n),')'));
% end
%
% SHG_p=subs(SHG_p,phi_0,strcat('a(',num2str(n+1),')'));
% Convert SHG_p to matlab function

```

```
SHG_in_p = matlabFunction(SHG_p,'file','myfile','vars', {[hypers phi_0], phi});
```

```
% S-polarized
```

```
SHG_s = abs(E_shg*[0;1;0])^2; % S-polarized SHG
```

```
SHG_in_s = matlabFunction(SHG_s,'vars', {[hypers phi_0], phi});
```

```
disp('#####SHG S polarized#####');
```

```
disp(SHG_s);
```

```
disp('#####');
```

```
% P-polarized + S-polarized
```

```
SHG_all = norm(E_shg)^2; % SHG all
```

```
SHG_for_all = matlabFunction(SHG_all,'vars', {[hypers phi_0 ], phi});
```

```
disp('#####SHG total polarized#####');
```

```
disp(SHG_all);
```

```
disp('#####');
```

```
%#####
```

```
% Part 3: Plot SHG anisotropy with initial parameters.
```

```
clear hypers phi_0 phi;
```

```
figure(1);
```

```
hold off;
```

```
plot(0:360,SHG_in_p([1 0],0:360));
```

```
hold all;
```

```
plot(0:360,SHG_in_s([1 0],0:360));
```

```
plot(0:360,SHG_for_all([1 0],0:360))
```

```
axis tight;
```

```
y_lim=yylim;
```

```
yylim([y_lim(1) y_lim(2)*1.2]);
```

```

legend('Parallel','Perpendicular','Total');

title('SHG Anisotropy')

#####

%Part 4: Fit parameters with experimental data.

%Initialize fitting parameters

hyper_0=1;

phi_0=0;

hyper_fit0=[hyper_0 phi_0];

%for P-all

data_all=load('Quartz_4mW.txt');

figure(2);

hold off;

plot(data_all(:,1),data_all(:,2),'o');

hyper_fit_all = lsqcurvefit(SHG_for_all,hyper_fit0,data_all(:,1),data_all(:,2));

hold all;

plot(data_all(:,1),SHG_for_all(hyper_fit_all,data_all(:,1)));

axis tight;

y_lim=ylim;

ylim([y_lim(1) y_lim(2)*1.2]);

legend('Data','Fitting');

title('SHG Anisotropy-P');

```